Convective-scale radar data assimilation and adaptive radar observation with the Ensemble Kalman Filter

by

Weiguang Chang

Department of Atmospheric and Oceanic Sciences

McGill University, Montréal, Québec, Canada

A thesis submitted to McGill University in partial fulfillment of the requirements of the degree of Doctor of Philosophy

April, 2014

Abstract

The flow-dependent background error statistics and other uncertainties involved in Ensemble Kalman Filter (EnKF), such as model error, initial perturbations, etc., are studied by a numerical weather prediction model and a few simple idealized experiments, respectively. Following the aforementioned studies, a convective-scale EnKF system is implemented to assimilate real radar data of radial velocity provided by the McGill J. S. Marshall Radar Observatory. The performance of this system and its impact on short-term ensemble forecasts are examined in three summer cases with different precipitation structures. In order to enhance and prolong the improvement brought by radar data assimilation on weather prediction, an adaptive radar observation method is proposed based on the background error statistics in EnKF. This method takes advantage of the phased-array radar technique to adaptively place observations where the important and unobserved model variable has more chances of improvement.

The idealized experiments of EnKF suggest that a better analysis requires sufficient ensemble spread in initial perturbation, accurate estimation of model and observation errors, and radar data thinning if necessary. The studies on the background error statistics showed that homogeneous isotropic background error perturbations can develop into situation-dependent features in 15 minutes, and the error structures in the regions with and without precipitation are different. Results from the high-resolution EnKF system indicate that the analysis uncertainty can be reduced after a 1-h cycling process; and that radial velocity assimilation has an impact on the precipitation field. Additionally, the improvement in ensemble forecasts is evident in observation space within a 2-hour lead-time. When the adaptive radar observation method is applied on radial velocity assimilation, the unobserved vertical velocity can be better improved in areas where background error cross-covariances is more significant. Nevertheless, the improvement on the unobserved variable is much smaller than for the observed variable.

Résumé

Les statistiques d’erreur de prévisions dépendent de l’écoulement atmosphérique ainsi que d'autres incertitudes associées au Filtre de Kalman d'Ensemble (EnKF), tels que l'erreur de modèle, les perturbations initiales, etc. Ces erreurs sont étudiées à l'aide d'expériences idéalisées ainsi que d'un modèle numérique de prévisions météorologiques. À cet effet, un système d’EnKF à l'échelle convective a été développé pour assimiler les données radar de vitesse radiale fournies par l'observatoire radar JS Marshall à l'université McGill. La performance de ce système et son impact sur les prévisions d'ensembles sont examinés à partir d'un échantillon de trois situations atmosphériques présentant des structures de précipitations différentes. Afin d'améliorer et de prolonger l'effet bénéfique apporté par l'assimilation de données, nous proposons une méthode adaptative d'observations radar basée sur les statistiques d'erreurs de prévision du système EnKF. Cette méthode vise à tirer parti de la rapidité associée au balayage électronique (phased array) afin de choisir de manière adaptative les endroits ou de futures observations ont le plus de chance d'améliorer l'analyse de variables non observées.

Les expériences idéalisées à partir de systèmes EnKF suggèrent que des analyses de qualité nécessitent des perturbations initiales de magnitude adéquates, des estimations précises des erreurs de modèle et d'observations ainsi que l'utilisation d'observations aux erreurs non corrélées. L'étude sur les statistiques d'erreur de background a montré que les perturbations isotropes et homogènes peuvent se développer suffisamment pour présenter des erreurs dont la structure diffère entre les régions avec et sans précipitation. Les résultats provenant du système d’EnKF à haute résolution indiquent que l'incertitude de l'analyse peut être réduite après un processus de cyclage pendant une heure. Aussi, il est démontré l'assimilation de la vitesse radiale a un impact sur le champ de précipitations. L'amélioration par rapport aux observations est mesurable pour une période de deux heures. Lorsque la méthode d'observation adaptative est appliquée, l'estimation de la vitesse verticale peut être améliorée dans les zones où les covariances d’erreurs sont importantes. Toutefois, l'amélioration est faible par rapport aux variables observées.

Statement of Originality

This thesis contributes to the field of radar data assimilation in the following aspects.

1. The time evolution of 1-km resolution background error statistics is examined. It is found that the error structures evolve differently for different variables, and in different regions (e.g. with or without precipitation). Moreover, once the physical parameterization scheme becomes active, these error structures change rapidly before the onset of precipitation.

2. A 1-km resolution EnKF system is implemented for radar data assimilation. Data assimilation is performed from global scale to convective-scale. It is verified that the parallel sub-EnKF method is helpful for maintaining the ensemble spread for convective-scale data assimilation. The performance of EnKF and its impact on forecast are studied for different precipitation structures.

3. This thesis explores for the first time the possibility of using phased-array technique and adaptive radar observation method to correct the unobserved model variable, for the purpose of producing a better forecast. This method can be considered as another way of using phased-array radar to improve weather prediction, from the perspective of radar data assimilation.

Acknowledgements

I would like to express my sincere appreciation to my thesis advisor Prof. Isztar Zawadzki for offering me the great opportunity to study in this field, providing me all the support I need, and giving me valuable suggestions. His patience, encouragement and inspiration guided me through this research.

I am also grateful to Dr. Luc Fillion who managed to provide me the convenience of running the data assimilation system at the Canadian Meteorological Center. He also gave many detailed professional advices on how to practically implement a complex system. His expertise in data assimilation helped me solve many problems.

I would like to thank Prof. Frédéric Fabry, Prof. M.K. Yau, and Prof. Daniel Kirshbaum who patiently listened to my presentations and gave me many advices in the group meetings. I am thankful to my college Dr. Kao-Shen Chung who had a lot of discussions with me, reviewed my articles, and provided me many suggestions.

I appreciate my colleges Dominik Jacques, Madalina Surcel, Ya-Chien Feng, Aitor Atencia, Bernat Puigdomènech Treserras, Jonathan Vogel and Seung-Jong Baek for their encouragement.

Special thanks go to my wife Wenjing Zhao and my mother Fengqin Li for their consistent supports and tremendous sacrifices. A more special thank you goes to my daughter Isabelle Yuqi Chang, who allowed me to enjoy the most wonderful moments of rocking her and writing my thesis at the same time.

Contribution of Authors

In Chapter 3, Dr. Kao-Shen Chung selected the case for the study, performed the ensemble forecasts, and analyzed the vertical background error structure and temperature tendency. The author of this thesis generated the initial conditions for ensemble forecasts, inspected horizontal spatial correlation and standard deviations of the background errors, and helped to interpret other results. Dr. Luc Fillion modified the perturbation scheme, gave suggestions and reviewed the article. Dr. Monique Tanguay modified the Limited Area Model for EnKF.

In Chapter 4, Dr. Kao-Shen Chung set up the localization parameters, helped to design the background check procedure, configured the 3-level nested model, and gave advices on data cleaning and implementing observation operator. The ensemble initial and lateral boundary conditions generated from parental EnKF system were provided by Dr. Kao-Shen Chung and Dr. Seung-Jong Baek. The author of this thesis implemented most parts of the EnKF system, performed data assimilation and short-term forecasts and analyzed the results. Dr. Luc Fillion gave many advices and reviewed the article.

In Chapter 5, Prof. Isztar Zawadzki provided the general ideal of adaptive radar observation, and gave suggestions on the experiment design. Other work was done by the author of this thesis.

The studies in Chapter 2 are performed under Prof. Isztar Zawadzki's supervision.

Contents

List of Tables

List of Figures

Chapter 1

Introduction

1.1 Ensemble Kalman Filter for atmospheric data analysis

Atmospheric data analysis is a process whereby atmospheric observations are diagnosed in order to produce a regular, coherent spatial representation of the atmosphere at a given time (Daley 1991). This analysis can be adopted as the initial condition for the time integration of a numerical weather prediction (NWP) model based on the governing differential equations of the atmosphere. The ability to make skilful predictions requires accurate analysis of the initial condition (Kalnay 2003). In order to minimize the uncertainty in analysis, data assimilation methods, such as variational and ensemble-based approaches (Daley 1991; Kalnay 2003), use statistical interpolation scheme to incorporate observations into the background that is usually produced by a numerical model.

Ensemble Kalman Filter (EnKF) is a data assimilation technique (Evensen 1994), which applies the Monte-Carlo method on a Bayesian update problem for estimating posterior probability distribution (i.e. analysis) from prior information (i.e. background) and observations, where the multivariate probability distributions are sampled by a number of model realizations (i.e. ensemble members). According to the error statistics estimated from the ensemble members, EnKF linearly combines the background and observations so as to produce an optimal analysis with minimum error variance. In order to yield this optimal estimate, the assumption that all errors follow unbiased Gaussian distributions is required by EnKF.

Besides the EnKF, another popular approach is the variational method, such as 3D-Var and 4D-Var, which obtains the best estimation by minimizing a cost function. A typical cost function sums the distance between analysis and background weighted by background error covariance matrix, and the distance between analysis and observations weighted by observation error covariance matrix (Kalnay 2003). In a 4D-Var system, an adjoint model is usually applied for transferring perturbations from analysis time to other times so as to calculate the distance between analysis and observations collected in a time span. Unlike the variational method, EnKF uses the Kalman Gain instead of a minimization process, and can work without extra effort on the governing equations, which makes it convenient and practical to use. Additionally, while the variational method demands a predetermined background error covariance matrix in cost function, EnKF uses ensemble members to provide a flow-dependent estimation of the background error statistics.

EnKF has been widely applied on atmospheric data assimilation because of its relatively simple implementation and the flow-dependent background error covariance matrix. The National Center for Atmospheric Research (NCAR) included EnKF as an analysis tool in the Data Assimilation Research Testbed (DART) (Anderson 2001, 2003, 2007, 2009; Anderson et al. 2009; Raeder et al. 2012). This EnKF system has been used on different models to assimilate a variety of observations, for the studies of hurricanes (Chen and Snyder 2006; Davis et al. 2010; Torn 2010), convective storms (Zhang et al. 2004; Dowell et al. 2010), carbon monoxide (Edwards et al. 2009; Arellano et al. 2010) and Martian atmosphere. In Canada, the Canadian Meteorological Center (CMC) implemented a global-scale EnKF system for operational use (Houtekamer and Mitchell 1998, 2001; Houtekamer et al. 2005; Mitchell et al. 2002; Mitchell and Houtekamer 2009). The comparison between different operational analysis systems at CMC suggested that EnKF had a similar performance in improving global forecasts as the 4-D variational system (Buehner et al. 2010a, b). Besides the standard EnKFs, other versions of EnKF were developed. Ensemble Transform Kalman Filter (ETKF, Bishop et al. 2001) was proposed to perform fast calculations for ensemble analyses. Szunyogh et al. (2008) employed the Local ETKF (LETKF) algorithm with the National Centers for Environmental Prediction (NCEP) global model. They found that the LETKF provided more accurate analyses than the spectral statistical interpolation analyses in sparse observation regions. The Italian National Meteorological Service also applied the LETKF in regional NWP (Bonavita et al. 2010). It was shown that the LETKF generally outperformed their operational 3D-variational system, according to the root-mean-square error verification for the forecasts. In addition, Ensemble Square Root Kalman Filter (EnSRF, Whitaker and Hamill 2002; Tippett 2003; Evensen 2004) was introduced as an alternative method to ETKF and EnKF.

Despite its superiority and popularity, one of the most problematic issues with EnKF is the violation of its assumption on the Gaussian distributed errors due to the nonlinearity of the NWP model. A few approaches, such as Ensemble Adjustment Kalman Filter (EAKF, Anderson 2001) and EnSRF (Evensen 2004) consider higher-order moments of the prior possibility density function and maintain the Gaussian distribution in analysis errors. Additionally, the particle filter (Snyder et al. 2008) does not use the first and second moments to parameterize the probability density function (pdf), but samples the entire pdf by a large number of ensemble members. Thus this scheme relaxes the Gaussian distribution assumption. However, it is impractical because it requires a large ensemble size which scales exponentially with the variance of the observation log likelihood.

The practical implementation of an EnKF system usually includes a few specific algorithms. Firstly, because of the limited ensemble size, it is difficult to precisely represent the complete multivariate probability distribution by ensemble members, which may result in underestimated variances and noisy covariances. In order to increase the variance and the ensemble spread, inflation methods (Anderson and Anderson 1999; Anderson 2007) are used in DART; and multiple parallel sub-EnKFs are applied at CMC (Houtekamer and Mitchell 1998, 2001). Moreover, the localization methods are used to remove or reduce the noises in covariance estimations (Anderson 2007; Bishop and Hodyss 2010; Greybush 2011; Anderson and Lei 2013). Secondly, due to the limited computer power, observations are usually assimilated one by one (as in DART) or batch by batch (as in the global EnKF at CMC) for reducing the computational cost. However, this procedure is only valid when observation errors are uncorrelated in space. Thirdly, in order to avoid the reduction of ensemble spread after each analysis step, observations need to be perturbed according to their error statistics (Whitaker and Hamill 2002).

In meso and convective scales, EnKF has been applied on the assimilation of simulated radar data. The first attempt was made by Snyder and Zhang (2003) who assimilated simulated radial velocities into a perfect cloud-scale model. The study showed that precise analysis could be produced after six cycles of assimilation. The research also indicated that flow-dependent error covariances are important for reconstructing the storm structure in detail. Tong and Xue (2005) applied EnKF on the assimilation of both simulated radial velocity and reflectivity observations. They showed that reflectivity data in precipitation areas help to retrieve storm details, and no-reflectivity observations in non-precipitation areas are useful for suppressing false alarm storms. Caya et al. (2005) compared EnKF and the variational method. The results of this comparison demonstrated that EnKF was slightly better than 4-D variational method after a few cycles due to the flow-dependent background ensemble members in EnKF. Xue et al. (2006) applied EnSRF for radar data assimilation within the framework of Observing System Simulation Experiments (OSSEs). They found that EnSRF is superior to other traditional retrieval schemes because the sensitivity of the EnSRF analysis to the volume scan interval is less, and frequent update of model state does not hurt the balance in the analysis. Additionally, EnSRF can also be applied on radar data assimilation to retrieve microphysical parameters (Tong and Xue 2008a, b).

Compared to simulated observations, assimilating real radar data by EnKF is even more challenging due to the imperfect highly non-linear model, phase error of backgrounds, non-continuous observations, and the limited knowledge of model and observation errors. Dowell et al. (2004) tested the feasibility of using EnKF to retrieve wind and temperature fields in an isolated convective storm from single radar observations. The results showed that the retrieval was sensitive to the initial perturbations, and the low level temperature was difficult to retrieve, which was likely caused by observation error and model error near the surface. Aksoy et al. (2009) used EnKF to assimilate real radar observations of radial wind and reflectivity collected by multiple radars. It is shown that although the amplitude of innovations (i.e. observations minus background) in each cycle was consistently reduced, the analysis result was still far from optimal, as the ensemble spread was consistently smaller than expected. They also claimed that the representation of mesoscale uncertainty in the initial perturbations is critical for the assimilation system. In their experiment on EnKF-based forecasts (Aksoy et al. 2010), they indicated that while radar data assimilation is able to partially mitigate some of the negative effects in some situations, the forecast skill decays on a time scale of tens of minutes. Dowell et al. (2011) examined the influences of real reflectivity observations in EnKF data assimilation. They demonstrated that storms developed more quickly when both radial velocity and reflectivity are assimilated, rather than only velocity.

Furthermore, the advanced phased-array technology allows radar to adaptively collect observations, by electronically steering the radar beam. Such radar provides the new phased-array radar data, whose spatial resolution, temporal resolution, accuracy and locations can be adjusted in a flexible manner (Heinselman et al. 2011). From the application of EnKF on phased-array radar data assimilation, Lu and Xu (2009) found that reducing the spatial resolutions and enhancing the temporal resolution and/or measurement accuracy can reduce or eliminate information redundancy and enhance the information content. Yussouf and Stensrud (2010) claimed that assimilating simulated phased-array radar data by EnKF at 1-min intervals over a short 15-min period yielded significantly better results than assimilating traditional radar data. These studies explored the possibility of improving EnKF analysis by adaptive radar observation.

1.2 Motivation and Research Objectives

In most EnKF applications for real radar data assimilation, the analysis is usually far from optimal (Aksoy et al. 2009) and the improvement on forecast is always short-lived (Aksoy et al. 2010; Surcel et al. 2014). These weaknesses in EnKF are related to the uncertainties involved in the system, such as initial perturbation, ensemble spread and model errors (Dowell et al. 2004). Therefore the first objective of this research is to inspect the impact of all the uncertainties involved in EnKF data assimilation, in order to better understand the unappealing analysis result, and provide advices for implementing a sophisticated EnKF radar data assimilation system. While the forecast error statistics can be estimated from ensemble members, other uncertainties including the first guess, the initial ensemble perturbations, and the estimations of model and observation errors, are related to prior knowledge obtained from climatology and experiences. The author would like to examine the evolution of the forecast error in a complex model, and investigate the influence of other uncertainties on EnKF by idealized simple experiments.

Based on the studies about the uncertainties in EnKF, the second objective of this research is to implement an EnKF system dedicated to real radar data assimilation. Although some EnKF studies already dealt with radar observations, most of the focus was on simulated observations or real observations collected from isolated convective systems happening within the model domain. Consequently, the performance of real radar data assimilation by EnKF under different weather conditions is still not clear. The author would like to build a high resolution EnKF for assimilating real radar data; carefully study the performance of EnKF under varying weather conditions; and evaluate the advantages and limitations of EnKF from the perspectives of both analysis accuracy and forecast precision.

The third objective of this research is to improve EnKF radar data assimilation by adaptive radar observation. Studies about adaptive observation have shown that changing observation locations has the potential to reduce analysis and forecast uncertainties (Palmer et al. 1998, Buizza and Montani 1999, Bishop et al. 2001, Majumdar et al. 2002). In regards to radar data, modern radar employing phased-array technique is able to sample the atmosphere adaptively in space and time as required by the user, since the radar beam can be electronically steered by adjusting the phases of an array of antennas. Given such a powerful device, one needs to decide the optimal data collection strategy, so that the uncertainty in analysis and forecast can be minimized by data analysis. It is known that the forecast quality relies on some model variables that cannot be observed by radar. For example, vertical velocity is important for a successful precipitation forecast but can hardly be observed by radar. In order to reconstruct such a model field by data assimilation, significant and reliable cross-covariances between errors of observed and unobserved variables in the background are required (Snyder and Zhang 2003). Given the advanced radar technology, the author would like to explore the possibility of using EnKF and adaptive radar observation method to improve forecast based on the background error cross-covariances between unobserved and observed variables.

1.3 Thesis structure

The subsequent chapters are organized in the following manner.

Chapter 2 studies the influence of EnKF uncertainties and the effectiveness of observations on data analysis, in order to give advices on the implementation of EnKF system, and the optimal observation collection method. The uncertainties exists in the estimation of background error, the estimation of initial guess error, the model error and the representation of model and observation errors. Additionally, this chapter will discuss the impact of observation density, observation number and observation accuracy on the analysis step of EnKF.

Chapter 3 examines the forecast error statistics estimated from a set of ensemble members under the framework of a high resolution EnKF system with a focus on the very early stage of transition from purely homogeneous isotropic background-error structures to situation-dependent error correlations. The error structures in the regions with and without precipitations are also compared.

Chapter 4 introduces a high resolution (1-km) EnKF system which assimilates real radial velocity observations into a limited area model. Short-term ensemble forecasts are initiated from the ensemble analyses after the cycling process is complete. The impact of data analysis on forecast is investigated in three summer cases with different precipitation structures.

Chapter 5 proposes an adaptive radar observation method which aims at improving the unobserved field from the assimilation of simulated radar data by EnKF. This method takes advantage of hypothetical phased-array radar to adaptively place observations where the unobserved variable is most likely to be improved.

In Chapter 6, conclusions, further discussions and future work are presented.

Chapter 2

Studies on the Influence of Uncertainties and the Effectiveness of Observations on Ensemble Kalman Filter by Idealized Experiments

Before the implementation of Ensemble Kalman Filter (EnKF) for real radar data assimilation, a few idealized experiments are conducted in this chapter to study the influence of uncertainties and the effectiveness of observations on data analysis. The uncertainties about the estimation of background error, the estimation of initial guess error, the model error and the misrepresentation of model and observation errors are examined. The impact of observation density, observation number and observation accuracy will be discussed. Results from this study give advices on the implementation of EnKF system, and the optimal observation collection method.

This chapter is based on the following conference articles, presentations and posters.

Chang, W., and I. Zawadzki, 2011: Targeted observations for radar data assimilation. 18A.2, 35th Conference on Radar Meteorology, Pittsburgh, PA, USA.

Chang, W., and I. Zawadzki, 2012: Impact of Ill Estimated Error Structures on Ensemble Kalman Filter. 2C1.6, 46th CMOS Congress, Montreal, QC, Canada.

Chang, W., and I. Zawadzki, 2012: The Value of Accuracy and Density of Radar Observation for Data assimilation. The Seventh European Conference on Radar in Meteorology and Hydrology. Toulouse, France.

Chapter 2

Studies on the Influence of Uncertainties and the Effectiveness of Observations on Ensemble Kalman Filter by Idealized Experiments

2.1 Introduction

The quality of data analysis relies on the accuracy of three pieces of information: the background (i.e. model forecast), observations and their error statistics. One of the most popular statistical data analysis schemes, the Ensemble Kalman Filter (EnKF), calculates background error statistics from a set of ensemble members and linearly combines the background and observations, according to the statistical properties of their errors in order to minimize the uncertainties in its analysis of the atmosphere state. Among the three informational components, Numerical Weather Prediction (NWP) models are usually used to provide the background. The models including the Weather Research and Forecasting (WRF) model and the Global Environmental Multiscale (GEM) model are developed and persistently improved for both research and operational use. In regards to the observations, radiosondes, aircrafts, ships, satellites, ground based radars and other observation platforms collect increasing amount of data, and quality control is usually applied so as to reduce observation errors. Given the background and observations, the error statistics, including variances and covariances, determine the weights assigned to these two parties and decide the analysis uncertainty. Since there are already a vast discussion on improving NWP models, this chapter focuses on the impact of the error statistics and the observations on data analysis, within the EnKF framework.

Although EnKF uses ensemble members for forecast error estimation, nevertheless many other errors and uncertainties involved in EnKF cannot be estimated in this way. Firstly, uncertainty exists in the estimated statistics of forecast (or background) errors, which are computed from the differences between ensemble members and the ensemble mean (Evensen 2003; 2006). Because the ensemble mean is always different from the unknown truth, the uncertainty mentioned above cannot be eliminated, but probably can be reduced if ensemble mean is closer to the truth. The second source of uncertainty comes from model error estimation which is usually related to climatology and some existing analysis results (Mitchell and Houtekamer 1999; Mitchell et al. 2002; Houtekamer et al. 2009). Thirdly, the estimation of observation error statistics could be inaccurate. For example, the spatial error correlation of radar data is not well known (Fabry 2011), and has to be ignored in EnKF, thus leading to the requirement of data thinning (Aksoy et al. 2009; Dowell et al. 2011). Lastly, the initial error estimation of the first guess is also imprecise at the beginning of EnKF, because the first guess is usually far from the truth, which itself is unknown. This uncertainty may lead to the inappropriate generation of the initial ensemble spread. All the errors and uncertainties discussed above have the potential to weaken the data analysis results, and therefore need to be investigated for the benefit of a careful EnKF system implementation.

From the perspective of data collection, a well-designed observation system is also beneficial for data analysis. For example, it has been shown that assimilating data from an adaptive observation platform is helpful for reducing errors in both analysis and forecast (Palmer et al. 1998, Buizza and Montani 1999, Bishop et al. 2001, Majumdar et al. 2002). An adaptive radar observation system (e.g. phased-array radar) is able to adaptively adjust temporal resolution, spatial resolution, locations and accuracy of the data, but still requires an optimal data collection strategy in order to mostly reduce analysis and forecast uncertainties. Although it might seem obvious that a larger number of more precise observations would help to better understand the atmosphere, their impact on data analysis is not actually that straightforward. For example, when radar data become denser in space, the observation errors are strongly correlated to contain more mutual information, which results in less benefit to the reduction of analysis uncertainty (Lu and Xu et al. 2006). The data from adaptive radar observation platforms also face this problem of deciding between observation accuracy and observation number (Heinselman et al. 2011). In other words, the improvement of one comes at the sacrifice of the other, given a limited radar canning capability. Therefore, in order to decide the optimal observation strategy, the effectiveness of both observation accuracy and observation number on the analysis must be examined.

This chapter will conduct a few idealized experiments about EnKF data assimilation. Furthermore, if the system is linear, the Kalman Filter will be used. The uncertainty of analysis is used to evaluate the system's performance.

In the next section, the EnKF algorithm is introduced. The third section examines the impact of uncertainties on data assimilation system, which includes: the uncertainty in background error estimation due to the difference between the ensemble mean and the truth, the poor estimation of errors in the first guess, the model error, and the misrepresentation of model and observation errors. The fourth section studies the influence of observation information on data analysis, including observation spacing, observation number, and observation accuracy. Finally, the summary and discussions are presented in the last section.

2.2 The algorithm of the Ensemble Kalman Filter

EnKF is a sequential data assimilation method that applies an ensemble of model integrations to predict error statistics in the forecast, and then uses those error statistics to directly update the ensemble of model states when observations are assimilated. Evensen (2003) provides the theoretical formulation and practical implementation of EnKF. The Monte-Carlo realization of EnKF usually starts from a set of initial ensemble forecasts $\mathbf{X}_j^f$ (j = 1, 2 … N, indicating the ensemble member index), which are produced by

$$\mathbf{X}_j^f = \mathcal{M}(\mathbf{X}_j^a) + \varepsilon_j \tag{2.1}$$

where $\mathcal{M}$ denotes the nonlinear model equation; ε_j is the perturbation for model error, which follows zero-mean Gaussian distribution with covariance matrix $\mathbf{Q}$; $\mathbf{X}_j^a$ is the analysis ensemble member from the previous assimilation step. For the first assimilation cycle, where analysis members are not available, $\mathbf{X}_j^a$ indicates the perturbed model initial condition for ensemble forecasts.

Given a set of ensemble members, the error variance and covariance matrix can be estimated by

$$var(\mathbf{A}_j, \mathbf{B}_j) = \frac{1}{N-1} \sum_{j=1...N} (\mathbf{A}_j - \overline{\mathbf{A}})(\mathbf{B}_j - \overline{\mathbf{B}})^T \tag{2.2}$$

where **A** and **B** represent state vectors (the elements in the vector represents each model variable at each grid point) for different members in model space (e.g.: $\mathbf{X}_j^f, \mathbf{X}_j^a$) or in observation space (e.g.: $\mathbf{HX}_j^f, \mathbf{HX}_j^a$); the over bars indicate the mean of the vectors over all ensemble members. Given the estimation of the error covariance matrix, the Kalman Gain can be calculated from

$$\mathbf{K} = var(\mathbf{X}_{j'}^f, \mathbf{HX}_{j'}^f)(var(\mathbf{HX}_{j'}^f, \mathbf{HX}_{j'}^f) + \mathbf{R})^{-1} \tag{2.3}$$

where $\mathbf{H}$ is the observation operator mapping model space to observation space; $\mathbf{R}$ is the observation error covariance matrix; and $\mathbf{K}$ is Kalman gain.

After the Kalman gain is calculated and observation vector $\mathbf{O}$ is provided, EnKF is able to produce the analysis result for each ensemble member by

$$\mathbf{X}_j^a = \mathbf{X}_j^f + \mathbf{K}(\mathbf{O}_j - \mathbf{HX}_j^f) \tag{2.4}$$

In order to avoid the underestimation of observation errors, observations $\mathbf{O}$ need to be perturbed to $\mathbf{O}_j$ according to the observation error covariance matrix $\mathbf{R}$ (Burgers et al 1998). Observation perturbation is a routine process in the EnKF system, because assimilating the same unperturbed observations into different ensemble members leads to insufficient analysis ensemble spread. Additionally, Whitaker and Hamill (2002) proved that EnKF is equivalent to linear Kalman Filter under a necessary condition that the observations are perturbed.

The forecast and analysis error covariance matrices can be estimated from ensemble members by

$$\mathbf{P}^f = var(\mathbf{X}_j^f, \mathbf{X}_j^f) \tag{2.5}$$

$$\mathbf{P}^a = var(\mathbf{X}_j^a, \mathbf{X}_j^a) \tag{2.6}$$

where $\mathbf{P}^f$ and $\mathbf{P}^a$ represent error covariance matrix for forecast and analysis, respectively. If the observation operator is linear, and errors follow an unbiased Gaussian distribution, the analysis error covariance matrix can be written as

$$\mathbf{P}^a = (\mathbf{I} - \mathbf{K}\mathbf{H})\mathbf{P}^f = \mathbf{P}^f - \mathbf{P}^f\mathbf{H}^T(\mathbf{H}\mathbf{P}^f\mathbf{H}^T + \mathbf{R})^{-1}\mathbf{H}\mathbf{P}^f \tag{2.7}$$

After data assimilation, the analysis error represented by the ensemble member should be lower than either the forecast error or the observation error.

2.3 Examination of the uncertainties in EnKF

In this subsection, simple experiments are performed to examine the influence of forecast error estimation with respect to ensemble mean, the error estimation of the first guess, the model error, and the misrepresentation of model and observation errors on data analysis, based on an EnKF system. In this experiment, the one-dimensional viscid Burgers' equation is used as the forecast model, which is

$$\frac{\partial u}{\partial t} + u\frac{\partial u}{\partial x} = D\frac{\partial^2 u}{\partial x^2} \tag{2.8}$$

where u is the control variable of velocity having an extension of 1000 points in one dimension; x is the distance in space; D is the viscosity coefficient which is set to be 0.12 in this experiment; and t is time. The leapfrog integration scheme is used for producing numerical solutions.

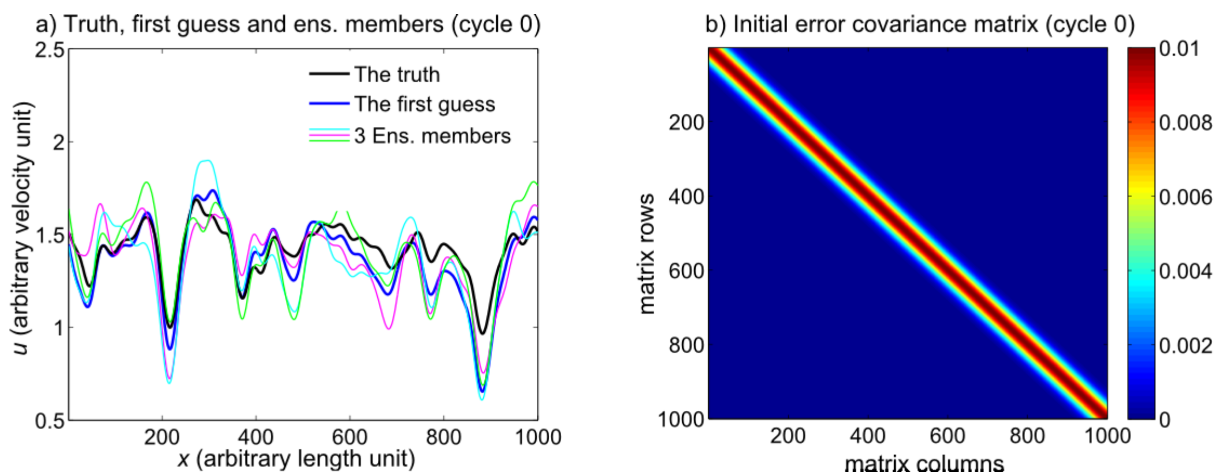

Fig. 2.1 a) 1-D fields of the truth, the first guess and three ensemble members at cycle 0, before data assimilation starts. b) Error covariance matrix used for generating the first guess from the truth, and for generating initial ensemble members from the first guess, at cycle 0. Each pixel represents an element in the error covariance matrix. The diagonal points represent variances; and the off-diagonal points represent spatial covariances.

The experiment starts at cycle 0, when a smoothed 1-D random field serves as the “true” initial condition of Eq. (2.8) as shown in Fig. 2.1a. In reality, the truth is not exactly known. Instead, a first guess, which could be a model output or an analysis from another assimilation system, is used for producing ensemble members. In this study, the first guess is generated via adding random errors to the truth (Fig. 2.1a). The initial 64 ensemble members are then produced by randomly perturbing the first guess. Both the errors on the first guess (the difference between the first guess and the truth) and the random perturbations (the difference between ensemble members and the first guess) follow a zero-mean Gaussian distribution with the error covariance matrix as presented in Fig. 2.1b. The diagonal element of an error covariance matrix represents variance, and the non-diagonal element is the covariance between any two grid points. Both the ensemble members and the truth are then used to initialize model integrations.

Table 1.1 List of experiment setup

	Exp in a) section	Exp in b) section	Exp in c) section	Exp in d) section
Model	One-dimension viscid Burgers' equation (Eq. 2.8)			
Observation	50 observations, truth + random error (no spatial correlation)			
Bkgd error estimation	With respect to the ensemble mean and to the truth.	With respect to the ensemble mean.	Same as in b)	Same as in b)
Error estimation of the first guess	Well estimated.	Misrepresented.	Same as in a)	Same as in a)
Model error	No model error	Same as in a)	Well estimated model error	Misrepresented model error.
Obs error	Well estimated	Same as in a)	Same as in a)	Misrepresented

After numerical integration of Eq. (2.8), ensemble forecasts (or background) and the truth are yielded at cycle 1. Fifty observations evenly spaced along x are then generated via the addition of Gaussian distributed random errors to the truth. The observation errors have a standard deviation of 0.06 and are uncorrelated in space. Fig. 2.2a shows the ensemble mean forecast, observations, and the truth at cycle 1, based on which, the EnKF equations (2.2) – (2.6) are applied, in order to perform data assimilation and estimate error statistics. The ensemble analyses are then used as model initial conditions for the ensemble forecast of the next cycle. Such cycling process is applied from cycle 1 to cycle 12. Note that the term ‘forecast’ is exactly the same as ‘background’ in this chapter since the forecast initiated at current time step will be used as background for the next time step.

Based on the above experiment procedure, the following four subsections use several experiment setups to perform data assimilation, as summarized in Table 1.1. More details can be found in the corresponding subsections.

a. The use of ensemble mean for forecast error estimation

In practice, the ensemble mean is usually considered to be the reference for the computation of error covariance matrix, as expressed in Eq. (2.2). If the truth is known, a more precise estimation of error statistics can be given by

$$var(\mathbf{A}_j, \mathbf{B}_j) = \frac{1}{N} \sum_{j=1 \ldots N} (\mathbf{A}_j - \mathbf{A}_t)(\mathbf{B}_j - \mathbf{B}_t)^T \tag{2.9}$$

where the subscript t indicates the truth, other notations are the same as in Eq. (2.2) (Evensen 2003). In reality, however, Eq. (2.9) is not applicable, as the truth is unknown. Therefore, while EnKF uses ensemble members and their mean to represent the forecast error statistics, such a representation is less reliable if the ensemble mean is far from the truth.

In order to examine the reliability of forecast error estimation by the ensemble mean, two experiments are conducted and compared: the first one uses ensemble mean as the reference to calculate the forecast error covariance matrix in EnKF (Eq. 2.2), while the second one uses the truth as the reference (Eq. 2.9). Since our focus in on the forecast error statistics represented by ensemble members, no model error is considered.

At cycle 1, before the first analysis step is performed, the truth, 50 observations and the ensemble mean forecast (i.e. background) are shown in Fig. 2.2a. Figure 2.2b displays the forecast error standard deviations with respect to the truth (blue dashed curve), and with respect to the mean (blue solid curve). Figure 2.2 suggests that the forecast ensemble spread is ‘enough’ to cover the truth, since the forecast error standard deviations are comparable to or larger than the difference between the ensemble mean and the truth. Moreover, the error standard deviation estimated from the truth (blue dashed curve in Fig. 2.2b) is much larger than the one estimated from the ensemble mean (blue solid curve in Fig. 2.2b), because the former contains the difference between the ensemble mean forecast and the truth.

Two data assimilation experiments are performed at cycle 1 to produce the ensemble analyses. While the first experiment calculates the background error covariance matrix with respect to the *mean*, the second experiment computes it with respect to the *truth*. After data assimilation, the standard deviation of the analysis with respect to the *truth* is plotted for both experiments in Fig. 2.2b (red dashed curve for the second experiment, red solid curve for the first experiment). Note that the *truth* is used as reference in both experiments for estimating the analysis uncertainty. In addition, the ensemble mean analysis for the first experiment is plotted in Fig. 2.2a (red curve).

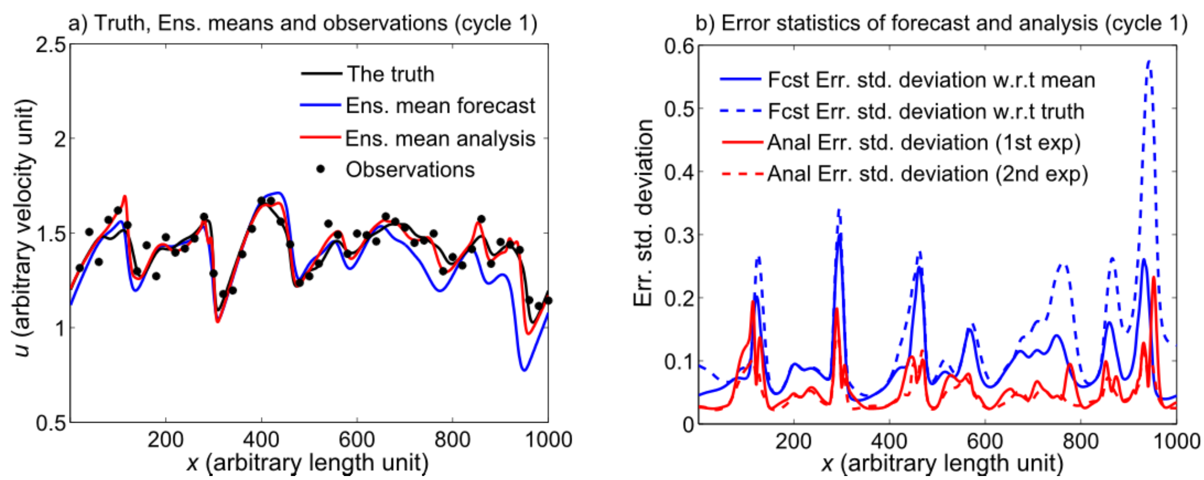

Fig. 2.2 a) 1-D fields of the truth, the observations, the ensemble mean forecast and the ensemble mean analysis at cycle 1. b) Forecast error standard deviations with respect to the truth and the mean, analysis error standard deviations with respect to the truth in two experiments (the 1st experiment uses $\mathbf{P}^f$ with respect to the mean to calculate Kalman gain; the 2nd experiment uses $\mathbf{P}^f$ with respect to the truth).

Figure 2.2a shows that after data assimilation, the ensemble mean of the analyses is driven closer to the observations, as compared to the ensemble mean of the forecasts. The analysis uncertainties in the two experiments are also generally smaller than the forecast uncertainties, as indicated by the error standard deviations plotted in Fig. 2.2b. Moreover, the analysis from the first experiment has a slightly larger uncertainty than the second experiment at most points, although the estimated forecast uncertainty is smaller in the first experiment. This is because the forecast error calculated from the ensemble mean is underestimated in the first experiment, while the one estimated with respect to the truth is more reliable (Evensen 2003; 2006). More explicitly, the forecast error variance calculated with respect to the mean is underestimated, or smaller than the variance calculated with respect to the truth. This is because: after integrating a nonlinear model, the ensemble mean deviates from the truth even if they are identical at the initiation time; and the variance with respect to mean is always minimal.

When the ensemble mean is closer to the truth, the estimation of error statistics with respect to the mean (as in most ensemble-based data analysis systems) is more precise, which in turn leads to a more accurate ensemble mean in the analysis. In order to assess the quality of the ensemble mean analysis, the root mean square (rms) error with respect to the truth can be computed via

$$rms = \sqrt{\frac{1}{M} \sum_{m=1\ldots M} \left(\overline{u}_{m,a} - u_{m,t} \right)^2} \tag{2.10}$$

where m represents the location index in the 1-D field; $M = 1000$ is the 1-D extension; $\overline{u}_{m,a}$ is the ensemble mean of analysis at location m; $u_{m,t}$ is the truth at location m.

The rms errors of the ensemble mean analyses at each cycle are presented by Fig. 2.3. The black curve shows that the EnKF converges after 4 assimilation cycles, as the forecast error covariance matrices are precisely estimated from the truth. In contrast, the blue curve implies that the EnKF converges much slower when the forecast errors are underestimated from the ensemble mean. However, since the ensemble mean is brought closer to the truth after each cycle, the error estimation with respect to the mean gradually becomes more reliable, which leads to even more precise analysis results.

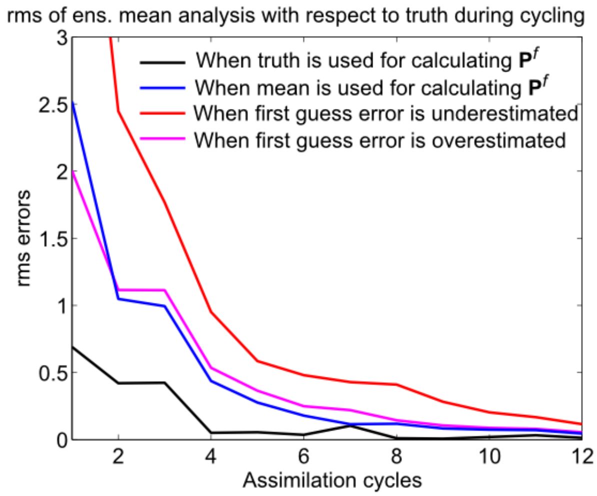

Fig. 2.3 rms errors of ensemble mean analysis with respect to the truth during 12 cycles, for the experiments where $\mathbf{P}^f$ is estimated with respect to the truth and the ensemble mean, and for the experiments where the error of the first guess is underestimated / overestimated.

b. The error estimation of the first guess.

In contrast to the forecast error covariance matrix, which can be estimated from ensemble members, the initial error covariance matrix describing the error of the first guess is usually obtained from a prior knowledge, such as climatology. Thus it could be incorrectly estimated. In this subsection, the errors of the first guess are underestimated and overestimated in two EnKF experiments, which affects ensemble spread in the initial members. Other experiment settings are shown in Table 1.1. Note that the forecast errors for Kalman gain calculation are estimated from the ensemble mean. By the end of each cycle, the rms errors of ensemble mean analyses are calculated, as in the previous subsection.

When the error of the first guess is overestimated by a factor of 2, Fig. 2.3 (pink curve) shows that the rms error of the ensemble mean analysis exhibits a similar performance as in the other experiment where the error of the initial guess is well estimated (blue curve). At some cycles (2 – 9), the analysis uncertainty is obviously larger.

When the error of the first guess is underestimated by a factor of 0.4, the rms error of the ensemble mean analysis converges to the zero line much slower than other experiments, as displayed in Fig. 2.3 (red curve). This is because EnKF falsely gives more credits to the forecast and reduces the influence of observations. Consequently, it is difficult to correct the ensemble mean of analyses, even after 12 assimilation cycles.

c. The model error.

The forecast error in EnKF is composed of two parts: the error transferred from the initial condition (i.e. the analysis in the previous cycle) and the error caused by the imperfect model (i.e. model error). In order to investigate the impact of having model error on data analysis, this experiment includes a model error of standard deviation 0.01, and assumes that model error is well estimated in EnKF. Such an error is represented by random fields and is added to the ensemble members before the analysis steps, as shown in Eq. (2.1). Other experiment settings are kept the same as in the previous subsections (see Table 1.1).

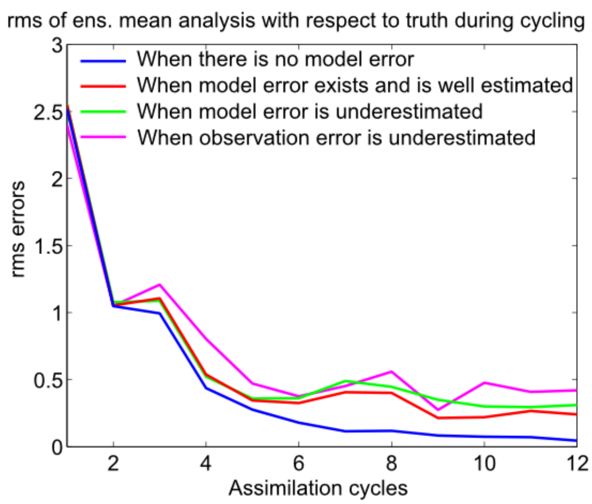

Fig. 2.4 rms errors of ensemble mean analysis with respect to the truth during 12 cycles, for the experiment where there is no model error; the experiment where model error exists and is well estimated; the experiment where model error is misrepresented; and the experiment where observation error is misrepresented.

The rms errors of ensemble mean analysis with respect to the truth in each cycle are plotted in Fig. 2.4. The results from subsection 2.3c (blue curve in Fig. 2.3) is also plotted as a reference for comparison. Despite being well known, after model error is included in EnKF system, the uncertainty of analysis is larger in each cycle, as compared to the experiment without model error (blue curve). This is because the model error adds more uncertainties to the system at each model integration step of the cycling process. In the first two cycles, the impact of having model error is minor (red curve close to the blue curve), because at the beginning of EnKF, the forecast errors are mostly caused by initial conditions rather than model errors.

d. The misrepresentation of model and observation errors

In reality, model and observation error statistics are not completely known. The former is usually estimated from previous model outputs (e.g. adaptive model error estimation scheme) or climatology, which is not as precise as in the previous subsection. Knowledge of the latter is also sometimes limited. For example, the errors of radar data are spatially correlated, but their correlation structure is difficult to estimate.

In order to examine the impact of misrepresentation of model and observation errors, two experiments are performed in this subsection. In the first experiment, the model error is underestimated by a fact of 0.4 in terms of its standard deviation, while the observation is well estimated. In the second experiment, the model error is well estimated, but the observation error standard deviation is underestimated by a factor of 0.4. Other settings are the same as before (see Table 1.1).

The rms errors of ensemble mean analyses are shown in Fig. 2.4. When model error is underestimated, EnKF falsely assigns more credits to the forecasts and the corresponding analysis has more uncertainty. As shown in the figure, the impact of the ill-estimated model error is evident after the fifth cycle (the green curve is above the red one). This is because the forecast errors are dominated by model errors. Similarly, if the observation error is underestimated, the rms errors of the ensemble mean analysis (pink curve) converge to a much higher value, as compared to the other experiments.

2.4 The effectiveness of observations on data analysis

The impacts of observation density, observation number, and observation accuracy on the analysis step of EnKF are studied in this chapter. Since we target on the analysis step, the cycling process is not performed in the following experiments. Due to the fact there is no nonlinear models or nonlinear observation operators in the following experiments, the linear Kalman Filter equations can be used. Accordingly, the analysis and its uncertainty can be produced by

$$\mathbf{K} = \mathbf{P}^f \mathbf{H}^T (\mathbf{H}\mathbf{P}^f \mathbf{H}^T + \mathbf{R})^{-1} \tag{2.10}$$

$$\mathbf{X}^a = \mathbf{X}^f + \mathbf{K}(\mathbf{O} - \mathbf{H}\mathbf{X}^f) \tag{2.11}$$

$$\mathbf{P}^a = (\mathbf{I} - \mathbf{K}\mathbf{H})\mathbf{P}^f \tag{2.12}$$

where the notations are the same as in the EnKF equations. The trace of analysis error covariance matrix $tr(\mathbf{P}^a)$ (or the total analysis error variance) is used to indicate the analysis uncertainty.

a. Observation spacing

Observation spacing describes the closeness between observations, and decides the observation error correlations. In this experiment, the spatial correlation of observation errors follows

$$\rho = \exp(-\frac{x^2}{r^2}) \tag{2.13}$$

where x indicates the distance between two observations and r is the observation error decorrelation distance; ρ is the spatial correlation between two observation errors. This equation shows that an increase in closeness between two observations results in greater correlation between their errors.

In the data assimilation system of this experiment, background is a one-dimensional field, the size of which is 200. The initial background error follows an unbiased Gaussian distribution with variance being 1, and decorrelation distance being 15, as in Eq. (2.13). The observations are available at only two points in the 1-D field, the distance between which is variable. Observation error statistics are the same as the background errors. Given the above information, data assimilation can be performed by Eqs. (2.10) - (2.12), which yields the analysis error covariance matrix.

In this experiment, varying the distance between observations is equivalent to modifying of the observation operator **H**. Accordingly, different analysis results are produced. Figure 2.5a shows that the error variance is 1 in the background before the performance of data assimilation. Assimilating two nearby observations (pink curve in Fig. 2.5a) corrects fewer points than assimilating observations that are far away from each other. Therefore the total analysis error variance is a function of the distance between two observations, as shown in Fig. 2.5b. As compared to the total background error variance $tr(\mathbf{P}^f)$ of 200, the total analysis error variance $tr(\mathbf{P}^a)$ varies from around 186 (when two observations are very close) to around 172 (when two observations are far away). Fig. 2.5b also shows that the optimal observation spacing should be at least 60 points between the two observations.

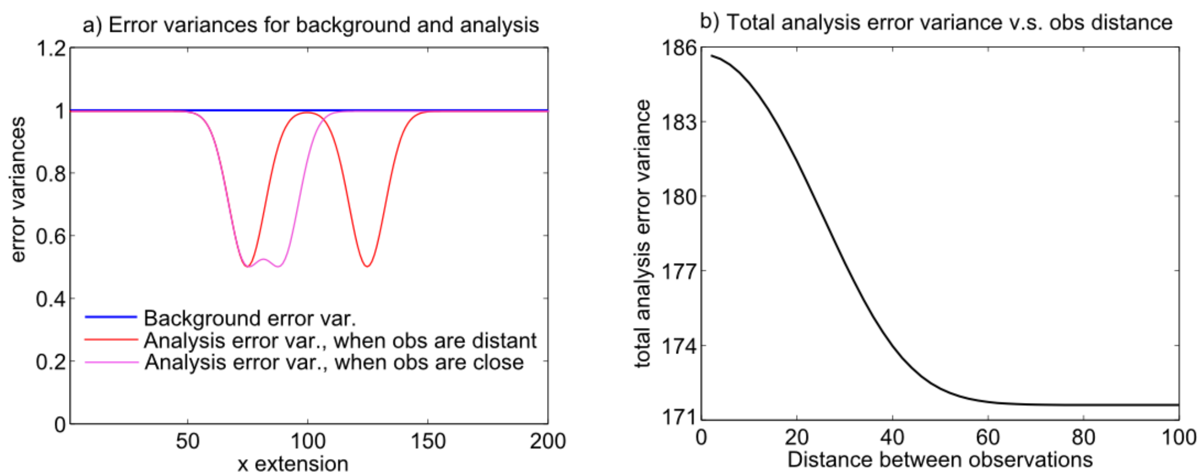

Fig. 2.5 a) Background error variances and analysis error variances when two observations are far from each other, and when they are close to each other. b) Total analysis error variance $tr(\mathbf{P}^a)$ against the distance between two observations.

In fact, the decorrelation distances of background error and observation error affects the optimal observation spacing. For example, when the decorrelation distances are 15 points for both background errors and observation errors, the 'minimum' optimal observation distance is 60 points, as discussed above. But when these decorrelation distances vary, the minimum optimal observation distance is changed accordingly. Fig. 2.6a shows the minimum optimal distance against the background and observation error decorrelation distances (their error variance is fixed to be 1). The corresponding total analysis error variance $tr(\mathbf{P}^a)$ is also presented in Fig. 2.6b. Figure 2.6a also shows that when the background error decorrelation distance is large, two observations can be placed further away because more points can be updated by background error correlation. When the observation error decorrelation distance is large, observations also need to be far from each other because too much mutual information is provided if they are close together. Figure 2.6b shows that $tr(\mathbf{P}^a)$ is more sensitive to background error decorrelation distance than to observation error decorrelation distance. A larger background error decorrelation distance leads to smaller analysis uncertainty, as because more points in the background can be updated through the background error correlation.

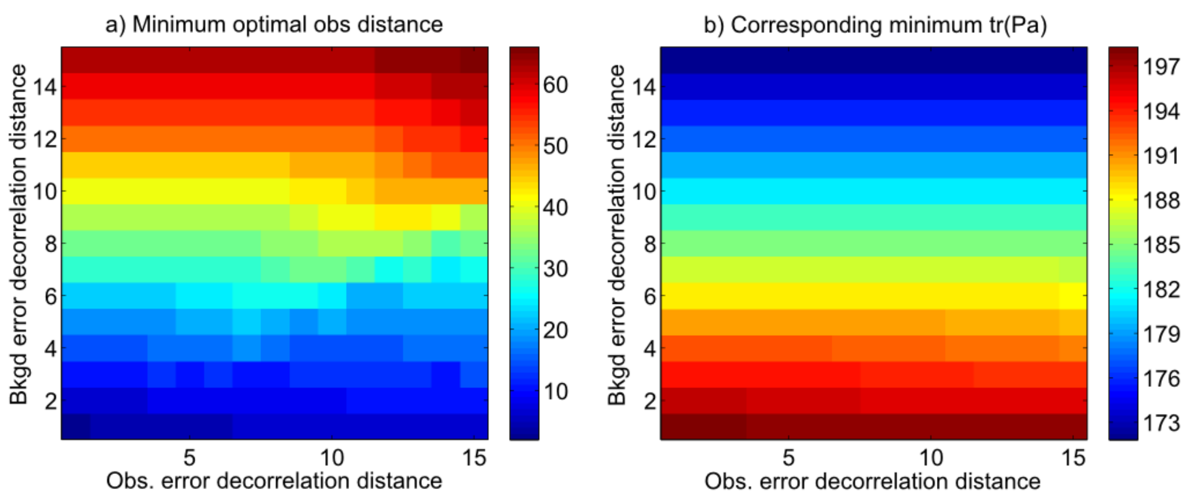

Fig. 2.6 a) The minimum optimal observation distance as a function of the error decorrelation distances of background and observation. b) The total analysis error variance $tr(\mathbf{P}^a)$ when the minimum optimal observation distance is reached.

In addition, the minimum optimal observation distance is also related to error variances of background and observation. In this exercise, the decorrelation distance is 5 grid points for both background and observation errors, but with a range of variances. Figure 2.7a shows that greater distance between two observations is needed if observation error variance is smaller or if background error variance is larger. Figure 2.7b uses the ratio $tr(\mathbf{P}^a)$ to $tr(\mathbf{P}^f)$, instead of the absolute value of $tr(\mathbf{P}^a)$, to evaluate the quality of analysis, because the background error variances are not fixed. Figure 2.7b shows that a larger observation distance (required by smaller observation error variance or larger background error variance as in Fig. 2.7a) leads to a more precise analysis. This is because: firstly, smaller observation error variance provides more reliable information to the model states and reduces the error; secondly, the larger background error variance allows stronger influence from the observations.

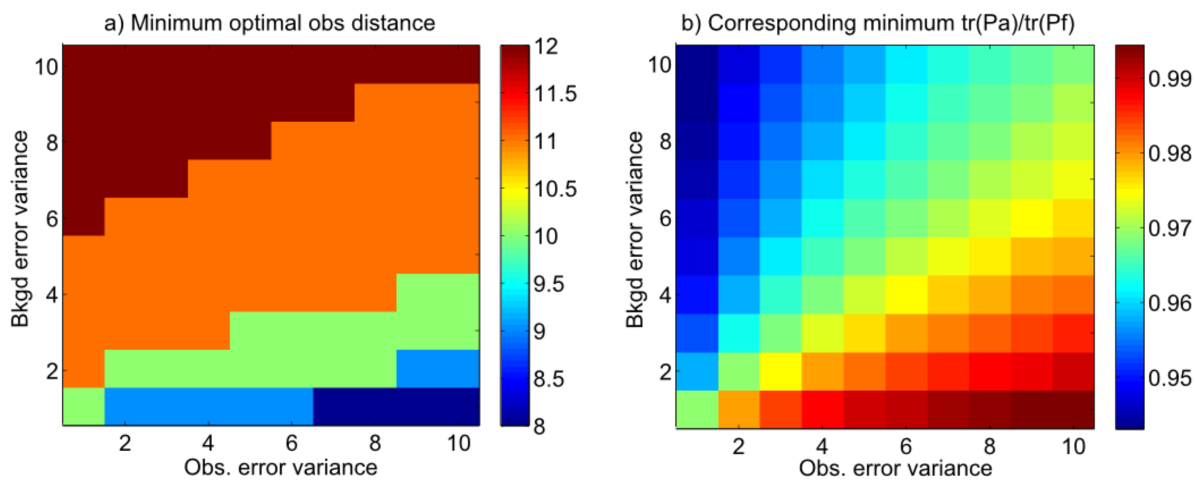

Fig. 2.7 a) The minimum optimal observation distance as a function of the error variances of background and observation. b) The ratio of $tr(\mathbf{P}^a)$ to $tr(\mathbf{P}^f)$ when the minimum optimal observation distance is reached.

b. The number of observations.

A larger quantity of observations usually means more information, and is expected to more significantly reduce analysis uncertainty. A similar Kalman Filter exercise is performed so as to test the impact of observation number on total analysis error variance. In this experiment, the error variance for both background and observation is 1; and the error decorrelation distance is 5 grid points. Given the fixed error statistics, the number of equally distributed observations varies in this exercise.

As shown in Fig. 2.8a, assimilating a larger number of observations has more impact on the state vector as expected (comparison between 8 observations and 16 observations assimilations). When the observation error covariance matrix is well known, assimilating more observations leads to smaller total analysis error variance $tr(\mathbf{P}^a)$, as shown in Fig. 2.8b (black curve).

In real data assimilation systems, observation errors are sometimes assumed to be uncorrelated in space because of the limited computer power and limited knowledge of the error correlation (Houtekamer and Mitchell 2000; Anderson et al. 2009). Accordingly, the off-diagonal elements in observation error covariance matrix **R** could be falsely ignored. According to Dalay (1991, Eq. 4.9.4) and Eqs. (2.10) – (2.12), the analysis covariance matrix resulted from the impact of misrepresenting **R** can be estimated by:

$$\begin{aligned}\mathbf{P}^a &= \mathbf{P}^f - 2\mathbf{P}^f\mathbf{H}^T(\mathbf{H}\mathbf{P}^f\mathbf{H}^T+\mathbf{R}^e)^{-1}\mathbf{H}\mathbf{P}^f \\ &\quad + \mathbf{P}^f\mathbf{H}^T(\mathbf{H}\mathbf{P}^f\mathbf{H}^T+\mathbf{R}^e)^{-1}(\mathbf{H}\mathbf{P}^f\mathbf{H}^T+\mathbf{R})(\mathbf{H}\mathbf{P}^f\mathbf{H}^T+\mathbf{R}^e)^{-1}\mathbf{H}\mathbf{P}^f\end{aligned} \tag{2.14}$$

where $\mathbf{R}^e$ is diagonal, and is the *estimated* observation error covariance matrix which could be different from the real **R**; other notations are the same as in Eqs. (2.10) – (2.12). If **R** is well represented ($\mathbf{R}=\mathbf{R}^e$), Eq. (2.14) is equivalent to Eq. (2.12).

From Eq. (2.14), $tr(\mathbf{P}^a)$ can be calculated and plotted in Fig. 2.8b (the green curve). This figure shows that the optimal observation number in this experiment is 20 as it leads to the minimum $tr(\mathbf{P}^a)$. On the one hand, assimilating fewer observations reduces the amount of information, and consequently results in larger analysis uncertainty. On the other hand, when more observations are assimilated, their errors are better correlated in space, which increases the difference between **R** and diagonal $\mathbf{R}^e$ in terms of their off-diagonal elements. This experiment suggests that assimilating more observations is not always beneficial to the data assimilation system, when the observation errors statistics are not precisely provided.

Furthermore, the optimal observation number can be a function of the decorrelation distances of observation and background, while the estimated observation error covariance matrix $\mathbf{R}^e$ is always set to be diagonal. Figure 2.9a shows that when observation error decorrelation distance is larger, the optimal observation number is smaller, because assimilating fewer observations can decrease the observation error correlation and thus reduce the difference between **R** and $\mathbf{R}^e$. Furthermore, when the background error has a longer decorrelation distance in space, fewer observations are needed, since they can update many state variables through background error correlation.

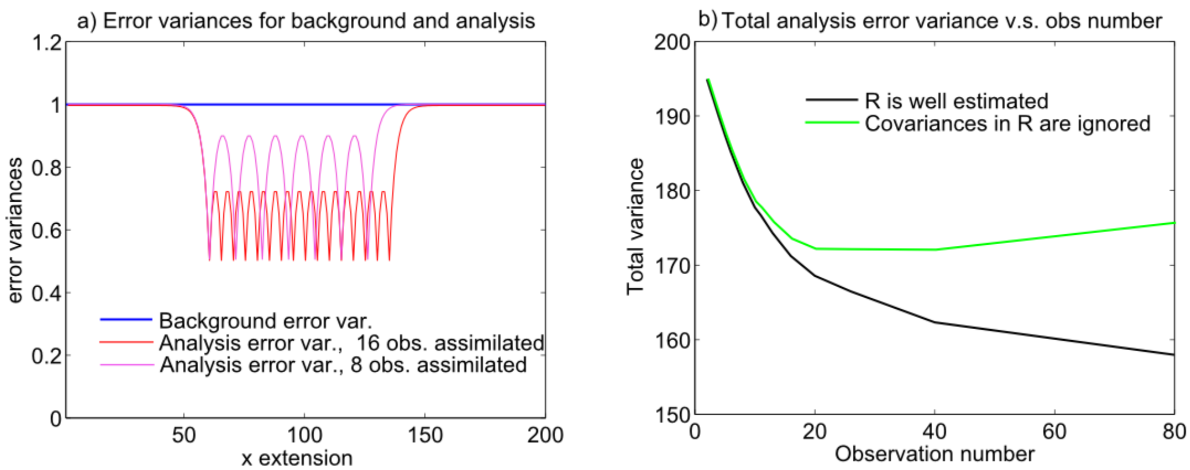

Fig. 2.8 a) background error variances and analysis error variances when 8 observation are assimilated, and when 16 observations are assimilated. b) Total analysis error variances $tr(\mathbf{P}^a)$ against observation number when observation error covariance matrix **R** is well estimated, and when the off-diagonal elements in **R** are ignored.

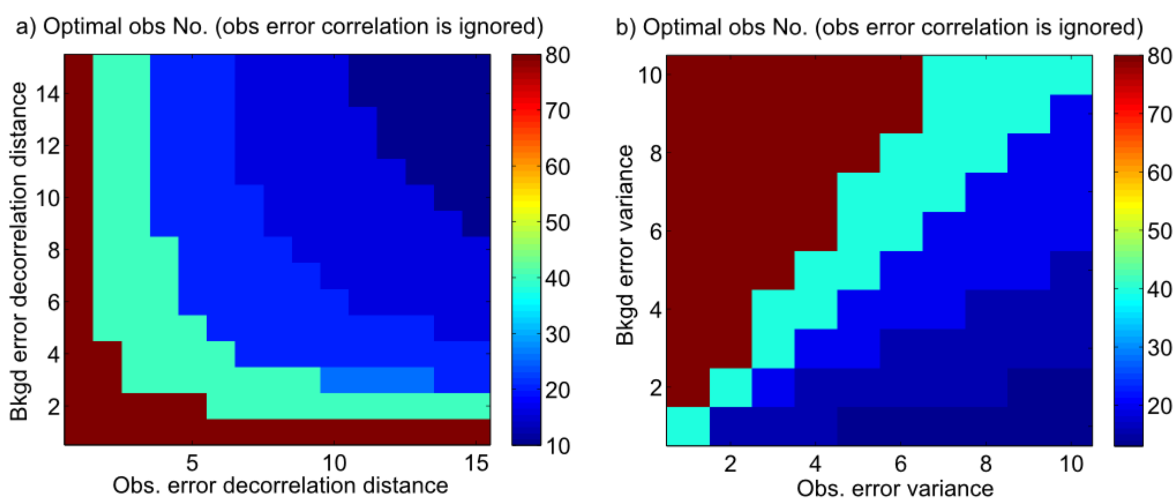

Fig. 2.9 a) Optimal observation number as a function of error decorrelation distances of background and observation, when covariances of observation error are ignored. b) Optimal observation number as a function of error variances of forecast and observation, when covariances of observation error are ignored.

The variances of background and observation errors can also affect the optimal observation number when observation error covariances are ignored. Figure 2.9b shows that fewer observations are needed when the observation error variance is larger. This is because larger observation error variances amplify the covariances which are the off-diagonal elements in the **R** matrix. Thus fewer observations are required in order to reduce error correlation. While background error variance is smaller, fewer observations are required, as reducing background error is equivalent to increasing observation error.

c. Comparison between the impacts of observation number and observation accuracy.

The phased-array technique allows radar to adaptively control observation number and observation accuracy. On the one hand, if radar receives more independent echoes from the same location, data can be more accurate (over sampling). On the other hand, if more beam positions are placed in a certain area, a larger number of observations can be acquired. Within a certain time period, the user of such radar has to choose between higher data accuracy and larger observation number. Therefore, an inspection of the influence of observation accuracy and observation number on data analysis assists in deciding observation strategy.

The data assimilation system in this study uses a 11 by 11 two dimensional field as the background (Fig. 2.10), the errors of which have a variance of 4 and are uncorrelated in space. Observations are uniformly distributed in this two-dimensional field. The observation errors are modeled by two parts: measurement error without error correlation in space; and representative error with strong spatial correlation. Both errors follow Gaussian distribution and are independent to each other. Therefore the observation error structure can be modeled by equations

$$\mathrm{var}(\varepsilon_o) = \frac{\sigma_m^2}{L} + \sigma_R^2 \tag{2.15}$$

$$\mathrm{cov}(\varepsilon_{o,i}, \varepsilon_{o,j}) = \sigma_R^2 \exp\left(-\frac{d_{i,j}^2}{r^2} \right) (i \neq j) \tag{2.16}$$

where ε_o is the observation error; L represents the number of independent echoes for each observation; σ_m^2 / L is the measurement error variance, which is the error variance of the mean of independent echoes collected for one radar observation. σ_R^2 is the representative error variance; $\varepsilon_{o,i}$ and $\varepsilon_{o,j}$ are the errors of observations i and j; $d_{i,j}$ is the distance between two observations; r is observation error decorrelation distance. This observation error structure will be used to generate the observation error covariance matrix **R** for the data analysis system. Given the error statistics, the analysis error covariance $\mathbf{P}^a$ can be computed from the linear Kalman filter equations (2.10) – (2.12). Similar to the previous exercises, total analysis error variance $tr(\mathbf{P}^a)$ is considered to be the indicator of analysis uncertainty. While L decides the measurement accuracy of the diagonal of **R**, it does not affect the off-diagonal elements of **R**. If more observations are collected, the data will have higher spatial resolution, which affects the off-diagonal elements of **R** and the observation operator **H**.

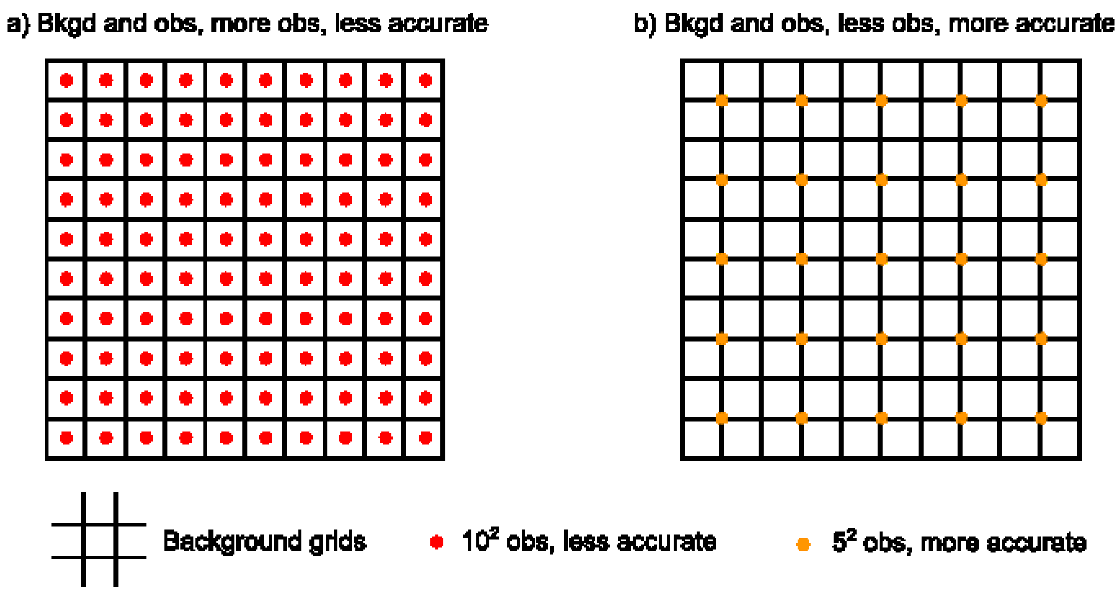

Fig. 2.10 Example of background grids and observations. a) 10^2 observations are available, but less accurate. b) 5^2 observations are available, but more accurate.

In order to describe the trade-off between observation number and observation accuracy, the 'equivalent radar resource' can be used, and is defined as the product of the number of independent echo on each observation and total observation number. For example, as shown in

Fig. 2.10, if the total observation number is 10^2, and 4 echoes are averaged for each observation, then the 'equivalent radar resource' is $10^2 \times 4$. The same radar resource can also be used to obtain 5^2 observations, each of which has 16 independent echoes.

Figure 2.11 shows $tr(\mathbf{P}^a)$ as a function of the 'equivalent radar resource' for five observation strategies. Each observation strategy corresponds to a choice of observation number and the independent echo number L. Among the five observation strategies shown in both Fig. 2.11a and b, one of the best ways to use radar resource is to maintain the observation uncertainty (averaging 4 echoes for each observation), and increase the observation number. The blue and green curves in Fig. 2.11a indicate that as long as more than 21^2 observations are maintained, increasing data accuracy, via averaging more independent echoes, and adding more observations have the same impact upon the analysis. If less than 21^2 observations are available, even though they are more precise (e.g. the cyan and red curves in Fig. 2.11a), the analysis uncertainty is larger, as compared to other strategies.

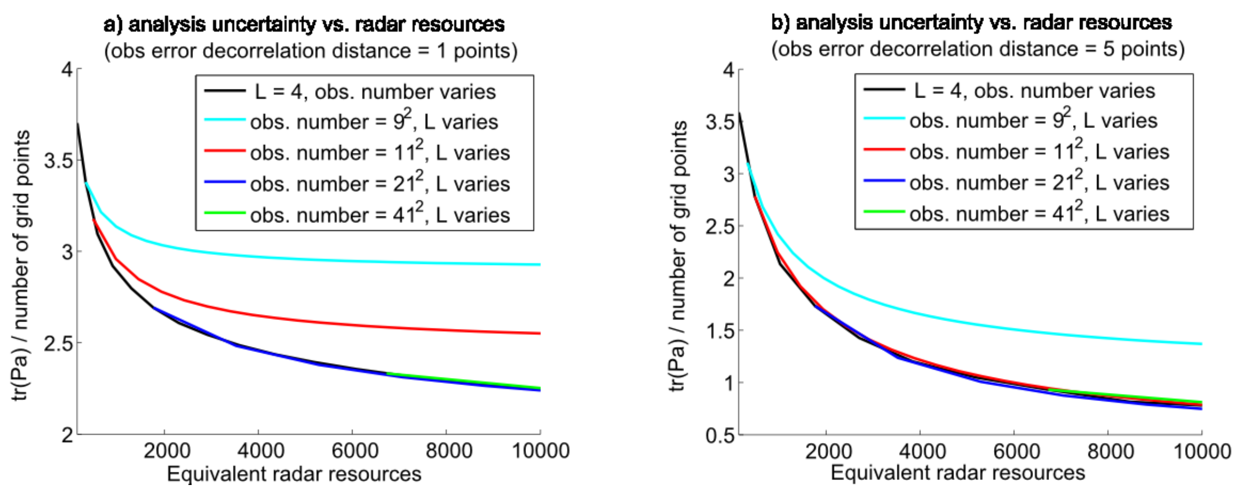

Fig. 2.11 The ratio of total analysis error variance $tr(\mathbf{P}^a)$ to the number of grid points, as a function of the equivalent radar resource, for five different observation strategies. Experiments are conducted when observation error decorrelation distance is set to 1 (a), and when observation error decorrelation distance is set to 5 (b).

Observation error structure has an impact on the choice of optimal observation strategy. Figure 2.11b shows that if the representative error decorrelation distance increases from 1 to 5, only 11^2 observations are required for reaching the optimal analysis. This is because, when observation errors are better correlated in space, they provide more mutual information; therefore fewer observations are needed.

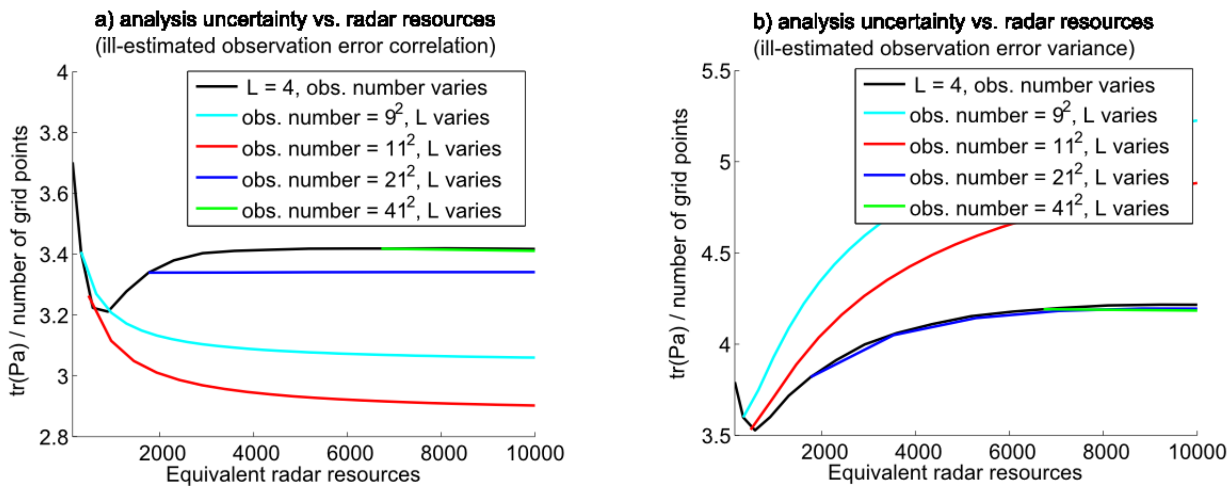

Fig. 2.12 The ratio of total analysis error variance $tr(\mathbf{P}^a)$ to the number of grid points, as a function of the equivalent radar resource, for five different observation strategies. The experiments are conducted when the representative error decorrelation distance is underestimated (a) and when the measurement error standard deviation is underestimated (b).

In contrast to the above experiment where the error statistics are well estimated, the next experiment assumes that the observation errors are poorly estimated, and uses Eq. (2.14) to estimate analysis uncertainty. Figures 2.12a and 2.12b are plotted under the conditions that the representative error decorrelation distance is underestimated by a factor of 0.3, and the measurement error standard deviation is underestimated by a factor of 0.3, respectively. Figure 2.12a shows that the 'optimal' strategy among the five choices is to keep 11^2 observations (red curve). This is because fewer observations provide less information; but more observations increases the difference between the real and estimated observation error covariance matrices, as discussed in the previous subsection (see Fig. 2.8b). Figure 2.12b suggests the existence of an 'optimal' radar resource under the condition that observation error variance is poorly estimated. If more radar resources are available than this optimal number, analysis uncertainty increases. This is because an increase in observation number (the black curve in Fig. 2.12b) adds more data with inaccurate estimation of their errors to the system, thus leading to a worse analysis result. When observations become more accurate (the coloured curves in Fig. 2.12b), they play a more important role in the assimilation system. Therefore the misrepresentation of their uncertainties strongly influences the analysis error.

2.5 Summary

Several idealized experiments of the Ensemble Kalman Filter (EnKF) and the linear Kalman Filter are performed to examine the influence of uncertainties in EnKF and the effectiveness of observations on data analysis. The uncertainties examined in this chapter includes forecast uncertainty with respect to the ensemble mean, error estimation of the first guess, model error, and the estimation of model and observation errors. The observation information inspected in this study includes observation spacing, observation number, and observation accuracy.

The experiments on forecast error estimation show that the difference between the ensemble mean forecast and the truth plays an important role in underestimating error statistics. The underestimation of forecast error results in larger analysis error. However, this problem diminishes when the ensemble mean moves closer to the truth after a few cycles.

If the initial uncertainty of the first guess is underestimated, the filter needs a much longer time to converge, and may affect the final assimilation result. On the other hand, if it is overestimated, the problem it causes is evident only in the first a few cycles. Therefore underestimating the initial error is more problematic than overestimating it. However, this conclusion is drawn based on the assumption that all the assumptions of EnKF are perfectly fulfilled. In a real data assimilation system, more complexities, such as the overwhelming model error, the data quality and the availability of observations, may weaken this conclusion.

After model error is taken into consideration, analysis error converges to a higher value, even though it is well estimated. If model and observation errors are poorly estimated, the analysis uncertainty is even larger, especially after the cycling process.

Single-step analysis is applied for examining the influence of observation information on analysis. When two observations are available, leaving them far apart is beneficial for the data analysis in terms of reducing total analysis error variance. When the background error decorrelation distance or the observation error decorrelation distance is larger, the distance between two observations should also be larger.

When the observation error statistics are well known, assimilating more observations is always helpful for reducing analysis uncertainty. However, if the observation error covariance is falsely ignored, data thinning should be performed.

The trade-off between observation accuracy and observation number is also considered. The experiments prove that a threshold of observation number exists, beyond which increasing the observation number and reducing the observation error can improve analysis to the same degree. If the threshold cannot be reached, adding more observations is more helpful than enhancing data quality. When the observation error statistics are misrepresented, thinning is usually required for reducing analysis error.

There are many limitations in this study. First, a simple model with one control variable is used in all the experiments, which excludes any cross-correlation between control variables, and ignores the model bias. Secondly, the ensemble members are sufficient for the simple experiments, due to the small model extensions. In a real data assimilation system where there are more model grids and control variables, limited ensemble members usually introduce more uncertainties into the system. Thirdly, the ensemble mean in section 3 is close to the truth, which does not require a large ensemble spread. Therefore, the ensemble members are able to represent the system errors quite well at the beginning of EnKF. In reality, because the difference between the ensemble mean and the truth is large, and the ensemble spread is large, it is more difficult to represent the errors statistics by a limited number of members. Lastly, uniform background fields in linear systems are used to assimilate observations with simple error structure in section 4, which is far from reality. In a real data assimilation system, deciding an observation strategy is more complicated than in section 4.

Chapter 3

Examination of Situation-Dependent Background Error Covariances at the Convective Scale in the Context of the Ensemble Kalman Filter

The previous chapter discussed the uncertainties that cannot be estimated by ensemble members in Ensemble Kalman Filter (EnKF). As a further step of understanding the uncertainties involved in EnKF, this chapter examines the background error statistics represented by ensemble members yielded from a complex numerical weather prediction model.

The background fields are model outputs with a 1-km resolution in space and 5-min temporal interval, which are suitable for high resolution radar data assimilation. The spatial pattern and time evolution of the background error under different weather situations are studied. The results from this chapter will be used for implementing a high resolution EnKF system as described in the next chapter.

This chapter is based on the following journal article.

Chung, Kao-Shen, Weiguang Chang, Luc Fillion, Monique Tanguay, 2013: Examination of Situation-Dependent Background Error Covariances at the Convective Scale in the Context of the Ensemble Kalman Filter. Mon. Wea. Rev., 141, 3369–3387.

The author of this thesis designed most of the high resolution EnKF system described in this chapter, generated the initial perturbations for ensemble forecasts and inspected the time evolution of horizontal spatial correlation and standard deviations of the background errors. The author of this thesis also helped to analyze the results of this study.

Chapter 3

Examination of Situation-Dependent Background Error Covariances at the Convective Scale in the Context of the Ensemble Kalman Filter

Abstract

A High Resolution Ensemble Kalman Filter (HREnKF) system at convective-scale has been developed based on the Canadian Meteorological Center's operational global Ensemble Kalman Filter (EnKF) system. This study focuses on the very early stage of transition from purely homogeneous isotropic background-error correlations to situation-dependent correlations. It has been found that forecast error structures can develop situation-dependent features in as little as 15 minutes. Furthermore, the dynamic and thermodynamic variables require different periods of time to build up their own forecast error structures. Differences in these structures between regions with and without precipitation are also investigated. An examination of temperature tendencies revealed that microphysical processes are as important as dynamical forcing in determining the structure of convective-scale errors structures, and that once physical processes become active, these structures change rapidly before the onset of precipitation. This study is intended to be the basis for a systematic exploration in the near future of the usefulness of the HREnKF system in assimilating high-density observations such as radar data.

3.1 Introduction

One important goal of the ensemble approach in atmospheric data assimilation is to approximate moments of the Probability Distribution Functions (PDFs) of the analyses and forecasts using a group of random realizations. The Ensemble Kalman Filter (EnKF) is an objective way to obtain a set of analyses and also initialize ensemble forecasts. Furthermore, an advantage of using the EnKF algorithm is that it estimates and updates the background error covariances with a short-term ensemble forecast in each cycle, thus taking into account situation-dependent features.

EnKF algorithms have been developed for a wide range of spatial scales. Designed for large scales, Houtekamer and Mitchell (2005) implemented an EnKF system at the Canadian Meteorological Center (CMC) to assimilate observations with the Global Environmental Multiscale (GEM) model. This EnKF system provides an ensemble of initial conditions for the CMC's medium-range ensemble prediction system. Their study demonstrated that the EnKF can be used successfully for operational atmospheric data assimilation. Szunyogh et al. (2008) employed the Local Ensemble Transform Kalman Filter (LETKF) algorithm with the National Centers for Environmental Prediction (NCEP) global model. They found that the LETKF provides more accurate analyses than the Spectral Statistical Interpolation (SSI) analyses in sparse observation regions. Based on the Weather Research and Forecasting model (WRF), a limited area EnKF system has been used with conventional data by Torn and Hakim (2008). In that study, it was found that upper-tropospheric wind and mid-tropospheric temperature are correlated with the water vapor field, which suggests that assimilating cloud motion wind and aircraft temperature observations may have a significant impact on the moisture analysis. The Italian National Meteorological Service also applied the LETKF in regional numerical weather prediction (NWP) (Bonavita et al. 2010). The results showed that the LETKF-based forecasts generally outperformed their operational 3D-VAR-based (constant background error covariances) counterparts according to a root-mean-square error verification metric. The application of the EnKF technique at the storm scale is relatively new and the research is focused on the accuracy of EnKF analyses. Using simulated Doppler winds, Snyder and Zhang (2003) first applied the EnKF algorithm coupled with a cloud-resolving model. The results demonstrated the potential of the EnKF at convective scales. Tong and Xue (2005) examined the impact of assimilating both

Doppler and reflectivity data in a series of Observation System Simulation Experiments (OSSEs). They concluded that the best results are obtained when both Doppler wind and reflectivity data are used. Dowell et al. (2004, 2011) tested the EnKF algorithm with real radar data. All the above studies showed that by assimilating Doppler winds and/or reflectivity, realistic storm-scale structures can be obtained in the analyses. Recently, several investigations have turned to very short-term forecasts and to specific weather phenomena (Zhang et al. 2009, Stensrud and Gao 2010, Aksoy et al. 2010). Forecast error covariances play a crucial role in data assimilation algorithm. However, their structure at convective scales is not well understood. Some studies (Bannister et al. 2011; Montmerle and Berre 2010) have shown that instead of using climatological synoptic-scale statistics, it is preferable to construct situation-dependent background error statistics. In the 3D-Var framework, Brousseau et al. (2012) examined the impact of using situation-dependent background error covariances (provided by a six-member ensemble) at convective scales. They showed the impact on analysis increments and found improvements in short-term forecasts.

In this study, a High Resolution Ensemble Kalman Filter (HREnKF) system has been adapted for the limited area model GEM_LAM from the global EnKF system (Houtekamer and Mitchell 2005; Houtekamer et al. 2009) currently operational at the CMC. The goal for the near future is to develop a convective-scale data assimilation system which assimilates radar data. Before discussing systematic assimilation of real radar observations, this paper presents an examination of the transition from homogeneous isotropic forecast error to situation-dependent short-term forecast error covariances at cloud-resolving scales. Many studies have shown the advantages of propagating the information of flow-dependent forecast errors via cycling procedures in EnKF systems. However, forecast errors at the convective scale are not well understood. Investigating the complex structure of forecast errors at cloud-resolving scales also helps to provide optimal values for various parameters (for instance, localization length) in the EnKF system. The paper is structured as follows. In section 2, the HREnKF system is introduced, while the configuration of the limited area model and the method used to specify the initial perturbation in the HREnKF are presented in section 3. Section 4 describes a case study and the performance of the deterministic forecast. The results of background error covariances at the mesoscale / convective scale are presented in section 5. The summary and some suggestions for future work are given in section 6.

3.2 The High Resolution EnKF (HREnKF) system

There are currently two ways of generating the ensemble analyses in the context of the EnKF: 1) Houtekamer and Mitchell (2001) applied a Monte Carlo approach where observations are perturbed in order to estimate the uncertainties in the analysis; 2) without perturbing the observations, a deterministic method is used to transform an ensemble of background fields into an ensemble of analyses (Whitaker and Hamill 2002; Bishop et al. 2001 and Anderson 2001). We follow the first approach. The HREnKF system is a modified form of the Canadian EnKF system (Houtekamer et al. 2009) adapted for limited area data assimilation and forecasting. Here we point out the basic features common to the global and LAM EnKF configurations. The analysis and forecast steps constitute the basic parts of the algorithm of the EnKF. The analysis step updates the atmospheric state based on the most recent observations. The central equation of the EnKF can be written as:

$$\boldsymbol{x}^a = \boldsymbol{x}^f + \boldsymbol{K}(\boldsymbol{y} - \boldsymbol{H}\boldsymbol{x}^f) \tag{3.1}$$

where $\mathbf{x}^a$ is the analysis (or posterior estimate), $\mathbf{x}^f$ represents the first guess (or prior estimate), $\boldsymbol{y}$ is a set of perturbed observations ($\boldsymbol{y} = \boldsymbol{y}^o + \varepsilon^o$, where $\mathbf{y}^0$ is the observations and ε^o represents the observation errors), $\boldsymbol{H}$ is the forward operator which maps the background fields onto the observation space, and $\boldsymbol{y} - \boldsymbol{H}\boldsymbol{x}^f$ is called the innovation. $\boldsymbol{K}$ is the so-called "Kalman gain matrix" defined as:

$$\boldsymbol{K} = \boldsymbol{P}^f \boldsymbol{H}^{\mathrm{T}} (\boldsymbol{H}\boldsymbol{P}^f \boldsymbol{H}^{\mathrm{T}} + \boldsymbol{R})^{-1} \tag{3.2}$$

where $\boldsymbol{P}^f$ and $\boldsymbol{R}$ represent the background and observational error covariance matrices, respectively. The situation-dependent matrix ($\boldsymbol{P}^f$) is updated (forecasted) from the previous analysis time t_n to the new analysis time t_{n+1} through a set of ensemble members.

The HREnKF assimilation system has the following features:

a. Sequential processing of batches of observations

In operational atmospheric data assimilation systems, the typical size of the observation vector is at least $O(10^6)$ or even more (Houtekamer and Mitchell, 2009). To deal with issues of storage and inversion of matrices, the observations are divided into batches that are assimilated sequentially. In comparison with assimilating all observations simultaneously, one should notice that, the batching process of observations is strictly valid as long as the observations whose observation errors are correlated with each other are processed in the same batch (Houtekamer and Mitchell, 2001).

b. Partitioning the ensemble

In the EnKF algorithm, the same set of prior fields could be used both, to provide initial guesses and also to compute the Kalman gain. This double use of the same information may lead to an under-estimation of the spread in the ensemble (Houtekamer and Mitchell, 2001). In the current system, the ensemble is partitioned into four sub-ensembles, and the gain matrix used for each sub-ensemble is computed by using the prior fields from the other sub-ensembles, thus improving the correspondence between ensemble spread and the ensemble mean error. The disadvantage of such a scheme is that the estimates of covariance are noisier, due to the smaller size of the sub-ensembles.

c. Localization

Due to the limited number of ensemble members, the estimated correlations can be noisy. To deal with this sampling error, a localization procedure is applied to both the horizontal and vertical background error covariances. The localized Kalman gain can be defined as:

$$\boldsymbol{K} = [(\rho_V \circ \rho_H \circ \boldsymbol{P^f})\boldsymbol{H}^T)][\boldsymbol{H}(\rho_V \circ \rho_H \circ \boldsymbol{P^f})\boldsymbol{H}^T) + \boldsymbol{R}]^{-1} \tag{3.3}$$

where ρ_H and ρ_V are the correlation functions applied for horizontal and vertical localization, and $\circ$ denotes the Schur product. Following Houtekamer and Mitchell (2001), when ρ_H and ρ_V are functions of distance only, the order of the observation operator and the Schur product can be interchanged. Therefore, the Kalman gain with model-space localization, as in eq. (3.3), can be approximated by the Kalman gain as:

$$\boldsymbol{K} = [\rho_V \circ \rho_H \circ (\boldsymbol{P^f H}^T)][\rho_V \circ \rho_H \circ (\boldsymbol{HP^f H}^T) + \boldsymbol{R}]^{-1} \tag{3.4}$$

d. Simulation of model errors

It is important to take into account the model error properly since neglecting model error may lead to a very small ensemble spread, and this may cause a convergence problem of the filter. Unfortunately, the model error in NWP, especially at the convective scale, is not well understood. In a similar way as Houtekamer (2009), the model error component of the HREnKF applies a simplified and reduced amplitude form of homogeneous and isotropic background error correlations. This is done by adding an ensemble of random perturbation fields with a specified covariance structure to the ensemble of background fields.

The HREnKF system consists of a set of parallel short-term forecast and data assimilation steps. Figure 3.1 illustrates the cycling procedure between analysis and forecast steps. In our study, the first initial guess is from a previous, unperturbed (deterministic) forecast. By adding prescribed random perturbations (based on the aforementioned procedure for dealing with model error) to the deterministic forecast, an initial set of ensemble members is obtained. The random errors are added to simulate errors of the numerical model. To take into account the uncertainty in observations, these are also perturbed according to their estimated errors. Via the data assimilation process (analysis step), one is able to update the analyses and launch the model (forecast step) to produce very short-term forecasts. The analysis and forecast steps are repeated (dashed line) in the system as the cycling proceeds.

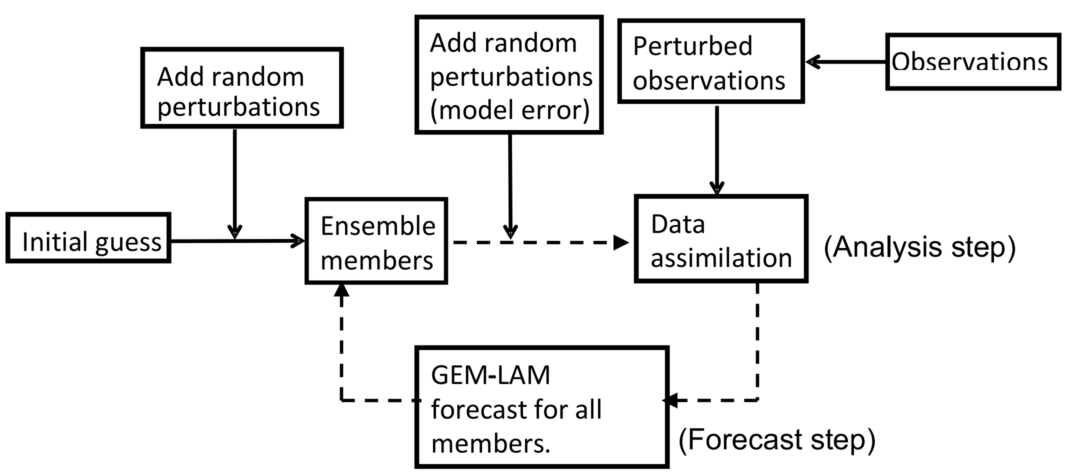

Fig. 3.1 Flow chart of the cycling procedure in the HREnKF system.

3.3 Configuration of the experiment

a. limited area model

The fully compressible limited area model GEM_LAM is used in our study. The model employs an implicit scheme in time and a semi-Lagrangian scheme in space. Detailed descriptions of the GEM model dynamics and physics formulations are available in Côté et al. (1998) and Mailhot et al. (1998), respectively.

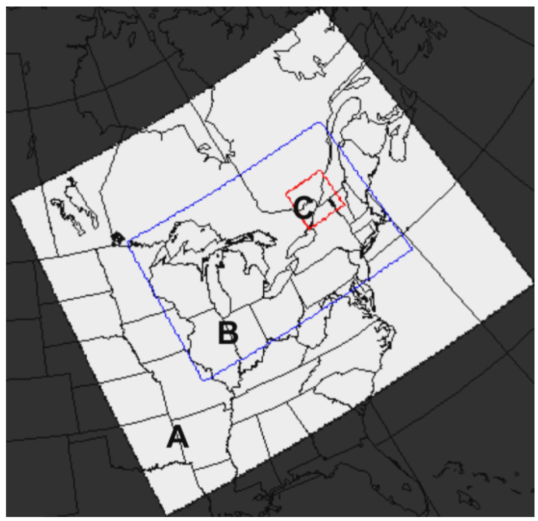

Fig. 3.2 Extent of limited-area model domains for the nested system. Domain A, B (blue box) and C (red box) correspond to LAM-15km, LAM-2.5km and LAM-1km, respectively.

A three-level nested domain (Fig. 3.2) is used in the model configuration to obtain a deterministic forecast in our experiments. The global grid forecast was run using GEM at a 15-km resolution (hereafter GLB-15km). The GLB-15km, which used the Sundqvist condensation scheme (Sundqvist 1978), was performed from 1200 UTC 21 July to 0300 UTC 22 July 2010. These hourly forecasts were used as initial conditions (1200UTC) and lateral boundary conditions to launch a limited area model in domain A with a horizontal resolution of 15-km (hereafter LAM-15km). The Milbrandt and Yau (2005) double-moment microphysics scheme used in LAM-15km predicts the mass mixing ratio and total number concentration of six hydrometeor categories (cloud water, rain, ice, now, graupel, and hail). This approach leads to more precise than the Sundqvist condensation scheme for the computation of microphysical growth/decay rates and precipitation, and it is expected to shorten the spin-up phase. A second nested LAM (domain B) of a forecast is started 6 h later (1800UTC) with a 2.5-km resolution (LAM-2.5km) of the model. This domain (564 x 494 grid points) covers the southern part of the provinces of Ontario and Québec. A 1-km resolution simulation (domain C, LAM-1km) is launched 6 h later at 0000 UTC July 22 2010, with an integration time step of 30s. The LAM-1km is centered on the Montréal region (300 x 300 grid points) for the purpose of eventually assimilating S-band radar data provided by McGill University.

The limited area simulations are fully non-hydrostatic with 58 hybrid vertical levels and a lid at 10 hPa. The land surface scheme called "Interaction between Surface, Biosphere and Atmosphere" (ISBA; see Noilhan and Planton 1989) is applied. The Kain-Fritsch convective scheme (Kain and Fritsch 1990) is applied in LAM-15km, however no convective parameterization is used in either LAM-2.5km or LAM-1km. In addition, in contrast to the global EnKF system which uses multi-model option (different versions of physical parameterizations), currently we keep fixed all the physical schemes for running the ensemble forecasts. We point out that this configuration may cause an underestimation of the error covariances. The double-moment version of the Milbrandt and Yau (2005) microphysics scheme is used for the grid-scale processes. Note that besides the standard model control variables: horizontal wind (u, v), temperature (T), and specific humidity (HU), the mixing ratio and number concentration of six hydrometeor variables (cloud water, rain, snow, ice, graupel and hail) are also carried from the driving conditions.

b. method of adding initial perturbations for ensemble members

It is feasible to obtain a set of ensemble initial states from the global EnKF system. However, as mentioned previously, in this study the initial states are constructed by generating random perturbations and adding them to a deterministic forecast. By providing homogeneous and isotropic perturbations to obtain initial states, one is able to examine the transition to situation-dependent forecast error covariance structures. In addition, the evolution of situation-dependent error structures in different locations can be fairly compared.

The HREnKF includes a background-error covariance simulator which produces random perturbations, from which we sample different fields for different members of the ensemble. The random perturbations are generated from the bi-Fourier decomposition in the spectral domain (Fillion et. al. 2010). The error simulator considers independent perturbations for streamfunction, divergence, temperature, humidity, and surface pressure, which are then transformed into wind, temperature, specific humidity and surface pressure background errors. The initial perturbations of background errors in the HREnKF system are generated as horizontally homogenous and isotropic in the limited area domain. We stress here that no well-tuned mesoscale (or convective-scale) data assimilation system is available to us at this stage of our study, which could serve as a guide. Contrary to the global EnKF, we do not have at hand reliable operational non-separable spectral homogeneous and isotropic correlation statistics. We thus used a simple specification of correlation scales in the horizontal and vertical using the separability assumption for background error correlations. This error specification is obviously an approximation. Nevertheless, we show clearly in the following that a rapid transition to situation-dependent structures occurs. The standard deviation background errors for the control variables are: 3 ms^{-1} for horizontal wind, 0.5 degree for temperature, and 0.1 for the logarithm of specific humidity. Those statistics were obtained from a 2.5-km National Meteorology Center (NMC, currently known as NCEP) approach (e.g. Fillion et al. 2010). We imposed a 10-km horizontal correlation length for stream function, velocity potential, temperature and logarithm of specific humidity, and a correlation length of 200 hPa in the vertical. No cross-correlations are imposed between different variables. In addition, we note that in general, it is important to consider perturbations of lateral boundary conditions (Caron 2012). However, for the first step of implementing the Canadian HREnKF system, we only added the errors to the fields over the entire analysis domain and did not perturb the lateral boundary conditions.

3.4 Description of the case study

The period selected for the case study was 21-22 July 2010. During this period, a mesoscale cyclone developed near the border between the provinces of Québec and Ontario, and subsequently moved eastward over Québec around 1300 UTC 21 July 2010. Precipitation was observed over the Montréal region from 1800 UTC 21 July to 0600 UTC 22 July. A deterministic model simulation was produced as the control run, and compared to remote sensing observations to assess the performance of the forecast.

a) b)

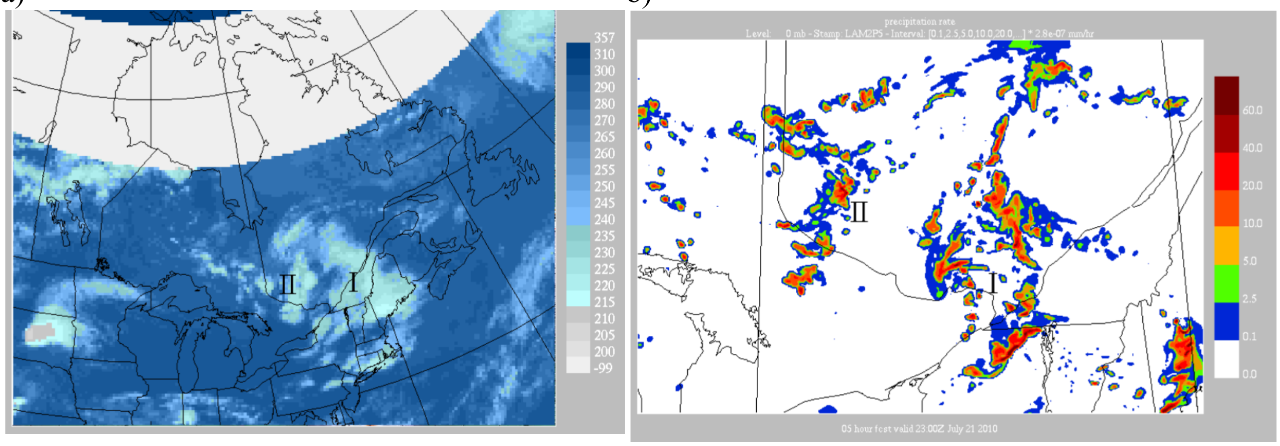

Fig. 3.3 a) Brightness temperature [K] from the 11 micron channel of GOES observations at 2245 UTC 21 July 2010; b) Precipitation rate [mm hr^{-1}] from the LAM-2.5km forecast at 2300 UTC 21 July 2010.

Figure 3.3a shows the brightness temperature from the 11 micron channel of Geostationary Operational Environment Satellite (GOES) data around 2300 UTC 21 July, and Fig. 3.3b shows the model 5-h simulation (2300 UTC) of surface precipitation at 2.5-km resolution. The similarity in the pattern of weather systems (I and II) between observations and simulation indicates that the driving model provides reasonable initial and lateral boundary conditions in this case. The CMC radar composite over southern Québec is shown in Fig. 3.4a. The precipitation rate of the 1-km resolution forecast at 0030 UTC 22 July 2010 is depicted in Fig. 3.4b. In the surface analysis at 0000 UTC in Fig. 3.4c, a low pressure system and two fronts are close to the LAM-lkm domain. Clouds (IR satellite observations in Fig.3.4c) and precipitations (ground-based radar observations in Fig. 3.4a) were produced accordingly. At a lead time of 30-min, the LAM-1km forecast predicted precipitation over the Montréal region. Two well-structured weather systems are simulated in the analysis domain: one in the north and another in the south-east of the domain. In addition, some convective cells are scattered in the center and south of the domain. Compared to radar observations, the LAM-1km is able to simulate the precipitation over the Montréal domain, but with different structures and locations. By examining the time sequence of radar composites over southern Québec, we found that a phase error seems to occur. One should note that this is not an uncommon issue at mesoscale and convective scales.

a) b) c)

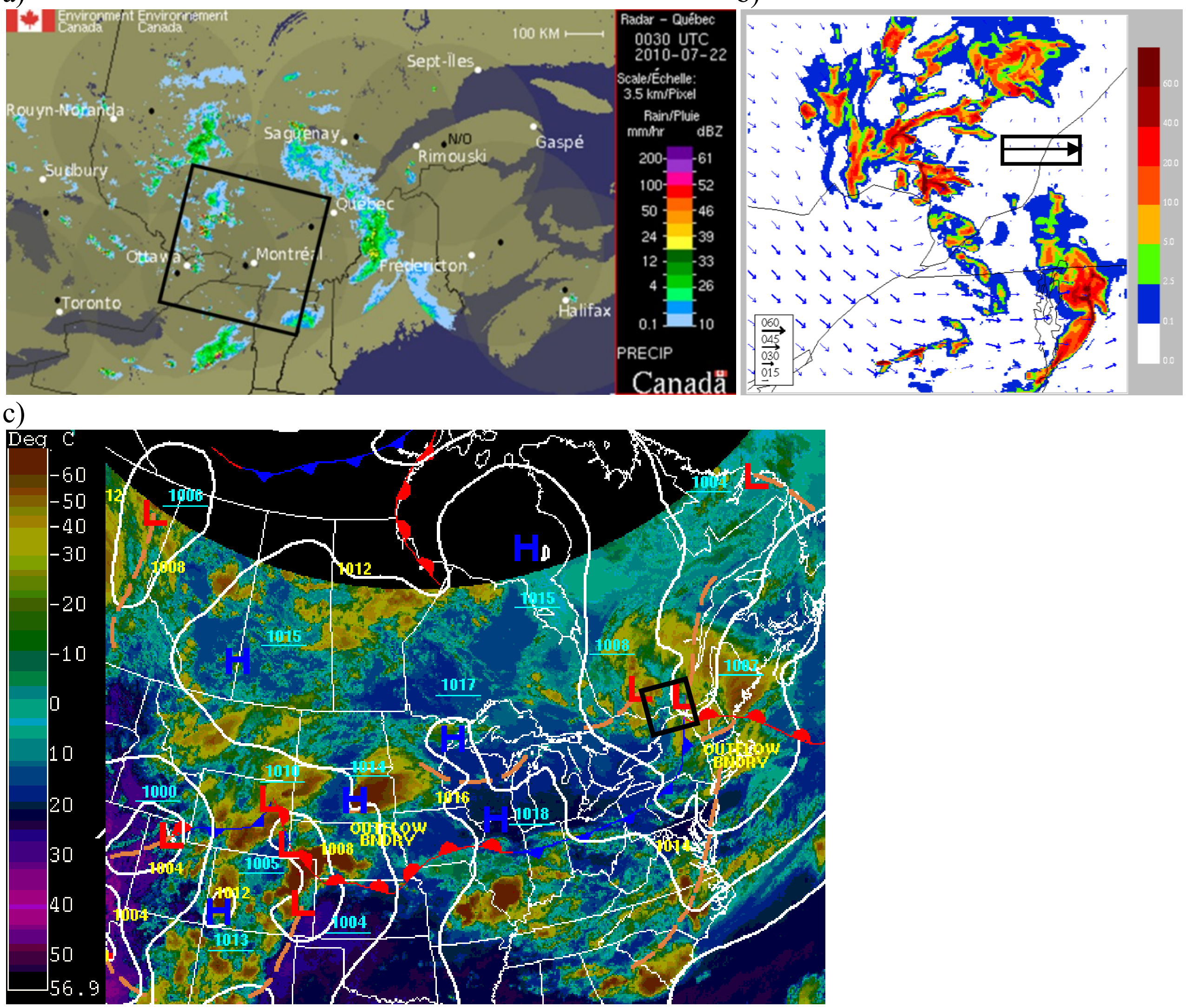

Fig. 3.4 a) Radar reflectivity [dBz] composite over southern Québec at 0030 UTC July 22 2010. The black square indicates the analysis domain of the LAM-1km; b) surface precipitation rate [mm hr^{-1}] and horizontal wind vectors [knots] at 800 hPa from the LAM-1km forecast at 0030 UTC 22 July 2010. The rectangular box is within no-precipitation areas and arrow line is the location of cross-section for further examination in section 3.5; c) synoptic scale surface analysis and IR composite of North America produced by NOAA at 0000 UTC July 22 2010. The black square indicates the analysis domain of the LAM-1km.

3.5 Results of the forecast error at the mesoscale/convective scale

Adaptation of the global EnKF data assimilation system for convective scales required a large number of modifications. It is imperative for the new code to pass basic validation tests, which we describe in Appendix A.

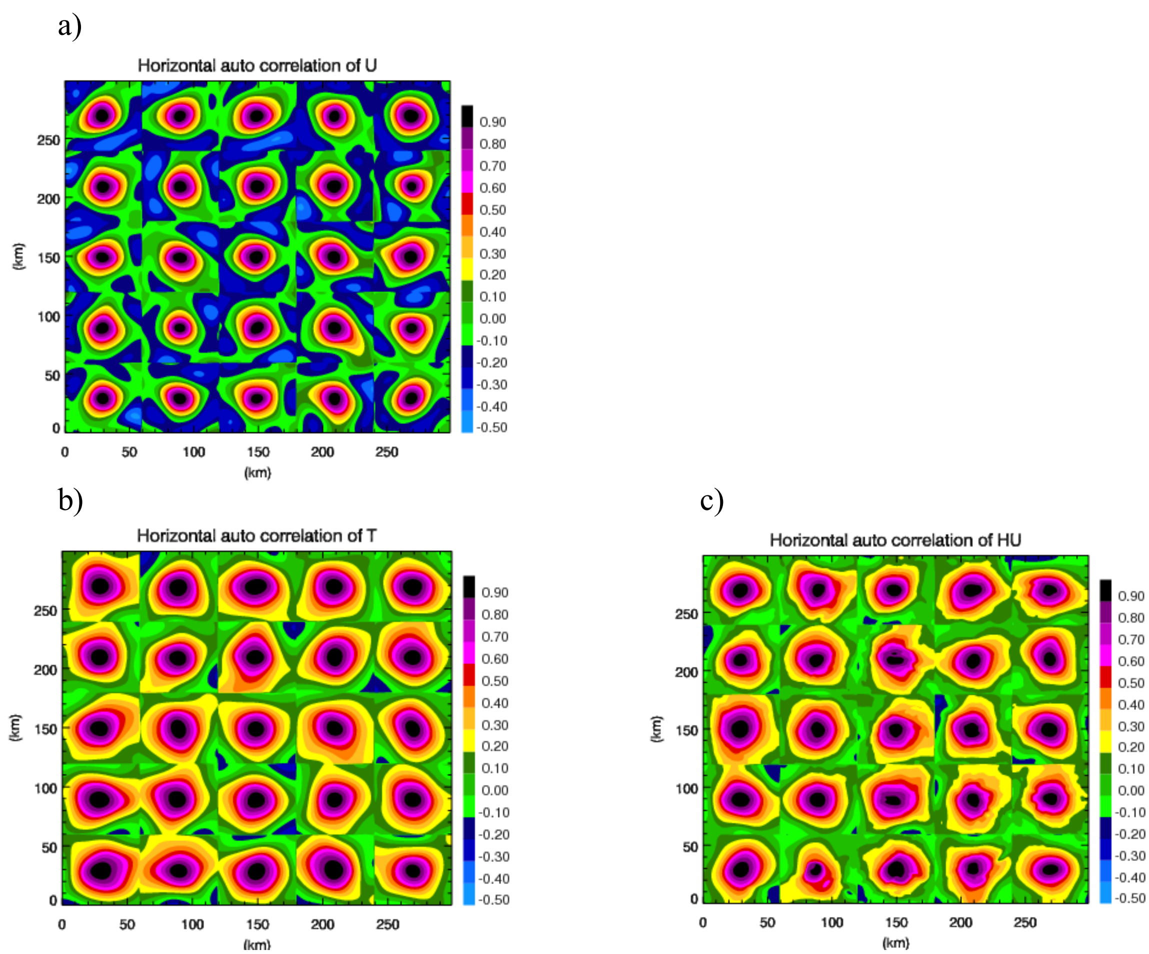

Fig. 3.5 Error correlation of 00-min forecast at 800 hPa. a) *u*-wind; b) temperature and c) humidity. The analysis domain is divided into 25 sub-domains, and the error correlation is computed with respect to the center of each sub-domain.

All the ensemble forecasts are integrated for 30 minutes with no data assimilation. Model errors have not been taken into account in the current study, therefore any forecast differences which arise are due to different initial conditions only. The ensemble forecast errors are estimated by calculating the difference between each ensemble member and the ensemble mean as defined by:

$$P^f = \overline{\varepsilon_b \varepsilon_b^{\,T}} \cong < (x_i - \bar{x})(x_i - \bar{x})^T > \qquad (3.5)$$

where $\boldsymbol{\varepsilon}_b = \boldsymbol{x}_b - \boldsymbol{x}_t$ is the difference between the background and the truth field. x_i stands for each ensemble member, $\bar{x}$ is the ensemble mean valid at the same forecasting time, and $< >$ is the ensemble average.

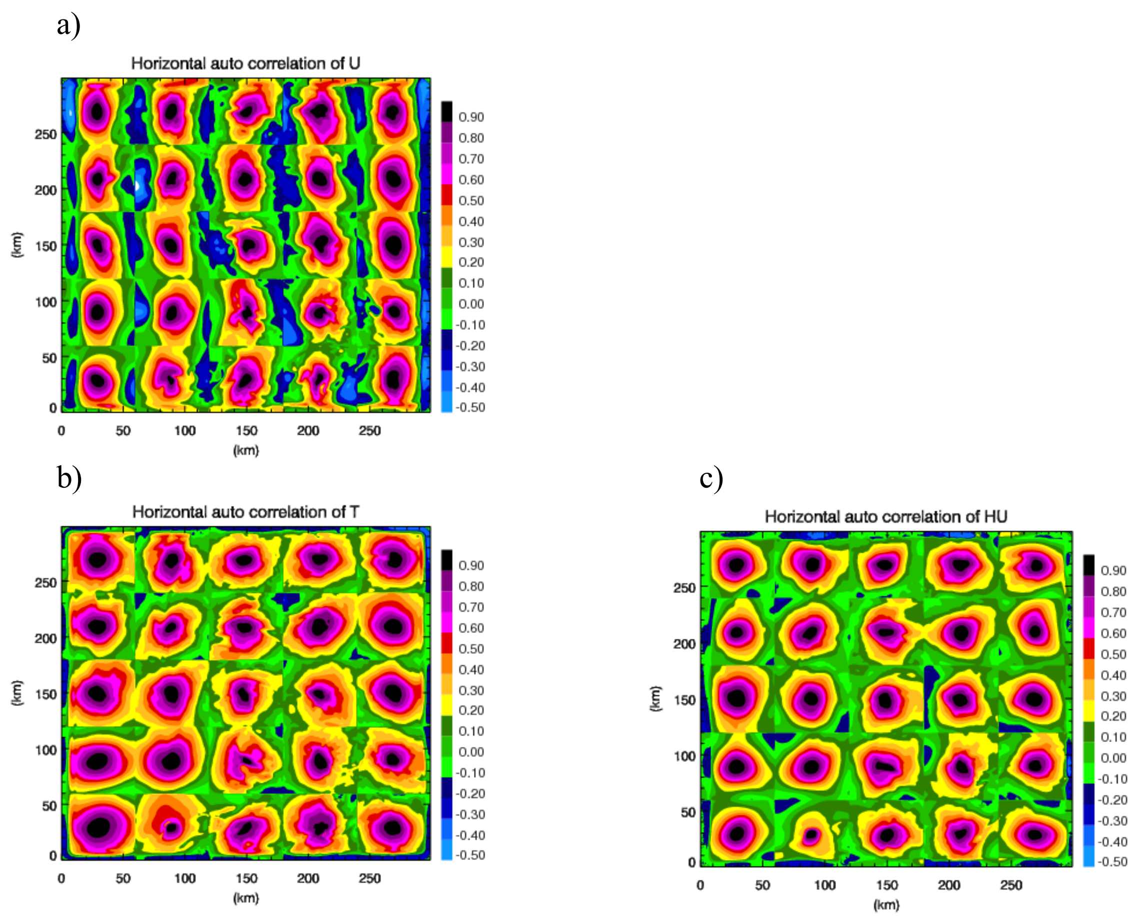

Fig. 3.6 Same as Fig. 3.5, but the error correlation of 5-min forecast.

The following results are based on the perturbations method introduced in section 3.3. By using the same random perturbation method for a range of correlation lengths appropriate for convective scales (from 10 to 20 km), sensitivity tests showed that one can obtain qualitatively similar error structures. Our study and discussions focus on the transition to situation-dependent background error covariances, and how the error structures vary in different regions, both in the horizontal and the vertical.

a. Horizontal error structure

Figure 3.5 shows the horizontal error correlations (at 800 hPa) of *u*-wind, temperature and humidity based on an 80-member forecast ensemble at the initial time (t = 0 min.). For visualization purposes, the analysis domain is divided into 25 sub-domains, and the error correlation is computed with respect to the center of each sub-domain. In general, the error structure reflects the use of homogenous isotropic initial perturbations except for the specific humidity field. This is because humidity perturbations are generated from the logarithm of specific humidity, ln(q), therefore the error structure depends on the mean state of the field. Due to sampling error, the discrepancy in each sub-domain is discernable in areas of weak correlations. The accuracy of the correlations is estimated by (Kendall et al. 1986):

$$\overline{(\rho-\hat{\rho})^2}=\frac{1}{n}(1-\rho^2)^2\approx\frac{1}{n}(1-\hat{\rho}^2)^2 \qquad (3.6)$$

where ρ stands for the real correlation, $\hat{\rho}$ is an estimate of ρ based on a set of n ensemble members. Substituting n = 80 and the value $\hat{\rho}=0.6\,(0.3)$, the root-mean-square error in the estimated correlation $\overline{(\rho-\hat{\rho})}$ is approximately 0.072 (0.1). Equation (3.6) explains why the violet and black colors in Fig. 3.5 have much less noise than other colors. Moreover, according to (3.6), the correlation would become less reliable if smaller ensemble size were used.

Figure 3.6 shows the forecast error structures that develop after 5 minutes of integration of GEM_LAM. The deformation of the forecast error of *u*-wind (same as v-wind, not shown) is manifest in each sub-domain (Fig. 3.6a) as compared to forecast error of the temperature (Fig. 3.6b) and humidity (Fig. 3.6c). The deformation of horizontal wind appears similar in all sub-domains and has longer correlation lengths compared to the error structure we specified at the initial time. Daley (1985, Fig. 1) shows error correlations of the u-wind which are similar to those in Fig. 3.6a. His study shows that when the flow has both rotational and divergent components, the error structures tend toward an oval shape (positive correlation) with negative correlation lobes in the sides, but the direction of deformation is no longer along the east-west direction for u-wind. This indicates that dynamic processes quickly affect and dominate the error structures of the u-wind in the very early stage of model integration. After 10 minutes of model integration, the errors of *u*-wind (Fig. 3.7a) evolve into various structures in each sub-domain, and the development of forecast error of temperature and specific humidity is more significant (Fig. 3.7b and 3.7c) than the errors at t = 5 min. (Fig. 3.6b and 3.6c). Furthermore, there is a strong resemblance between the temperature and humidity error structures. At 15 minutes, all the control variables exhibit the transition from purely homogeneous isotropic background-error correlations to situation-dependent correlations (not shown). The evolution of forecast errors in the first 15 minutes indicates that as the model is integrated in time, the control variables rapidly build up their own error structures based on dynamic, thermodynamic and microphysical processes. The *u*-wind error structure is established rapidly, but error structures of thermodynamic variables (temperature and humidity) evolve on a longer timescale.

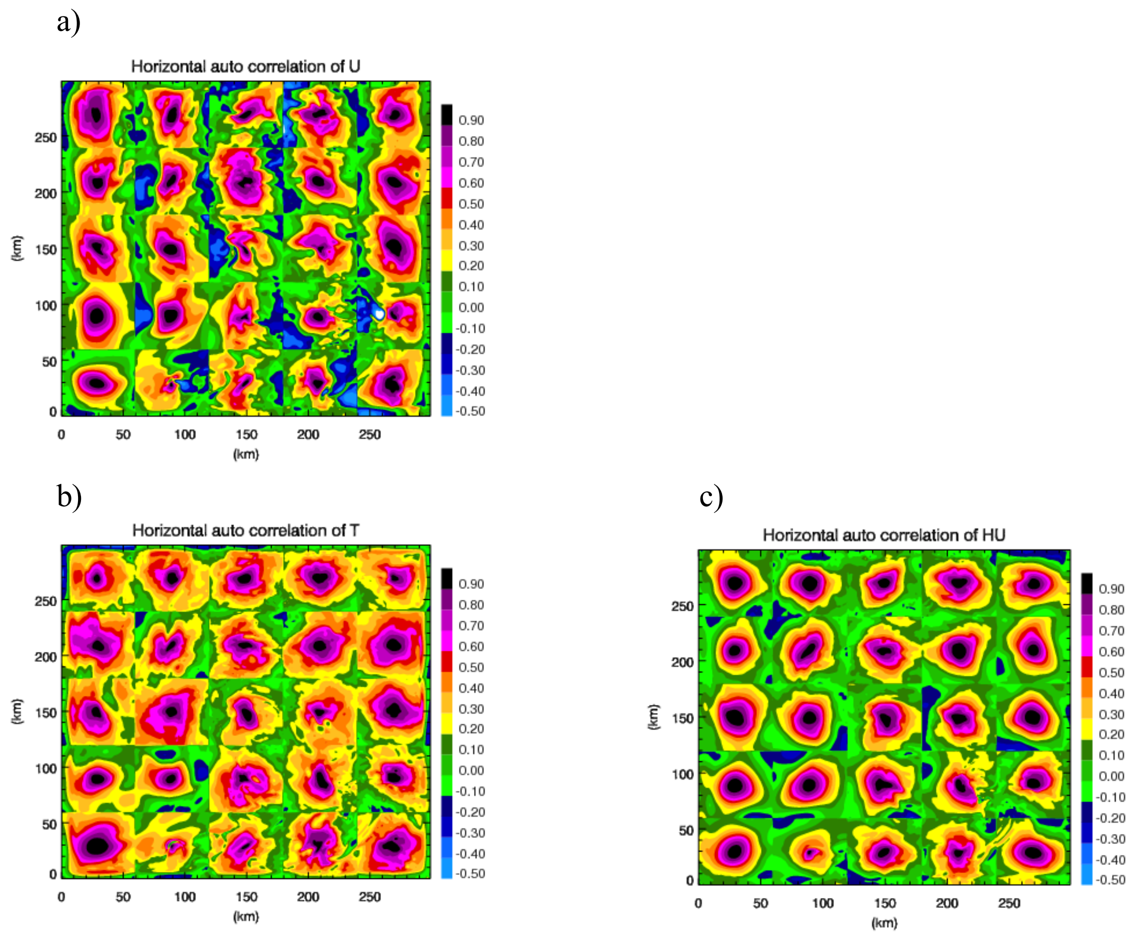

Fig. 3.7 Same as Fig. 3.5, but the error correlation of 10-min forecast.

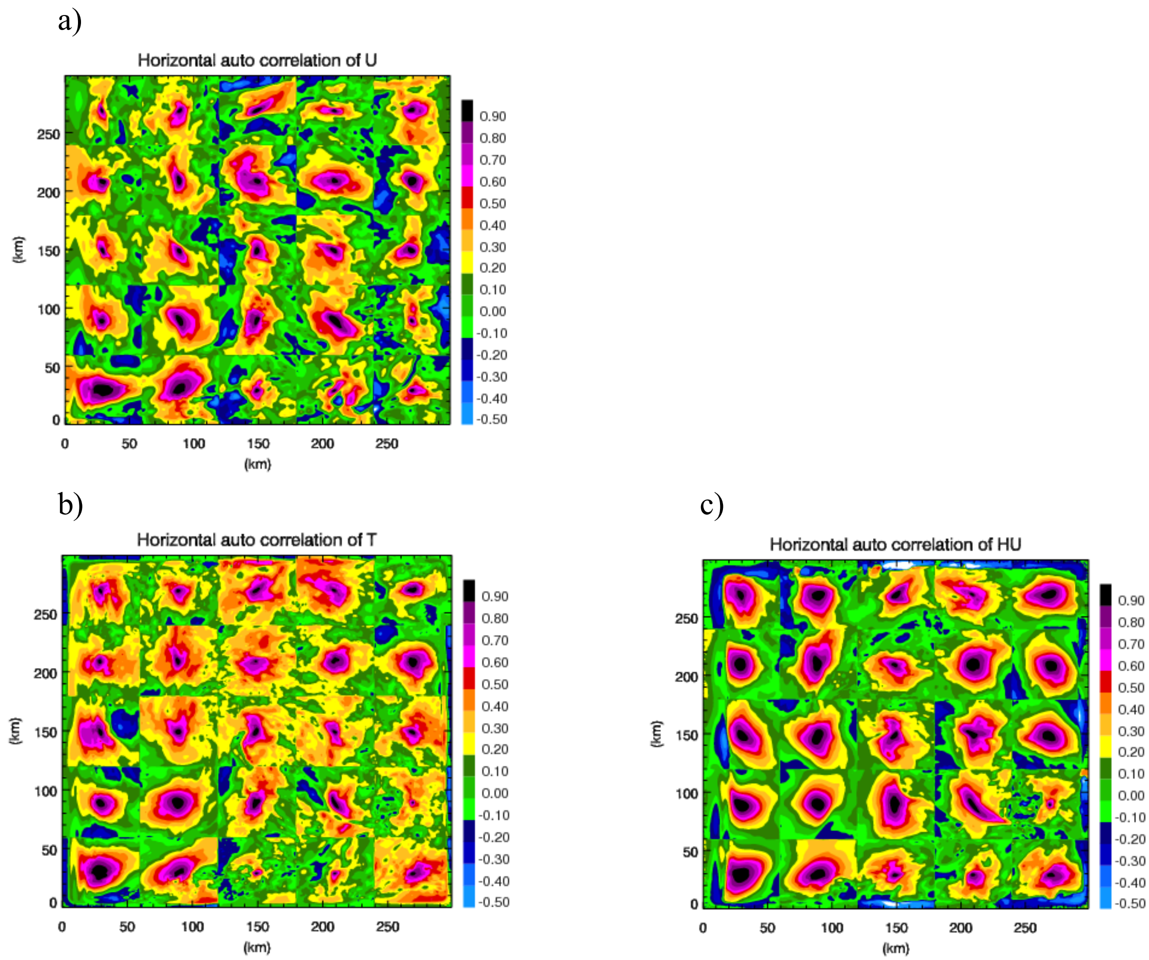

Fig. 3.8 Same as Fig. 3.5, but the error correlation of 30-min forecast.

After 30 minutes of model integration, significant heterogeneous error structure develops in the analysis domain (Fig. 3.8). The situation-dependent error structure (in each sub-domain) is present clearly in all variables. One can see that the error structures of all variables are aligned along the lateral boundaries, and that the mean flow (see Fig. 3.4b, wind vectors) affects the error structures of the wind component (Fig. 3.8a). In addition, it is evident that the correlation lengths are shorter in some of the sub-domains and longer in others. For instance, the sub-region at x=119-179, and y=0-59 shows that the error structure can be extremely localized. This is associated with tiny convection cells appearing in the southern domain of Fig. 3.4b and it suggests that this microphysical process is isolated and de-correlates quickly with other processes occurring in the surrounding environment. Moreover, the spatial deformation of the errors has different orientations in each sub-domain. Compared with the surface precipitation from the deterministic forecast in Fig. 3.4b, one can see that, in general, the error correlation length is much smaller surrounding the precipitation area and larger in the non-precipitating regions. For instance, the error correlation length in the south west of the domain (non-precipitating) is much longer than in the center and south east of the domain (precipitating).

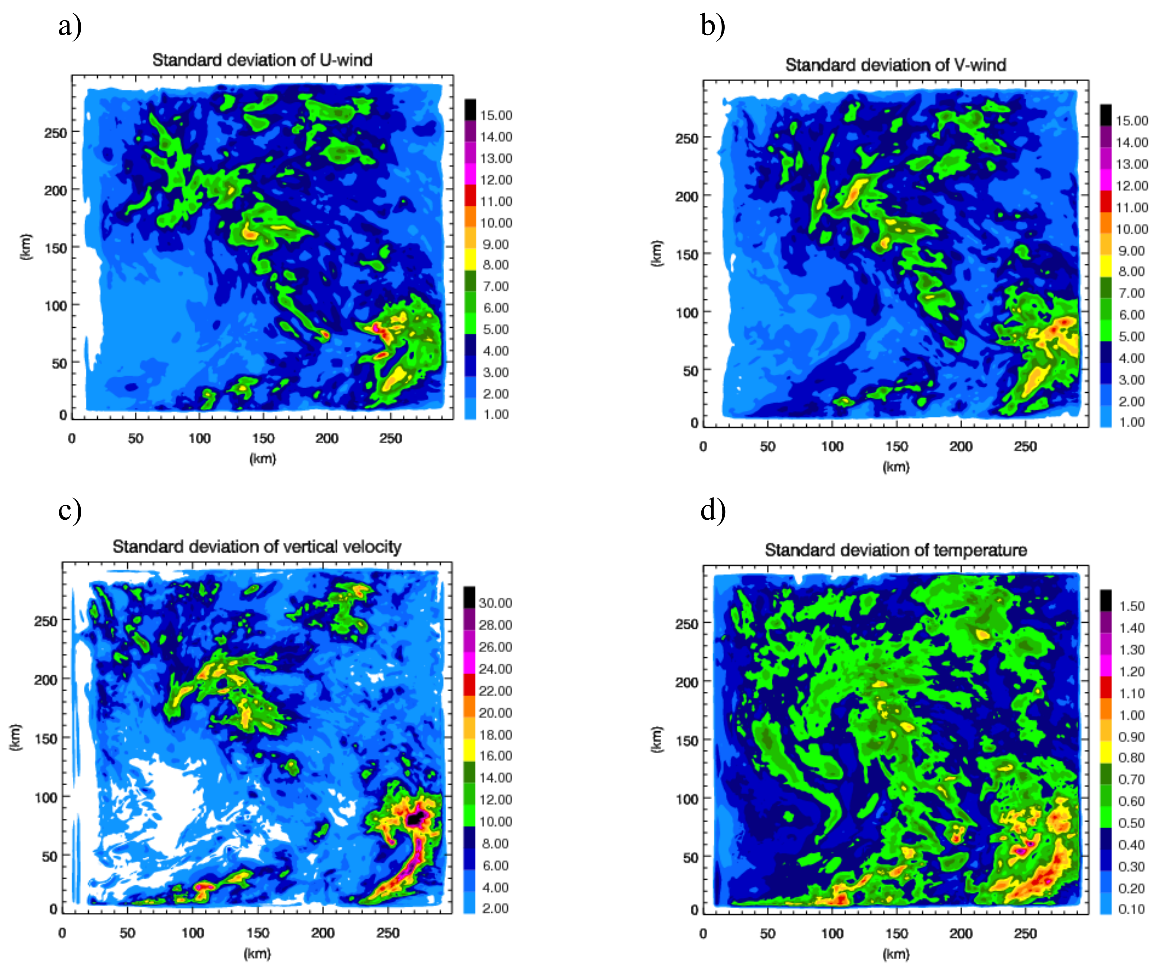

Fig. 3.9 Ensemble spread (800 hPa) of 30-min forecast. (a) u-wind [knots]; (b) v -wind [knots]; (c) vertical velocity [Pa s^{-1}]; (d) temperature [K].

Next, we examined the performance of short-term forecasts. Compared with the control run, the 80 ensemble members exhibit a variety of intensities and locations of precipitation. However, none of the forecasted precipitation patterns resemble the radar observations at 0030 UTC July 22 2010 (not shown). The ensemble spread in the horizontal illustrates the uncertainty in numerical forecasts in space. The ensemble spread for horizontal wind (u,v), vertical velocity (w) and temperature (T) at 800 hPa corresponding to the 30-min forecast is plotted in Fig. 3.9. The very small values of spread, visible near the boundaries in all variables, are a result of the lack of perturbations in the lateral boundary conditions. Larger values of spread occur near the two main weather systems and in the southern part of the analysis domain. In addition, relatively small ensemble spread is visible in the south-west portion of the domain, which is a region without precipitation in most of the ensemble forecasts. The ensemble forecasts exhibit very little precipitation in the south-west of the domain because the atmosphere is relatively stable over that area, and therefore the uncertainty is small. Furthermore, localized convective storms occur in the southern part of the domain. The intensity and the location of the storms vary from one member to another, so the uncertainty is large over that area. Moreover, the ensemble spread reveals that the precipitation system in the south-east corresponds to higher uncertainty compared to the system in the north of the domain.

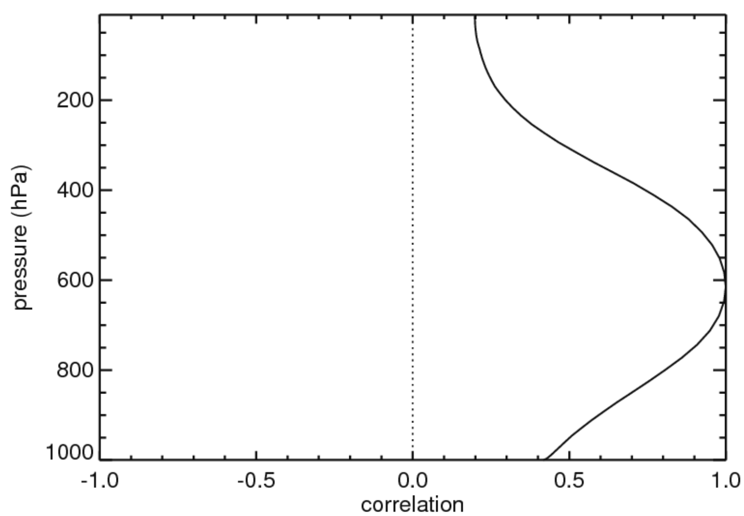

Fig. 3.10 Vertical error correlation of temperature applied in the entire domain at initial time (t=0-min forecast).

b. Vertical error structure

Figure 3.10 shows the vertical correlation structure obtained from the background-error simulator which used to generate the initial ensemble of perturbations. Correlations shown are relative to the 600 hPa pressure surface. As we have already shown for the horizontal structure of forecast error, the vertical structure also develops situation-dependent features rapidly, i.e. within the first 15 minutes of the forecast. Vertical profiles of the error correlation for temperature corresponding to the 30-min forecast are presented in Fig. 3.11 with 25 sub-domains (as before, the error correlation is computed with respect to the center of each sub-domain). The temperature vertical error correlation exhibits different structures in different sub-domains. It is recognizable that the vertical profiles are quite different in non-precipitating (south-west of the domain) and precipitating areas. We select three areas (see Fig. 3.11) in the analysis domain for further examination of the vertical error structure: sub-domain #7 (no-precipitation), #24 (precipitation), and #10 (precipitation). All members forecasted precipitation in sub-domain #10 and #24, although with different intensities and patterns.

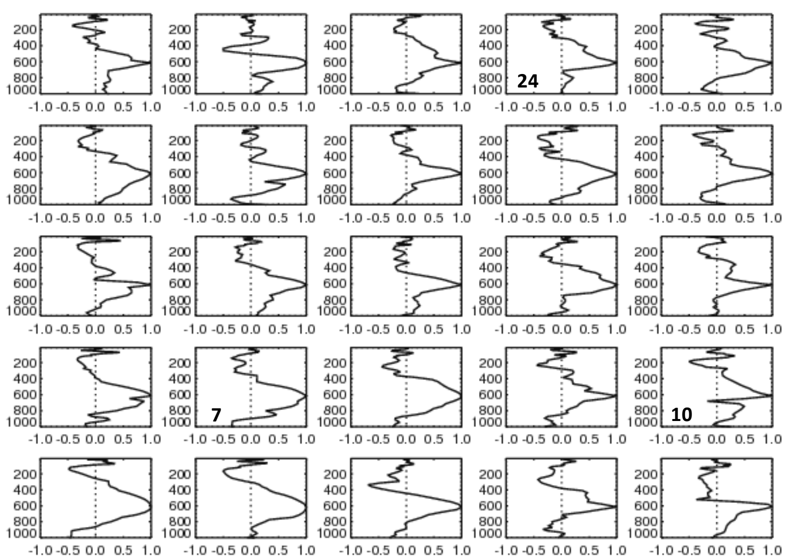

Fig. 3.11 Vertical error correlation of temperature at t=30-min forecast. The y-axis corresponds to pressure level [hPa]. The error correlation is computed with respect to the center of each sub-domain at approximately 600 hPa. The numbers indicate the sub-domains to be examined in Fig. 3.12.

The vertical error structure is computed in each sub-domain and averaged over the area of the sub-domain (3600 grid points). Figure 3.12a presents the vertical error structure in sub-domain #7, which is the non-precipitating sub-domain. The error in the vertical is nearly a symmetric structure and the correlation length is slightly shorter than 200 hPa (initial correlation).

In addition, negative error correlations occur at high and low levels of the profile. This is the typical temperature vertical error correlation structure observed in large-scale data assimilation systems related to the hydrostatic balance over non-precipitating areas (see Fig. 13 in Gustafsson et al 1999). We emphasize that the original random perturbations prescribed have a Gaussian vertical structure without negative lobes. However, as the 30-min forecast indicates, once the model is launched, the temperature rapidly develops error structures with such negative lobes over non-precipitating regions. On the other hand, the vertical profiles in sub-domain #24 (Fig. 3.12b) and sub-domain #10 (Fig. 3.12c) exhibit shorter correlation lengths in the vertical and the correlation structure is no longer close to symmetric as in sub-domain #7 (Fig. 3.12a), but rather more correlated above the reference level (600hPa).

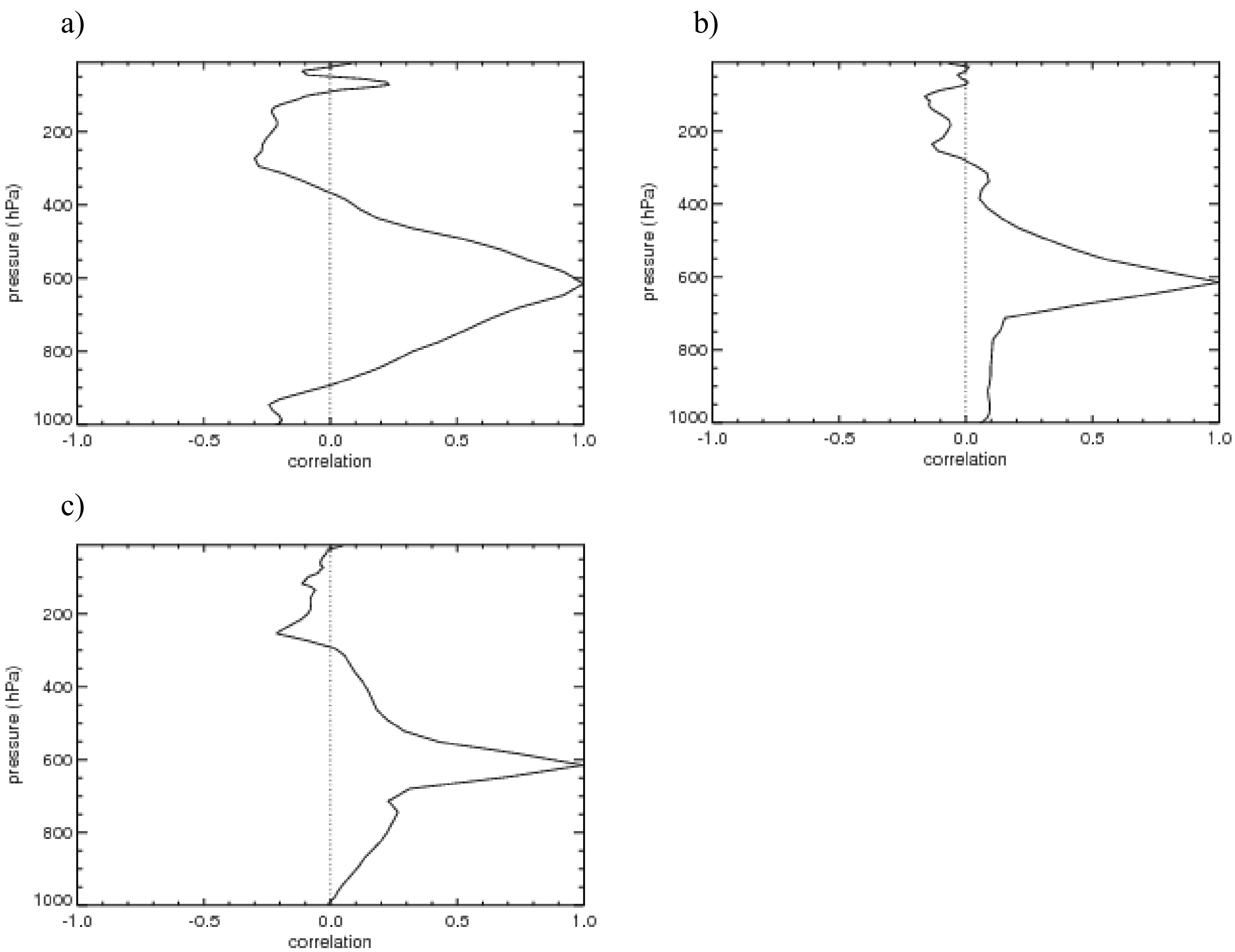

Fig. 3.12 Vertical error correlation of temperature of 30-min forecast in a) sub-domain #7; b) sub-domain #24; c) sub-domain #10. The vertical error structure is computed at approximately 600 hPa and averaged in each sub-domain (3600 pixels).

Since microphysical processes are the main difference between the precipitation and no-precipitation areas, we suspect that these processes play an important role in determining the vertical error structure of temperature. To examine the details of the vertical error structure in precipitating regions, the temperature tendencies are computed, being careful to discriminate between dynamics and physics contributions. Figure 3.13 shows the ratio of temperature tendencies due to physics and dynamics ($\text{Ratio} = \frac{|F_{\text{T-physics}}|}{|F_{\text{T-dynamics}}|}$) at 600 hPa for the ensemble mean. $F_{\text{T-dynamics}}$ is defined as $[-\vec{V} \cdot \nabla T - \omega(\frac{\partial T}{\partial p} - \frac{RT}{c_p p})]$, where $\vec{V}$ is horizontal wind vector; T is temperature; ω is vertical motion in pressure coordinate; p is pressure; R is dry air gas constant; c_p is heat capacity at constant pressure. $F_{\text{T-physics}}$ is the temperature tendency from the physical parameterizations (radiation, condensation, etc). When the ratio is equal to or larger than 1, it indicates that the physical tendency is as important as the dynamical tendency. The plot illustrates the fact that the dynamics dominates in non-precipitating regions (white color means negligible or zero tendency due to physics); Around precipitating areas, it is quite common to see the value of the ratio larger than 1. In some locations, microphysical processes can even dominate (red and purple colors), which shows the importance of physical processes in precipitation regions.

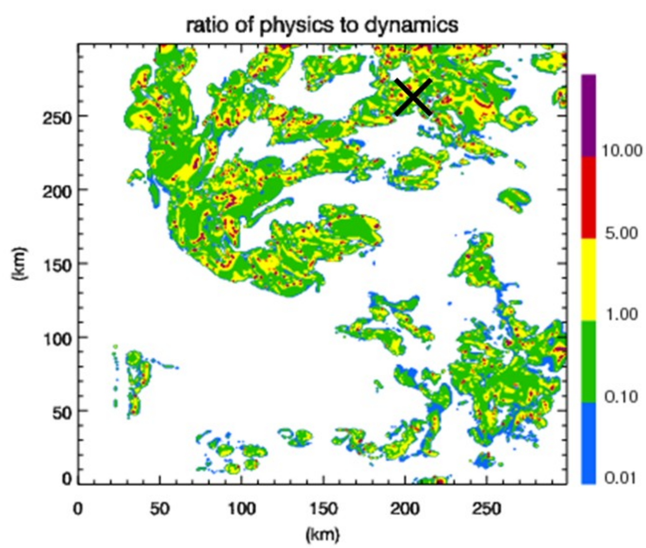

Fig. 3.13 Ratio of temperature tendencies due to physics and dynamics at 600 hPa for the ensemble mean. The cross indicates the location of imposed observation in Fig. 3.14a.

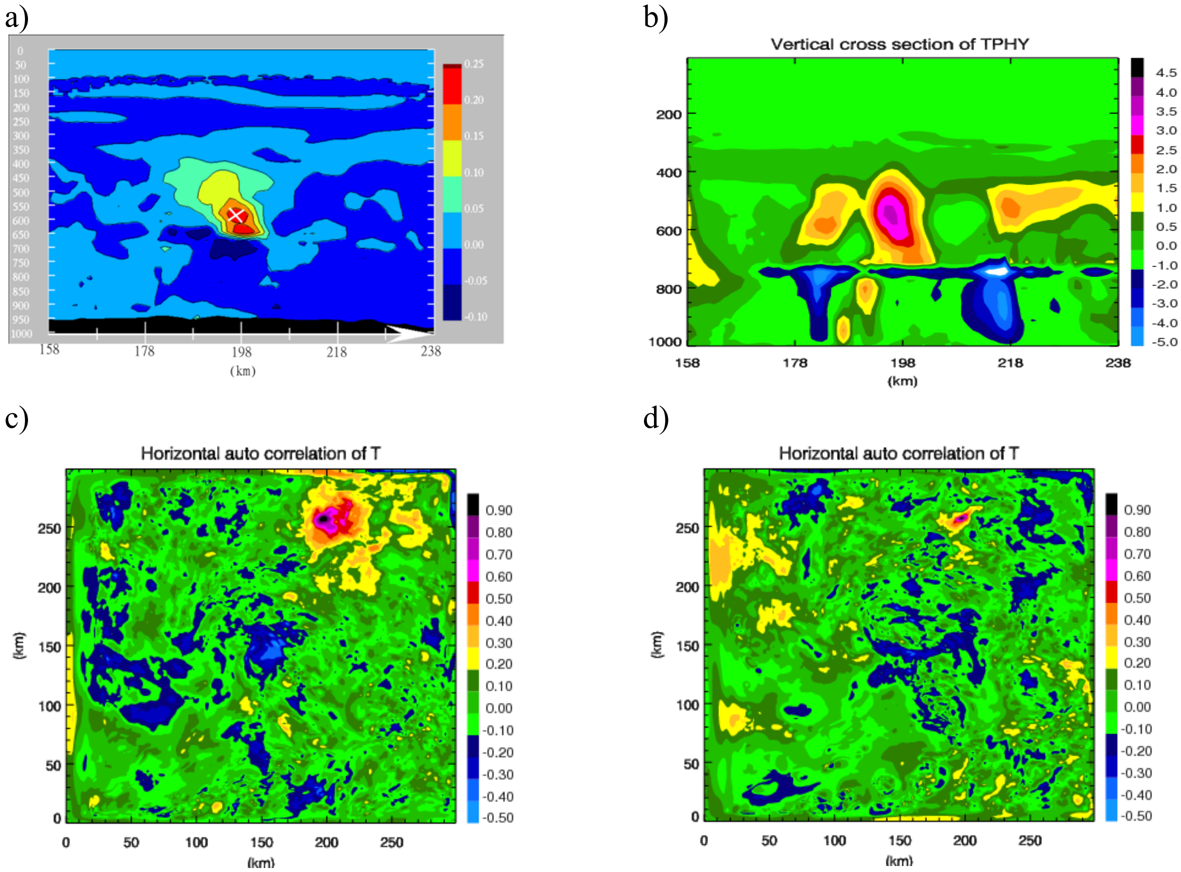

Fig. 3.14 The cross-section of a) temperature increments in sub-domain #24 from a single observation test of 30-min forecast (contour interval: 0.05 degree; the white cross indicates the location of imposed single observation and shadow near surface is the topography); b) ensemble mean of total temperature tendency [K s^{-1}] of 30-min forecast due to physics in sub-domain #24. The y-axis corresponds to pressure level [hPa]. Error correlation of temperature of 30-min forecast at: c) 800 hPa; d) 600 hPa. The error correlation is computed with respect to the location of single observation test (x=198, y=258).

To examine this issue further, we imposed a simulated temperature observation near 600 hPa at x=198, y=258 in sub-domain #24 (see the cross in Fig. 3.13). Figure 3.14a shows the vertical increment of temperature cross-section at point A (158<x<238 and y=258). This single-observation test showed that the increment is of significant (positive) amplitude between 650 hPa and 400 hPa. This feature matches the average of vertical error structures in sub-domain #24 (Fig.

3.12b). Furthermore, the ensemble mean of total temperature tendency due to the physics is plotted in Fig. 3.14b. The vertical-cross section shows that most of the heating is localized between 700 hPa and 400 hPa, and has a vertical spread corresponding to the vertical increment in Fig. 3.14a. We have confirmed that most of the contribution to the physics temperature tendency comes from condensation (not shown), which suggests that localized diabatic heating contributes to such a narrow vertical error structure. The horizontal error correlations of temperature at t = 30 min. at the location of the imposed observation are plotted in Fig. 3.14c and 3.14d. The correlations are much shorter at mid-levels (Fig. 3.14d) compared to those at low levels (Fig. 3.14c), suggesting that the error horizontal length scales tend to be larger at low levels, where dynamics plays a dominant role, whereas the correlations are relatively localized in the horizontal and vertical at levels where microphysical processes are more active.

Our study clearly demonstrates that the error structures are quite different in non-precipitating and precipitating regions. Similar conclusions were found in other studies (e.g. Caron and Fillion 2010, Montmerle and Berre 2010). As part of their 3D-VAR assimilation system, Montmerle and Berre (2010) used a strategy for modeling background error correlations based on discrimination between precipitating and non-precipitating regions as indicated by radar observations. The HREnKF data assimilation system indicates that care should to be taken when attempting such an approach. To illustrate this point, in Fig. 3.15a we show the area-averaged (1800 grid points) vertical error structure in the region defined by the black box in Fig. 3.4b, where no surface precipitation occurs in any of the 15-min. ensemble forecasts. The temperature error correlation, computed at approximately 600 hPa, resembles the characteristic correlation for precipitating regions (with a narrow and asymmetric error correlation) as in Fig. 3.12b and 3.12c. Figure 3.15b shows an example of a cross-section (east-west, see the arrow in Fig. 3.4b) of the cloud mixing ratio from one ensemble member. Even though there is no precipitation at the surface over this area, clouds have developed. This means that once physical parameterization processes become active, the vertical error structures change rapidly before the onset of precipitation.

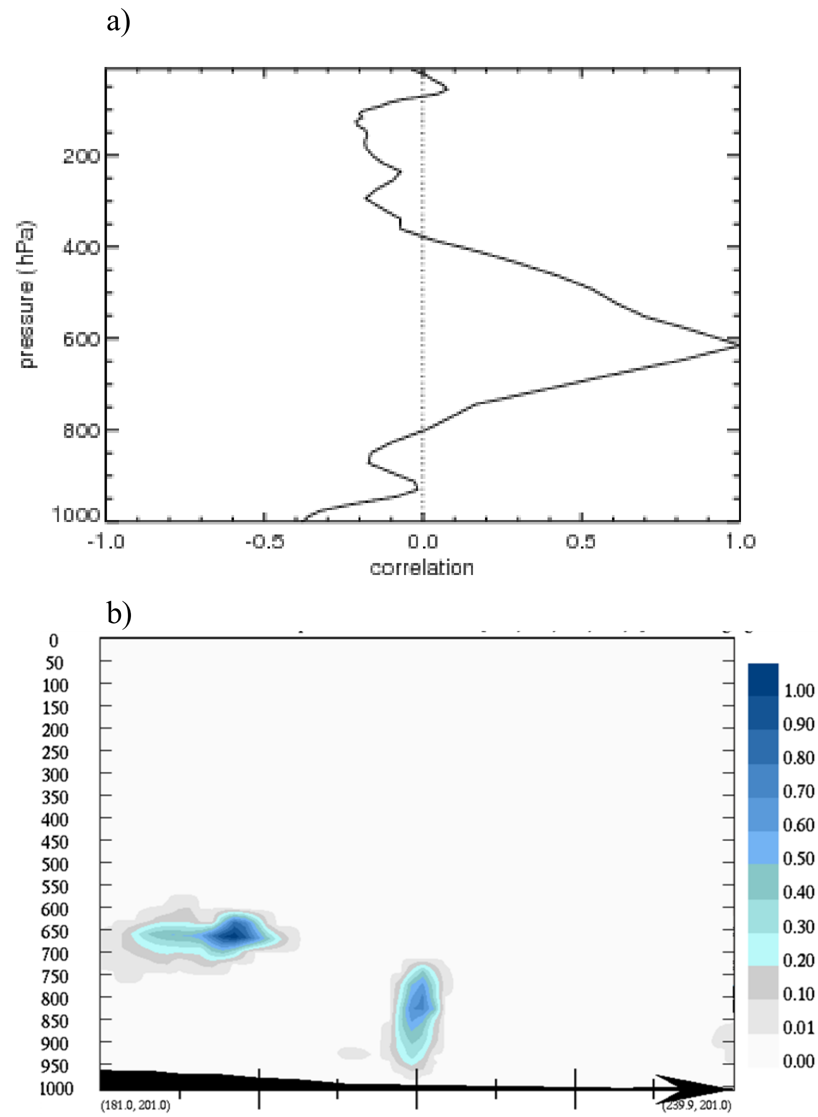

Fig. 3.15 a) Averaged vertical error correlation of temperature over the "non- precipitating" region of 15-min ensemble forecast (the error correlation is computed at approximately 600 hPa over 1800 pixels, see black box in Fig. 3.4b); b) East-west (arrow line in Fig. 3.4b) cross-section of cloud mixing ratio [g kg-1] from one ensemble member. The shadow near surface is the topography.

3.6 Summary

For the purposes of data assimilation at cloud-resolving scales, as well as the future assimilation of radar data, the global EnKF system at the Canadian Meteorological Center has been modified for a high-resolution LAM grid. This system is called HREnKF.

This study focused on investigating the forecast error at the convective scale with a summer case valid on July 22nd 2010. With an 80-member ensemble, the forecast error correlation structures evolve and exhibit a "situation dependence" rapidly after launching the GEM_LAM, typically within 15 minutes. In addition, we found that the situation-dependent error structures for different control variables tend to develop on different time scales. Dynamic variables such as horizontal wind evolve faster than the thermodynamic variables (temperature and humidity), and the humidity error typically resembles the temperature error. The error variances derived from ensemble forecasts (e.g. from 30-min. integrations), illustrate the uncertainty of weather forecasts at cloud-resolving scales. Larger error variances tend to be found inside and around regions of precipitation (both embedded storm cells and mesoscale systems forced by large scale motions), while the error variance usually remains small in non-precipitating areas where the atmosphere is stable. Furthermore, an examination of the forecast error in the horizontal and the vertical plane demonstrates that the error structures are characteristically different in precipitating and non-precipitating regions. By computing the temperature tendencies due to dynamics and physics, we have shown that microphysical processes are as important as dynamics at convective scales. The ensemble mean of the temperature tendency due to physics confirmed that diabatic heating is the major factor which modifies the temperature error structure. This indicates that the error structures both in the horizontal *and* vertical need to be addressed carefully at convective scales. Furthermore, our study shows that once microphysical processes are active, the error structures change rapidly before precipitation occurs.

The next step following this study is to assimilate McGill S-band radar data in the system. We plan to examine and report on the impact of assimilating radar data using a set of summer and winter cases.

APPENDIX A

Validation of the HREnKF system

A single-observation experiment is performed for validation of the HREnKF analysis procedure. This experiment also allows us to examine the actual analysis response based on forecast error structures provided by the HREnKF system.

a. Validation experiments and sampling errors

The experiment is performed with 80 ensemble members, and we impose the single test observation at the center of the analysis domain (x=150, y=150). A simulated temperature innovation of 1 degree with a standard deviation error of 1 degree is imposed at 850 hPa. The horizontal localization distance is 60-km, and the vertical localization is configured to force the covariances to zero at a distance of 2 scale heights.

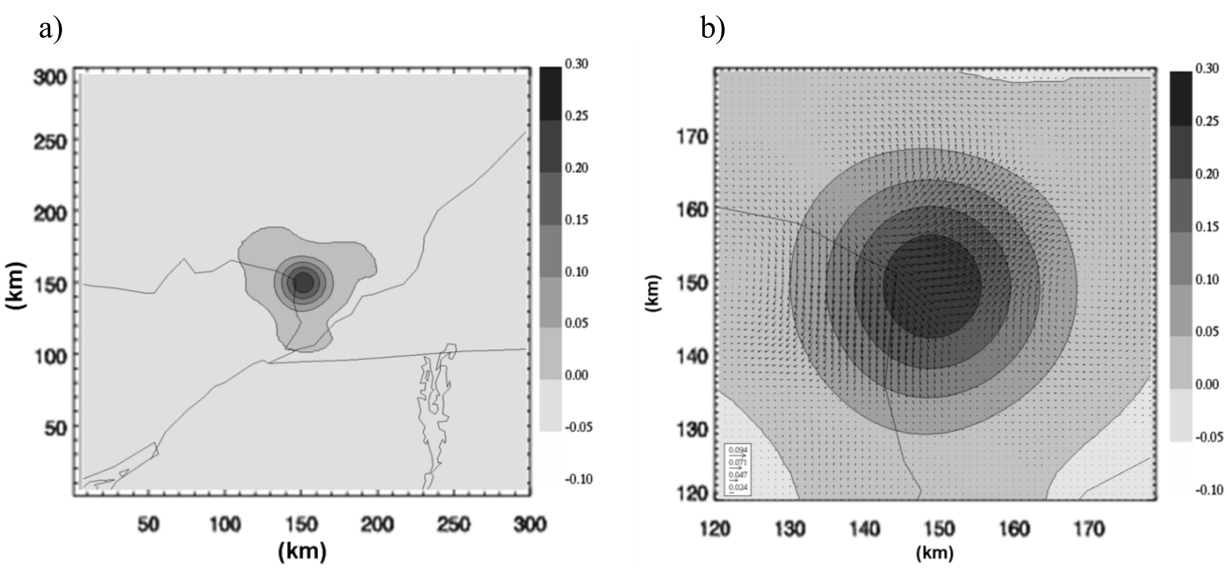

Fig. 3.16 Single observation experiment based on the 80-ensemble member of the HREnKF of initial time: a) temperature increment at 850 hPa; b) increment of temperature and horizontal wind vectors (zoom-in of the analysis domain centered at the observation). The contour interval is 0.05 degree and vectors are in units of knots. The single observation is at the center of the analysis domain (x=150, y=150).

Figure 3.16a shows the temperature analysis increment for the HREnKF analysis. The increment is nearly isotropic in space, which reflects the prescribed error structure. The amplitude of the horizontal analysis increment decreases to zero at about 60-km from the imposed observation (heavy solid contour line), which is consistent with the prescribed localization distance. The maximum increment of 0.25 degree is at the observation location. This is precisely consistent with Eqs. (3.1), (3.2) when use is made of the ensemble estimated forecast error variance at the observation point (estimated as 0.57 degree).

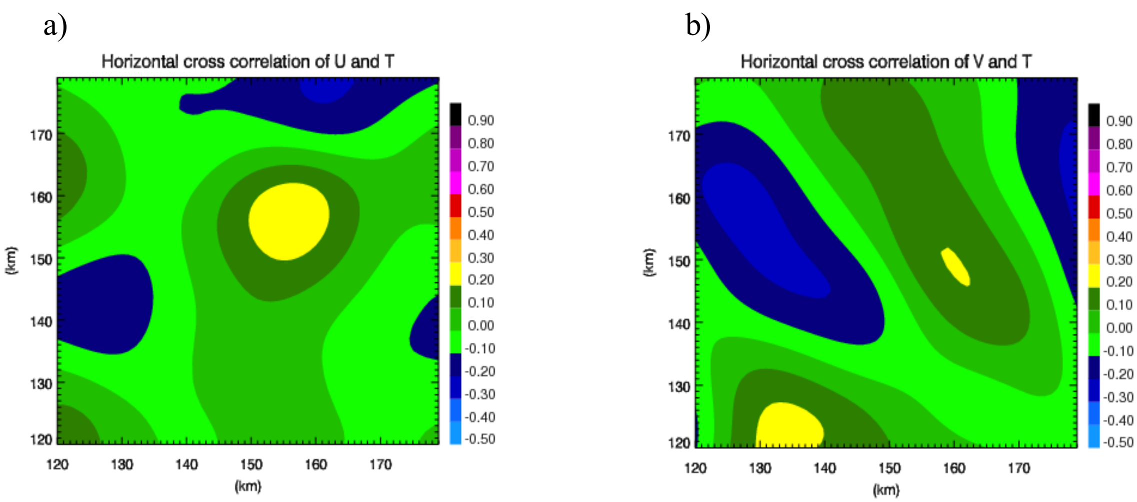

Fig. 3.17 Error cross-correlation based on 80-member ensemble of the HREnKF of initial time. a) u and T; b) v and T (zoom-in of the analysis domain as Fig. 3.16b).

To provide an estimate of the side effect of error sampling, we illustrate the impact of the simulated temperature observation on wind analysis increments. Figure 3.16b zooms in on the center of the increment area, and the increment of the horizontal wind (vectors) and temperature (contours) are plotted. Note that in principle, the cross-correlation of temperature and winds should be zero due to our original correlation modeling assumptions. However, when the multivariate probability density function is sampled by a limited number of ensemble members, noises or non-zero values in the cross-correlation are introduced as shown in Fig. 3.17. Figures 3.17a and 3.17b present the error cross-correlations between temperature and u (v) components respectively, based on 80 ensemble members. The correlation between temperature and wind explains clearly the horizontal wind increments due to the temperature observation. Based on the cross-correlation values in Fig. 3.17 (between -0.3 to 0.3), we see that according to Fig. 3.16b, perceptible, random divergent circulations can be induced by our algorithm due to the finite sample size. We speculate that this phenomenon can potentially trigger fictitious deep convection in circumstances where poor ensemble size and/or too permissive innovation data (i.e. poor data quality control) are present. The strong nonlinearity of convective scale flow thus requires special care regarding error sampling issues.

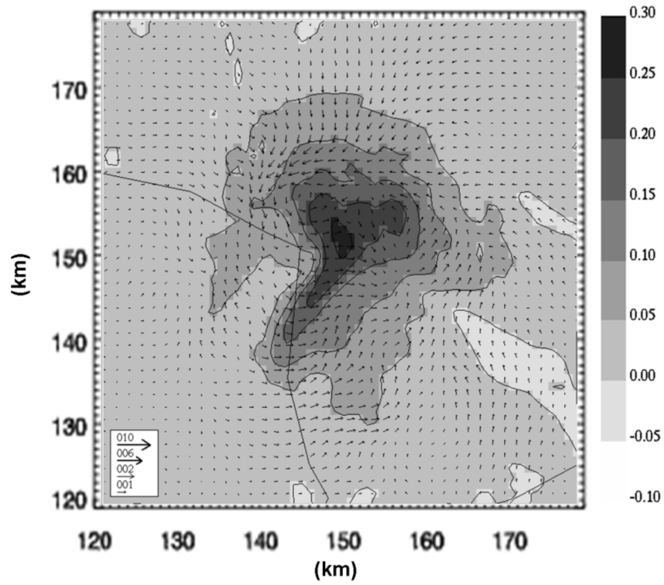

Fig. 3.18 Single observation experiment based on the 80-member ensemble of the HREnKF of 30-min forecast: temperature and horizontal wind increment at 850 hPa. (zoom-in of the analysis domain as Fig. 3.16b). The contour interval is 0.05 degree and the vectors are in units of knots. The single observation is at the center of the analysis domain (x=150, y=150).

b. Transition to situation-dependent covariances

In this experiment, we examine a single-observation result based on the ensemble of forecast in HREnKF. The prescribed innovation and observation error are the same as before, and the location is again at the center of the analysis domain (x=150 and y=150).

Figure 3.18 shows increments of the temperature and wind after the model was integrated in time with the HREnKF. The temperature increment clearly exhibits the situation-dependent structure of the forecast error built up from ensemble members. In the vertical plane, the temperature increments (Figs. 3.19 a and b) exhibits a tilted structure which may play a role at mesoscales and convective scales.

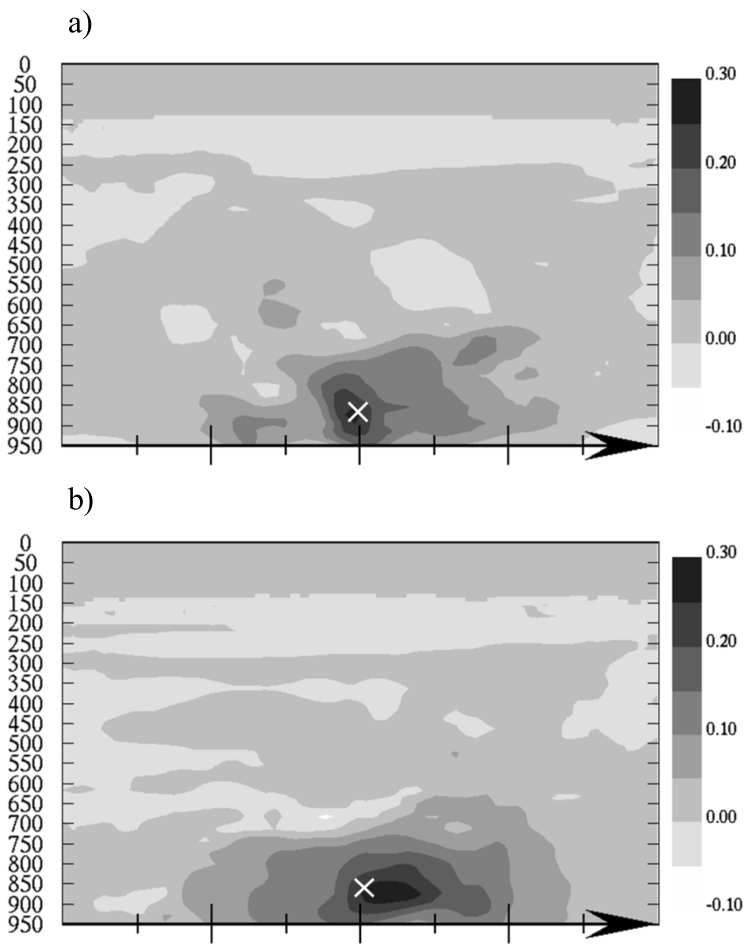

Fig. 3.19 Cross-sections of the temperature increment at the location of the imposed observation: a) west-east direction; b) south-north direction. (y-axis is pressure [hPa], the cross indicates the location of single observation)

To examine how the wind changes in response to the single temperature observation, the error cross-correlation between u (v) and temperature (T) is plotted in Fig. 3.20a (b). The error cross-correlations between winds and temperature are stronger than the ones in Fig. 3.17, and the background error structure is a result of the dynamical and microphysical processes inherent in the model forecast.

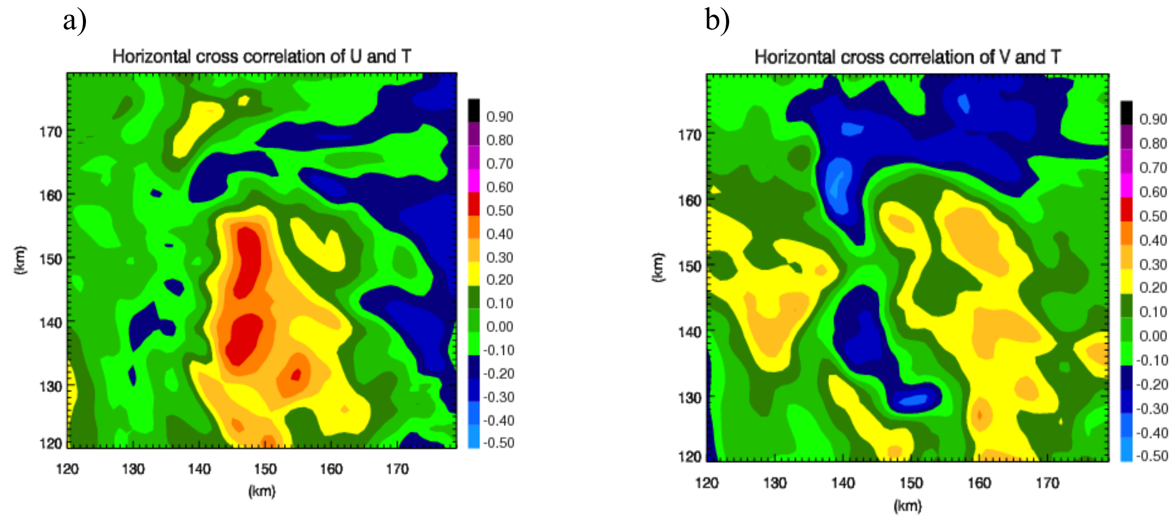

Fig. 3.20 Error cross-correlation for the same domain as in Fig. 3.17 based on 80-member ensemble of the HREnKF of 30-min forecast. a) *u* and *T*; b) *v* and *T*.

Chapter 4

Radar Data Assimilation in the Canadian High Resolution Ensemble Kalman Filter System: Performance and Verification with Real Summer Cases

The results in chapter 1 give some advices for the implementation of Ensemble Kalman Filter (EnKF) system, such as sufficient initial ensemble spread and data thinning. Chapter 2 provides information about the background error statistics which can be used to setup the localization scheme in EnKF.

Based on the studies in the previous chapters, a high resolution (1-km) EnKF system is developed for radar data assimilation. Similar to the operational global EnKF system at the Canadian Meteorological Center, this high resolution EnKF includes parallel sub-EnKFs to maintain a sufficient ensemble spread during the cycling process. After the implementation, this system is applied on different summer cases with different precipitation structures in order to investigate its performance. Short-term ensemble forecasts are initialized from the analysis results of the EnKF system for the purpose of verifying the impact of EnKF on short-term forecast.

This chapter is based on the following journal article.

Chang, Weiguang, Kao-Shen Chung, Luc Fillion, and Seung-Jong Baek, 2014: Radar Data Assimilation in the Canadian High Resolution Ensemble Kalman Filter System: Performance and Verification with Real Summer Cases. Mon. Wea. Rev., In press.

Chapter 4

Radar Data Assimilation in the Canadian High Resolution Ensemble Kalman Filter System: Performance and Verification with Real Summer Cases

Abstract

An 80-member High Resolution Ensemble Kalman Filter (HREnKF) is implemented for assimilating radar observations with the Canadian Meteorological Center (CMC)'s Global Environmental Multiscale Limited Area Model (GEM-LAM). This system covers the Montréal region and assimilates radar data from the McGill Radar Observatory with 4-km data thinning. The GEM-LAM operates in fully non-hydrostatic mode with 58 hybrid vertical levels and 1-km horizontal grid spacing. As a first step towards full radar data assimilation, only radial velocities are directly assimilated in this study. The HREnKF is applied on three 2011 summer cases having different precipitation structures; i.e. squall line structure; isolated small-scale structures; and wide spread stratiform precipitation. The short-term (< 2h) accuracy of the HREnKF analyses and forecasts is examined.

In HREnKF, the ensemble spread is sufficient to cover the estimated error from innovations and lead to filter convergence. It results in part from a realistic initiation of HREnKF data assimilation cycle by using a Canadian Regional EnKF system (itself coupled to a global EnKF) working at meso and synoptic scales. The filter convergence is confirmed by the HREnKF background fields gradually approaching to radar observations as the assimilation cycling proceeds. At each analysis step, it is clearly shown that unobserved variables are significantly modified through HREnKF cross-correlation of errors from the ensemble. Radar reflectivity observations are used to verify the improvements in analyses and short-term forecasts achievable by assimilating only radial velocities. Further developments of the analysis system are discussed.

4.1 Introduction

Since introduced by Evensen (1994), the Ensemble Kalman Filter (EnKF) has been widely used for atmospheric data assimilation (e.g. Houtekamer and Mitchell 1998; Anderson and Anderson 1999; Anderson 2001; Bishop et al. 2001; Whitaker and Hamill 2002; Tippett et al. 2003; Anderson and Collins 2007; Anderson et al. 2009). The most problematic issues addressed by these studies involve calculation efficiency and insufficient ensemble spread that could lead to filter divergence. The EnKF scheme proposed by Houtekamer and Mitchell (1998, 2001) is able to reasonably increase ensemble spread by computing more than one Kalman gain, is relatively easy to implement and parallelizes well. Hence a global EnKF based on this scheme is in operational use at the Canadian Meteorological Center (CMC). The operational global EnKF provides the theoretical and practical basis for our high resolution kilometric scale EnKF (hereafter referred to as HREnKF), details of which will be elaborated in the next section.

After its success for large scale data assimilation, the technique of EnKF was adopted for research purposes to assimilate radar data at mesoscale and convective scale. Snyder and Zhang (2003) explored for the first time the possibility of using EnKF to assimilate radar observations. By assimilating simulated radial velocity into a perfect cloud-scale model, their study showed that accurate analysis can be produced after six radar-scans in thirty minutes. They also indicated that flow-dependent error covariances are important for reconstructing the unobserved fields. Furthermore, a study using simulated radial velocity and reflectivity observations showed that reflectivity data in precipitation areas help to retrieve storm details, and no-reflectivity observations in non-precipitation areas are useful for suppressing false alarm storms (Tong and Xue 2005).

Compared to data assimilation of simulated observations in the context of a perfect forecast model, assimilating real radar data by EnKF is even more challenging due to the imperfect highly non-linear model, and the limited knowledge of model and observation errors. Despite those problems, results from many studies demonstrated notable improvement in both analysis and forecast from assimilating real radar data (Aksoy et al. 2009, 2010; Dowell 2004, 2011). In those studies, amplitude of innovations (i.e. observations minus background) in each cycle was consistently reduced during EnKF cycling. Short-term forecasts after EnKF cycling were improved in a few cases in terms of root mean square (rms) errors of reflectivity and radial velocity with respect to real observations.

Although some EnKF studies already dealt with real radar data, most of them focused on isolated convective systems happening within the model domain. The HREnKF in this article is carefully studied under varying weather conditions. Its impact on analyses and short-term forecasts is addressed, and the advantages and limitations of applying HREnKF for radar data assimilation are discussed. This study is an extension of Chung et al. (2013) and benefits from one more year of development work. Radar observations are provided here by McGill J. S. Marshall Radar Observatory. Experiments are performed in the context of the Global Environmental Multiscale Limited Area Model (GEM-LAM) with l-km horizontal grid spacing. For the moment, we focus on radial velocity assimilation strictly, leaving reflectivity data for the next stage of our program.

The remainder of the article is organized as follows. In the second section, the design of HREnKF is introduced including the GEM-LAM configurations, the pre-processing of observations and the observation operator used. The third section shows the setup of HREnKF experiments, introducing three summer cases, and the evaluation methodologies. Results for these three summer cases are presented in the fourth section. Finally, this article closes with a summary and discussions in the last section.

4.2 Description of HREnKF for radar data assimilation

a. The HREnKF scheme

The HREnKF inherits from the global EnKF scheme implemented operationally at CMC (Houtekamer and Mitchell 1998, 2001; Mitchell et al. 2002; Houtekamer et al. 2005; Mitchell and Houtekamer 2009). In the following discussion, the term 'global EnKF' refers specifically to this Canadian operational global EnKF. The basic equations of HREnKF are similar to the equations in Evensen (1994) and Houtekamer and Mitchell (1998). Given a number of ensemble members equally divided into a few subgroups, the fundamental HREnKF algorithm can be described by the following set of equations

$$\mathbf{X}_j^f = \mathcal{M}(\mathbf{X}_j^a + \varepsilon_j) \tag{4.1}$$

$$\mathbf{K}_i = var(\mathbf{X}_{j'}^f, \mathbf{H}\mathbf{X}_{j'}^f)(var(\mathbf{H}\mathbf{X}_{j'}^f, \mathbf{H}\mathbf{X}_{j'}^f) + \mathbf{R})^{-1} \tag{4.2}$$

$$\mathbf{X}_j^a = \mathbf{X}_j^f + \mathbf{K}_i(\mathbf{O}_j - \mathbf{H}\mathbf{X}_j^f) \tag{4.3}$$

where i =1, 2, …, is a subgroup index; j and j' represent the indices of ensemble members within and outside the subgroup i respectively. The matrix $\mathbf{K}_i$ is the Kalman gain used in subgroup i, and calculated from all the ensemble members other than the ones in i. Superscripts a and f represent analysis and forecast (i.e. background) respectively; $\mathbf{X}$ is the model state vector; $\mathbf{O}_j$ represents perturbed observation vector (Whitaker and Hamill, 2002); $\mathbf{H}$ stands for the observation operator; $\mathbf{R}$ is the observation error covariance matrix; $\mathcal{M}$ is the nonlinear forecast model; ε_j represents random perturbations added onto each analysis member to simulate model errors. The error covariance matrices in Eq. (4.2) are estimated from

$$var(\mathbf{A}_j, \mathbf{B}_j) = \rho \circ \frac{1}{N-1} \sum_{j=1\ldots N} (\mathbf{A}_j - \overline{\mathbf{A}})(\mathbf{B}_j - \overline{\mathbf{B}})^T \tag{4.4}$$

where $\mathbf{A}$ and $\mathbf{B}$ represent state vectors for different members in model space or in observation space (e.g. $\mathbf{X}_j^f$ or $\mathbf{H}\mathbf{X}_j^f$ in Eq. 4.2); j is an ensemble member index; ρ represents the localization function which will be explained later and $\rho\circ$ means a Schur product with the localization function (Houtekamer and Mitchell 2001).

Brief descriptions of HREnKF features are given in following, while the details can be found in Houtekamer and Mitchell (2001) and Chung et al. (2013).

Because of the huge size of state vector (~10^7) in model space, limited number of ensemble members (~10^2) in EnKF can hardly precisely estimate the first moment (mean) and the second moment (variances and covariances) of the multivariate background error probability density function. As a result, the problems of insufficient ensemble spread and noisy covariances usually exist in the estimation of background error statistics. Dividing ensemble members into *subgroups* and *localization* are two approaches to solve those problems.

Dividing ensemble members into several *subgroups* in HREnKF alleviates the problem of ensemble spread reduction caused by limited ensemble size (Mitchell and Houtekamer 2009). Otherwise, the filter could reject observations due to the underestimation of background uncertainties and result in filter divergence.

Three-dimensional *localization* works on top of the calculation of background error covariance matrices as shown in Eq. (4.4) in order to reduce noise effects in the estimation of covariances (Houtekamer and Mitchell 2001). The algorithm of both horizontal and vertical localizations follows Eq. (4.10) in Gaspari and Cohn (1999). According to some other studies in radar data assimilation (Dowell et al. 2004; Tong and Xue 2005; Aksoy et al. 2009), and the error correlation analysis in Chung et al. (2013), 10-km and 1 scale height (on the coordinate of natural logarithm of pressure) are realistic scale parameters in the above mentioned localization equation for horizontal localization and vertical localization respectively. The cut-off distances are twice as large as the above scale parameters. Moreover, due to the filtering mechanisms in NWP model, the *effective* model resolution is usually 5-10 times of model resolution in mesoscale (Skamarock 2004). In order to prevent the increments from being removed by the filtering effect of model integration, the localization cut-off distance (20 km) is set to be much larger than the effective resolution (5-10 km).

Sequential processing allows HREnKF to assimilate observations sequentially in batches for reducing the calculation burden (Houtekamer and Mitchell 2001). The validation of such algorithms is subject to the condition that observation errors in different batches should be uncorrelated. In our study, data thinning will be done on radar observations in order to meet this requirement, details of which will be given in subsection 4.2c.

Another feature of HREnKF is the *background check* procedure which eliminates observations that are far from the background fields (i.e. a short-term forecast). The criterion can be expressed by

$$(o - \overline{Hx^f}) > 2\sqrt{\sigma_o^2 + \sigma_f^2} \tag{4.5}$$

where o represents each single unperturbed observation; $\overline{Hx^f}$ is the ensemble mean forecast (i.e. background) mapped to the observation space for the corresponding observation; σ_o^2 is the fixed observation error variance; σ_f^2 is the flow-dependent background error variance estimated from ensemble members in observation space. Observations satisfying the inequality (4.5) are rejected by the background check. This procedure also prevents the model from being shocked by an occasional extreme update on a particular model state variable.

The above features and algorithms of HREnKF are shared with the global EnKF developed by Houtekamer and Mitchell (1998, 2001), besides which, HREnKF has its own specials. Firstly, in addition to the control variables (temperature, specific humidity, and horizontal wind components) in the global EnKF (Houtekamer et al. 2005), HREnKF has vertical velocity W as an additional control variable which contributes to the radial velocity (see Eq. 4.6) and is crucial for small scale convection. The microphysical variables are not updated directly in the analysis step, but are adjusted through model integration in the forecast step. Secondly, the time interval for analysis cycling is set as short as five minutes (as compared to 6h for the global EnKF), which is the same as the output frequency of McGill radar observations. Lastly, 80 ensemble members are employed, which are fewer than the global EnKF's 192 members, but enough to produce reliable background error structures (Chung et al. 2013).

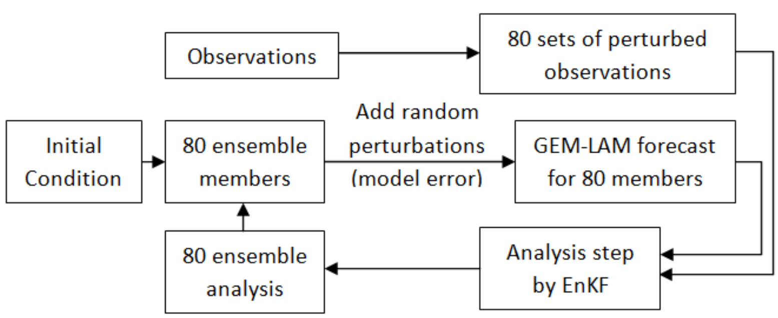

Fig. 4.1 Flow chart of HREnKF.

The HREnKF operates as shown in Fig. 4.1 and starts from 80 initial ensemble members. The approaches for providing those initial ensemble members will be given in subsection 4.3a. During the forecast step, random perturbations representing model errors are applied to ensemble members to prevent ensemble spread reduction (Eq. 4.1). Since model errors at the convective scale are not well understood, they are simply simulated here by homogenous and isotropic

Gaussian distributed random fields (Chung et al. 2013). The perturbed variables include temperature, horizontal wind components and specific humidity (standard deviations of perturbations are respectively 0.5 degree, 3 m s^{-1} and 0.1 on natural logarithm of humidity). In our experiments, following the global EnKF, perturbations are applied everywhere on the model grid, although according to Snyder and Zhang (2003), localized perturbations may be useful for preventing the spurious convective cells. Given the 80 perturbed members as initial conditions, the high resolution GEM-LAM is integrated for five minutes to yield 80 ensemble forecasts that are considered as 80 background fields ready for the analysis step. In the analysis step, 80 sets of observations are generated by perturbing real observations (Whitaker and Hamill 2002; Evensen 2003) according to their error structures modeled by Gaussian distribution and observation error standard deviation (see subsection 4.2c). The perturbed observations are then statistically combined with the background fields using the EnKF equations (Eqs. 4.2 and 4.3) to produce 80-member ensemble analysis, from which another ensemble forecasts can be performed. The above process repeats until a final analysis is produced.

b. GEM-LAM configurations

The fully compressible GEM-LAM is used in our study. The model employs an implicit scheme in time and a semi-Lagrangian advection scheme. Detailed descriptions of the GEM model dynamics and physics formulations are available in Côté et al. (1998) and Mailhot et al. (1998), respectively. As shown in Fig. 4.2, a three-level nested domain is used in the model configuration to finally drive the 1-km model. The hourly forecasts from the global grid, which used the Sundqvist condensation scheme (Sundqvist 1978), were used as initial and lateral boundary conditions to launch a limited area model in domain A with horizontal resolution of 15-km (hereafter LAM-15km). A second nested LAM forecast (domain B) starts 6 hours later than LAM-15km and runs at 2.5-km horizontal resolution (LAM-2.5km). This domain (729 x 540 grid points) covers the southern part of the provinces of Ontario and Québec. The LAM at 1-km horizontal resolution (domain C, LAM-1km) is launched 6 hours later than LAM-2.5km with integration time step of 30 s. The LAM-1km is centered over the Montréal region (300 x 300 grid points) to assimilate radar observations from McGill J. S. Marshall Radar Observatory.

The limited area simulations are fully non-hydrostatic with 58 hybrid vertical levels and a lid at 10 hPa. The land surface scheme called "Interaction between Surface, Biosphere and Atmosphere" (ISBA; see Noilhan and Planton 1989) is applied. The Kain-Fritsch moist convective parameterization scheme (Kain and Fritsch 1990) is employed in LAM-15km; however no convective parameterization is used in either LAM-2.5km or LAM-1km. As opposed to the multi-model option (different versions of physical parameterizations for different ensemble members) used in the global EnKF system, the HREnKF system currently keeps all the physical schemes fixed for model integration. The double-moment version of the Milbrandt and Yau (2005) microphysics scheme is used for the grid-scale processes. The model control variables include horizontal winds, temperature, specific humidity, vertical velocity, mixing ratio and number concentration of six hydrometeor variables (cloud water, rain, snow, ice, graupel and hail).

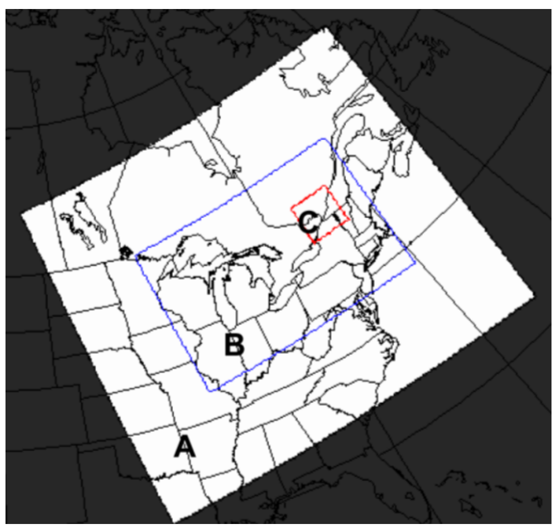

Fig. 4.2 The 1 km grid spacing GEM-LAM covering the Montréal region and its parental models. A: LAM 15 km grid spacing; B: LAM 2.5 km grid spacing; C: LAM 1 km grid spacing.

c. McGill Radar observations

The radar observations assimilated by the HREnKF are provided from the S-band dual-polarized Doppler radar at J. S. Marshall Radar Observatory operated by McGill University. The

McGill radar collects data every five minutes at 24 angles (from 0.5° to 34.4°) in elevation and 360 angles (from 1° to 360°) in azimuth. The coverage of the radar is 240 km in radius.

Before radar data are brought to the HREnKF system, J. S. Marshall Radar Observatory uses dual-polarization information such as the standard deviations of ZDR (differential reflectivity, defined as the difference between the horizontal and vertical reflectivity factors) and PhiDP (differential propagation phase shift, defined as the phase difference between the horizontally and vertically polarized echoes) to identify the ground clutters (Cho et al. 2006). Mathematical algorithms are also used to remove data contaminations including blockage effect, Doppler ambiguity and range folding (Doviak and Zrnic 1984). The measurement error of radial velocity is estimated to have a standard deviation of 1 m s^{-1} (Keeler and Ellis 2000). This value is taken in HREnKF as observation error. To keep radar data quality, the Plan Position Indicator (PPI) data are used for assimilation.

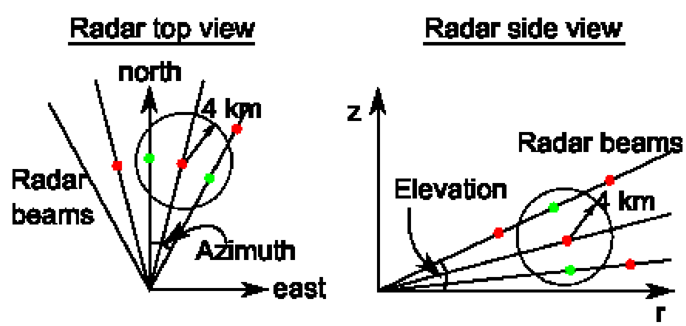

Fig. 4.3 Three-dimensional data thinning scheme for 4 km radius. Solid straight lines are radar beams. Red points are observations kept after data thinning. Green points are observations removed by data thinning.

After quality control, data thinning is applied to ensure uncorrelated observation errors, which is required for two reasons. Firstly, errors of raw radial velocity data are correlated between neighboring range gates and between neighboring beams (Xu et al. 2007; Keeler and Ellis 2000). On the other hand, their correlation structures are not fully known. Therefore, it is convenient to thin the data and ensure observation errors are uncorrelated after thinning.

Secondly, the sequential assimilation process of HREnKF is only valid under the condition that the observation errors in different batches are independent. Due to the notable observation error correlation, especially in the radar far field (Fabry 2011), we assume that errors of two observations more than 4 km away from each other are not correlated. Thus, a 4-km data thinning is applied in three dimensions on the radar data in this study (Fig. 4.3). Moreover, thinning is performed at lower elevation angles first, and then at higher elevation angles, in order to keep more observations at lower elevations, since low level winds are important for convergence and convection initiation. After data thinning, around 1/3 observations are kept from raw data.

d. Observation operator for radial velocity

Radial velocities, the only type of observation directly assimilated in the current HREnKF, can be written as a function of three wind components as shown in Eq. (4.6).

$$V_r = U\sin(\varphi)\cos(\theta) + V\cos(\varphi)\cos(\theta) + (W + V_t)\sin(\theta) \tag{4.6}$$

where U, V and W are three wind components from model output; V_t is terminal velocity for raindrops; φ and θ are azimuth and elevation angles respectively. The terminal velocity can be calculated either from model output or from reflectivity observations. In our study, similar to other studies in the literature (e.g. Sun and Crook 1997; Chung et al. 2009; Wang et al. 2013), reflectivity observations are used to calculate V_t. The relationship between V_t and reflectivity can be described by Eqs. (4.7) and (4.8).

$$Z = 43.1 + 17.5\log(M) \tag{4.7}$$

$$V_t = 5.94M^{1/8}\exp(\frac{l}{2h}) \tag{4.8}$$

where Z is reflectivity; M is precipitation concentration ($g\ m^{-3}$); l is altitude (m); h is a 10^3m scale height. Although reflectivity data are not assimilated directly by HREnKF, they are used in the observation operator for the calculation of radial velocity.

4.3 Experimental setup

a. Experiment design

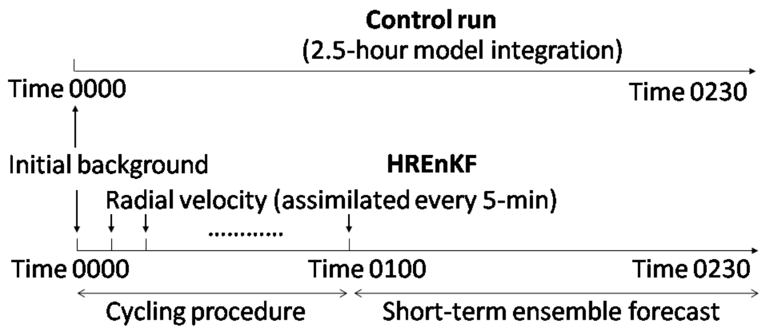

Fig. 4.4 Experiment procedure. Time 0000 indicates the start of the experiment, not the real time. Time 0230 indicates 2 hours and 30 minutes after the start of the experiments.

The experiment procedure consists of 1-h HREnKF cycling and 1.5-h short-term ensemble forecasts, which are synchronous with a 2.5-h control run (Fig. 4.4). The HREnKF cycling process begins with 5-min model integration of the 80 initial ensemble members; then assimilates observations of radial velocity every 5 minutes for 12 cycles; and finally produces an ensemble of analysis. The short-term 80-member ensemble forecasts are initiated from the final analysis ensemble and lasts for 90 min. To investigate the impact of radial velocity assimilation by HREnKF on analysis and forecast, a control run is established during the same entire experimental period.

In the experiments to follow, two different approaches are intercompared to provide 80 initial ensemble members for HREnKF and lateral boundary conditions for the high resolution GEM-LAM. In the first approach, following the preceding study (Chung et al. 2013), a deterministic forecast (as describe in subsection 4.2b) provides the initial guess at the start point of HREnKF, on which Gaussian distributed random errors are added to yield 80 initial ensemble members. The statistical properties of initial perturbations are similar to model error perturbations described in subsection 4.2a, except for their standard deviation being multiplied by a factor of two. The driving field of the deterministic forecast also provides the same lateral boundary conditions for all ensemble members in both HREnKF cycling process and short-term forecast. The control run corresponding to this approach is a model integration initiated from the initial guess. In the following text, this approach will be referred to as EXP1.

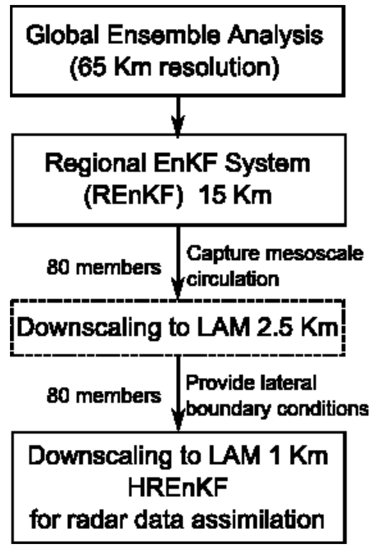

Fig. 4.5 Flow chart of HREnKF experiments with the application of the regional EnKF for capturing mesoscale circulation and providing initial and lateral boundary conditions for HREnKF data assimilation and forecasting experiments.

It is now better documented in the literature (e.g. Nutter et al. 2004a, b; Saito et al. 2012; Caron 2013) that perturbing lateral boundary conditions in ensemble forecast systems is important. Therefore, since a regional EnKF-15km system (referred to as REnKF) is currently available in research mode at CMC, the second approach assigns each member of HREnKF different initial and lateral boundary conditions from the members of the REnKF. As shown in Fig. 4.5, The REnKF takes information from the operational global ensemble analysis and then assimilates conventional observations (same types as the global EnKF) every 6 h for two cycles. Presently, results coming from extensive validation tests of REnKF demonstrate that it scores as good as the global EnKF against radiosonde observations after one month cycling (results not shown). Similar to EXP1, the second approach consists of a downscaling procedure down to 1-km horizontal grid spacing. The model configurations in LAM-2.5km and LAM-1km are exactly the same as described in subsection 4.2b. In this approach, the 80-ensemble forecasts at 2.5-km grid spacing provide the lateral boundary conditions for each member at 1-km grid spacing. We emphasize the fact that REnKF, generally better capture mesoscale circulations as compared to global EnKF, and provide larger ensemble spread for both initial ensemble members and the ensemble lateral boundary conditions. Further details on this impact on ensemble spread will be given in subsection 4.4a. Note that the control run in this context takes the ensemble mean of the 80 analysis members of 15-km resolution REnKF and then use downscaling to 1-km grid spacing. This approach is given the name 'EXP2' for simplicity in the following discussion.

In the case studies, only the first case exploits both EXP1 and EXP2, while the other two use only the second approach. The rationale for doing this will be elaborated in the next section along with the results of experiments.

b. Description of three cases

On 29 June 2011, a squall line appeared on McGill radar image and moved eastward (Figs. 4.6a and 4.6b). The HREnKF performs twelve data assimilation cycles from 0000 UTC to 0100 UTC, and the following short-term ensemble forecast is from 0100 UTC to 0230 UTC. The radial velocities in Fig. 4.6b show how observations look like and where they appear with respect to the radar location (black dot). By comparing Figs. 4.6a and 4.6b, one may notice that the colored area of radial velocity image is slightly larger than that of reflectivity. This is due to the fact that reflectivities smaller than 7 dBZ are considered insignificant compared to the noise, and therefore are not colored in the figure. The radial velocities at the same locations, however, are significant. When radial velocity observations are provided, but reflectivities are unobserved or insignificant, terminal velocity cannot be obtained by Eqs. (4.7) and (4.8) and does not contribute to the observation operator. We emphasize that the reflectivity contains more information than the radial velocity does in Fig. 4.6, because the former contains both precipitation and non-precipitation data, which is crucial for correcting position errors in data assimilation.

As discussed before, two different experiments, EXP1 and EXP2 are performed for this case, where the control runs are different. By comparing between observations (Fig. 4.6a) and the control runs for both experiments (Figs. 4.6c and 4.6d) at time 0000 UTC before the experiment starts, one can tell that the precipitation in EXP2 is more precisely located. This is a result of the ability of REnKF to track mesoscale circulations in EXP2, which reduces the error of the control run at the beginning of HREnKF. Because of the improvement brought by REnKF on better positioning the mesoscale flow in general, the next two cases will rely on REnKF for providing the initial ensemble and the driving ensemble fields. HREnKF will rather focus on improving the convective scales.

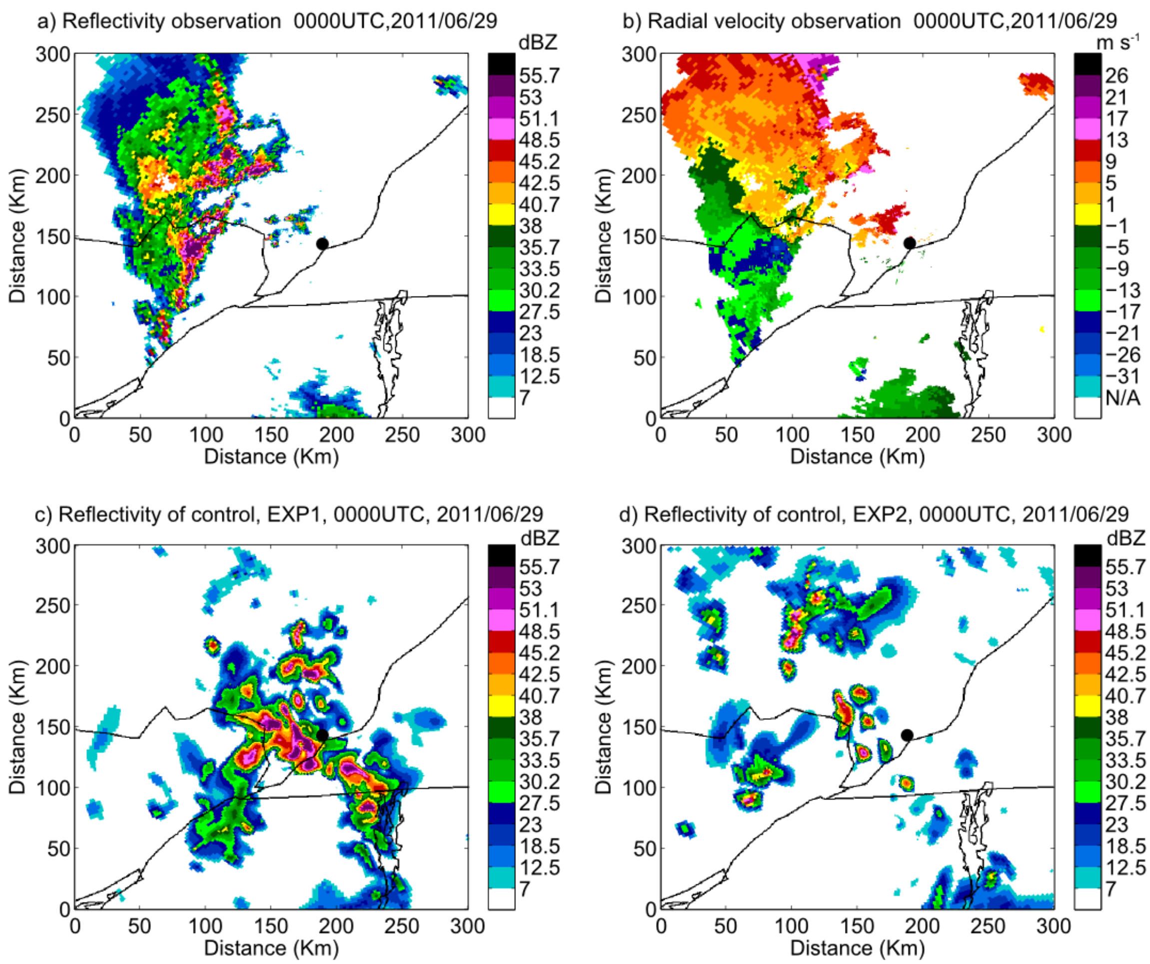

Fig. 4.6 The case of 29 June 2011. All figures are snapshots at 0000 UTC. a) Reflectivity observation at the 4th elevation angle (0.9 degree). b) Radial velocity observation at the 4th elevation angle. c) Model output of reflectivity for the control run of EXP1, interpolated to the 4th elevation angle. d) Model output of reflectivity for the control run of EXP2, interpolated to the 4th elevation angle. The black dots near the centers of figures denote radar location.

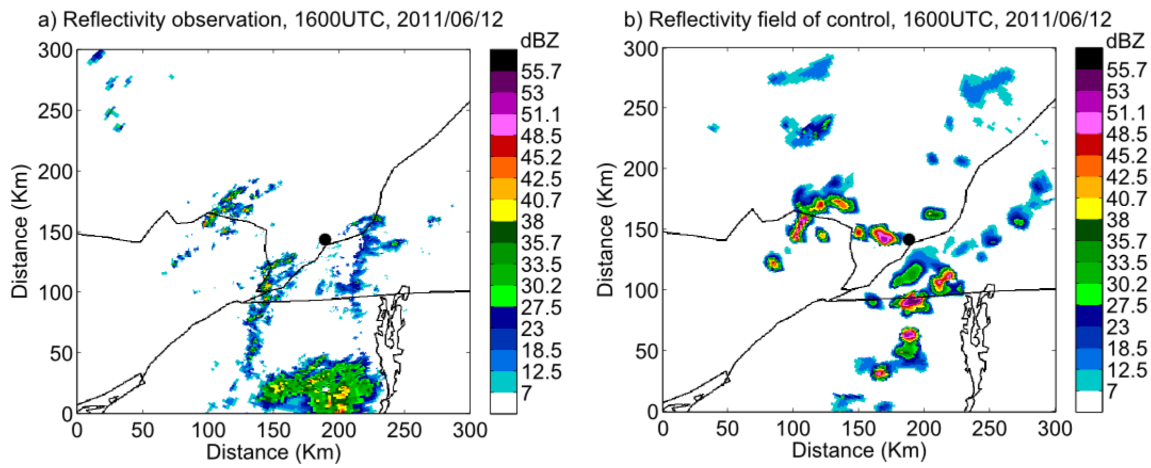

Fig. 4.7 The case on 12 June 2011 at 1600UTC. a) Reflectivity observations at the 4th elevation angle (0.9 degree). b) Model output of reflectivity for the control run, interpolated to the 4th elevation angle. The black dots near the centers of figures denote radar location.

The second case happened on 12 June 2011 where severe storms stroke the Montréal area in the afternoon, and delayed the "Grand Prix de Formule Un" car racing for more than two hours. As seen in the radar image (Fig. 4.7a), many storms near the center of the domain were small-scale, isolated and strong. Those storms moved from southwest to northeast and lasted for many hours. On the southern portion of the domain, a well organized stratiform weather system already existed and gradually decayed. HREnKF is performed from 1600 UTC to 1700 UTC. The short-term forecasts are from 1700 UTC to 1830 UTC. The reflectivity output of the control run (Fig. 4.7b) shows clear location errors at the initial time, which challenges the HREnKF system.

In the third case, around 2100 UTC on 23 June 2011, strong convections were observed to the south of the radar, and some light precipitation extends to the northeast of the domain (Fig. 4.8a). This mesoscale weather system developed and moved very slowly towards east-northeast. In this case study, HREnKF is performed from 2100 UTC to 2200 UTC, and short-term forecasts are from 2200 UTC to 2330 UTC. The reflectivity field of the control run (Fig. 4.8b) is similar to the observation in terms of the stratiform structure, but the location error is quite large.

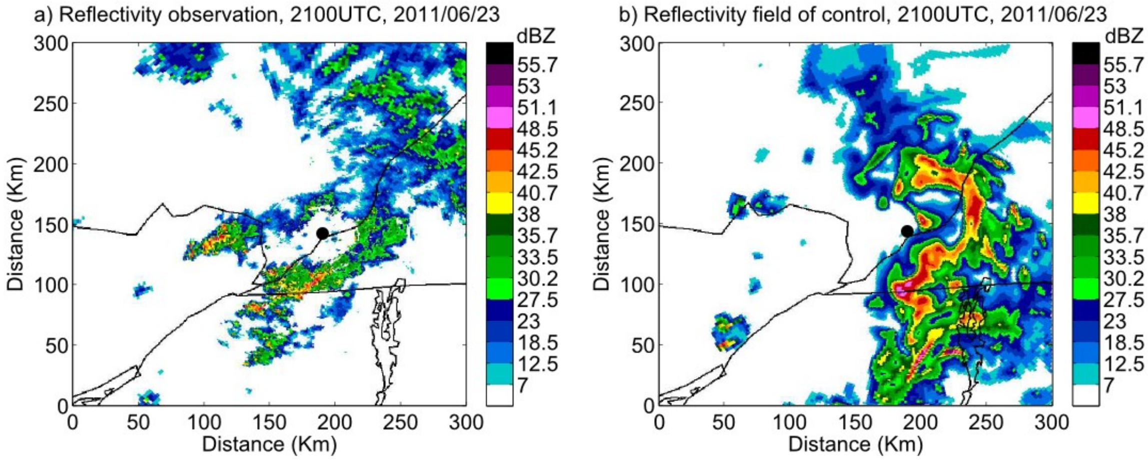

Fig. 4.8 As in Fig. 4.7 but for the case on 23 June 2011 at 2100 UTC.

c. Evaluation methodologies

The behavior of HREnKF and its impact on analysis and forecast are evaluated by several indicators. Firstly, indicators in observation-space are calculated during the cycling process of HREnKF in order to examine the ensemble spread and filter convergence. Secondly, the final analysis produced by HREnKF and the following short-term ensemble forecast are compared to the control run and the observations to demonstrate the improvement brought by HREnKF. We will call the 5-min forecast in cycling process 'background' in the following discussion, because they serve as the background for the analysis step. The 1.5-h forecast is referred to as 'short-term forecast'. In this way, we are able to literally differentiate the 5-min forecast in HREnKF and the 1.5-h forecast after HREnKF.

We now introduce observation-space diagnostic indicators for the HREnKF cycling process. By the end of each 5-min cycle, given the background and ensemble analysis calculated from equations (4.1) and (4.3) respectively, the observation-space ensemble means of background and analysis can be obtained by projecting variables from model-space to observation-space and averaging over all members. Then, two indicators are computed: root-mean-square (rms) error of ensemble mean background with respect to observations (referred to as 'background rms' hereafter), and rms error of ensemble mean analysis with respect to observations (referred to as 'analysis rms' hereafter). The computation of rms error is given by

$$rms = \sqrt{\frac{1}{M}\sum_{m=1...M}\left(o_m - \overline{\mathbf{HX}_m}\right)^2} \tag{4.9}$$

where M is the number of observations used for the current analysis step; o_m is the mth observation; $\mathbf{HX}_m$ is the model state in observation space for the mth observation, and its average is taken over all the ensemble members. When $\mathbf{X} = \mathbf{X}^f$, representing the background state vector, Eq. (4.9) calculates the background rms. When $\mathbf{X} = \mathbf{X}^a$, representing the analysis state vector, Eq. (4,9) calculates the analysis rms.

Based on the information of ensemble members and ensemble mean of background, the ensemble spread of background can be calculated as well. In order to be comparable to the background rms, the ensemble spread is computed also in observation-space as

$$spread = \sqrt{\frac{1}{M}\sum_{m=1...M}\left\{\frac{1}{N-1}\sum_{n=1...N}\left(\mathbf{HX}^f_{n,m} - \overline{\mathbf{HX}^f_m}\right)^2\right\}} \tag{4.10}$$

where M is the number of observations used for the current analysis step; N is the number of ensemble members; $\mathbf{HX}^f_{n,m}$ is the ensemble background of member n in observation space for the mth observation. Sufficient ensemble spread is a necessary condition of successful operation of EnKF. The ensemble spread is usually generated at the beginning of EnKF and should be maintained during the cycling process. For example, Dowell and Wicker (2009) discussed the use of additive noise for producing and maintaining ensemble spread for storm scale ensemble data assimilation. In our HREnKF, the ensemble spread is maintained by dividing ensemble members into subgroups (Houtekamer and Mitchell 1998). Two different approaches of obtaining initial ensemble members (see subsection 4.3a) will also be examined. Another possible method of keeping sufficient ensemble spread is inflation (e.g. Anderson 2007). In the results section of this article, we will show that ensemble spread is supposed to meet the requirement that (spread^2+observation error variance) is greater than or comparable to (background rms)^2.

Another diagnostic indicator for the HREnKF cycling process is proposed here to test the convergence between background and truth implying filter convergence. In our real data study, since the truth is unknown, observations which are closely related to the truth are considered as references to judge the convergence. For the purpose of measuring the difference between background and observations, 'observation-pass-ratio' is defined as the ratio of the number of observations which pass the background check to the total observation number available for each cycling step. As explained in subsection 4.2a, the background check aims at excluding the observations greatly differing from the background (Eq. 4.5). Accordingly, a larger observation-pass-ratio implies model states being closer to observations, since larger proportion of observations are able to pass the background check. A gradually growing observation-pass-ratio suggests filter convergence. Note that a greater observation-pass-ratio does not necessarily suggest that more data are assimilated because the absolute number of assimilated observations depends also on the total observation number before background check.

Besides the above indicators exploring the performance of HREnKF, two other scores are used for verifying the accuracy of final analysis and short-term ensemble forecast, given observations as reference. The first score is the 'bias' defined as the spatial average of the differences between observations and ensemble forecast or analysis (zero-time lead forecast) at each radar elevation angle for each ensemble member. A score closer to zero implies better quality of the analysis or the forecast. The score is given by

$$bias_{l,n} = \frac{1}{M'} \sum_{m=1...M'} \left(o_m - \mathbf{H}\mathbf{X}^f_{n,m} \right) \tag{4.11}$$

where l means the lth elevation angle; n denotes the nth member; M' is the number of observations at the lth elevation angle. The second score is the 'rms' of ensemble forecast with respect to observations at each elevation angle for each member. If the forecast is closer to the observation, the rms is expected to be smaller. The rms is calculated by

$$rms_{l,n} = \sqrt{\frac{1}{M'} \sum_{m=1...M'} \left(o_m - \mathbf{H}\mathbf{X}^f_{n,m} \right)^2} \tag{4.12}$$

where $rms_{l,n}$ is the forecast rms at the lth elevation angle for ensemble member n. It is important to realize that this score is different from Eq. (4.9) which calculates the rms of the ensemble mean. Given the bias and rms for 80 ensemble members, the ensemble mean and ensemble standard deviation of the 'bias' and 'rms' are calculated from the scores of each member.

For the control run, similar scores can be calculated from Eqs. (4.11) and (4.12), where $\mathbf{X}^f$ means the model state vector of the control run that has only one member.

4.4 Results

a. Results of the case on 29 June 2011

The results of two experiments for the first case study will be shown in this section. The first experiment (CASE1_EXP1 hereafter) and the second experiment (CASE1_EXP2 hereafter) take the schemes of EXP1 and EXP2 respectively as defined in subsection 4.3a.

The first results we present are the indicators of rms errors and ensemble spread over the HREnKF cycling period, which can be used to examine the sufficiency of ensemble spread. The ensemble spread and rms errors are presented in V_r observation space, including only the observations that pass the background check. In CASE1_EXP1 (Fig. 4.9a), the ensemble spread is smaller than the background rms for all cycles, thus puts the HREnKF in danger of underestimation of the background uncertainty. This problem is due to the fact that the initial ensemble spread of CASE1_EXP1 is decided by the set of random perturbations applied in the beginning of HREnKF, whose variances are not large enough. Nevertheless, we do not want to amplify the initial perturbations because, it could perturb too severely the model dynamical and physical balance. Therefore, the relatively small amplitude of random perturbations results in the insufficiency of ensemble spread. Another important reason for the small ensemble spread in CASE1_EXP1 is its fixed lateral boundary conditions, which gradually influence the inner domain through the model integration and reduce the ensemble spread near the boundaries. Similar discussions about rms errors and ensemble spread can also be found in Aksoy et al. (2009, 2010) and Dowell (2011). Our results focus on the improvement of sufficiency of ensemble spread brought by implementation of the regional EnKF.

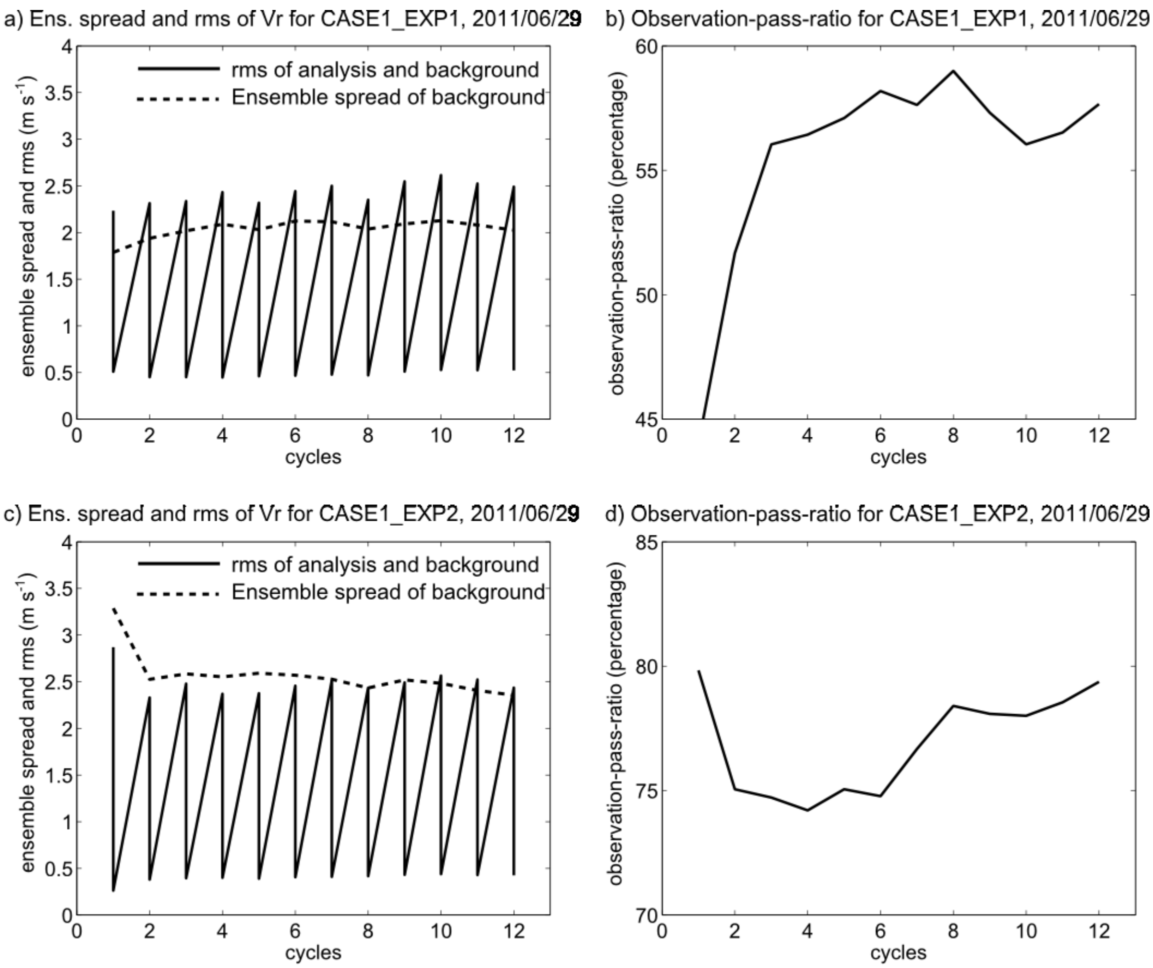

Fig. 4.9 Results of cycling process for the case on 29 June 2011. Each cycle takes five minutes. a) and b): CASE1_EXP1. c) and d): CASE1_EXP2. a) and c): ensemble spread in observation space (V_r) (dashed line), background rms of V_r (12 upper points on the solid line) and analysis rms of V_r (12 lower points on the solid line) during the cycling process. b) and d): observation-pass-ratio.

Different from CASE1_EXP1, the initial ensemble members in CASE1_EXP2 are derived from the REnKF, which guarantees large ensemble spread (Fig. 4.9c) as well as realistic balanced model fields. Moreover, since each member has its own lateral boundary conditions, the ensemble spread near the boundary does not shrink as in CASE1_EXP1. Quantitatively speaking, the ensemble spread for CASE1_EXP2 is around 2.5 m s^{-1} (Fig. 4.9c), while the ensemble spread for CASE1_EXP1 is no more than 2 m s^{-1} (Fig. 4.9a). Correspondingly, the total spread squared (ensemble spread squared + observation error variance) is (2.5^2+1^2) for CASE1_EXP2 and (2^2+1^2) for CASE1_EXP1. Given the background rms staying around 2.3 - 2.5 m s^{-1} for both CASE1_EXP1 and CASE1_EXP2, by applying the criterion for deciding the ensemble spread sufficiency as described in subsection 4.3c, one can tell that the ensemble spread is sufficient in CASE1_EXP2 but insufficient in CASE1_EXP1.

The second set of results we now discuss are the observation-pass-ratios that indicate the convergence of background to observations during HREnKF cycling process. The observation-pass-ratio for CASE1_EXP2 increases from about 74% to almost 80% after the 4^{th} cycle (Fig. 4.9d), while the ratio for CASE1_EXP1 generally remains around 57% after cycle 3 (Fig. 4.9b). This infers first that the background gradually converges to observations during the cycling process in CASE1_EXP2, and second, the HREnKF in CASE1_EXP2 incorporates a larger proportion of observations than CASE1_EXP1 because of its larger ensemble spread (Fig. 4.9c). Although the increasing observation-pass-ratio after the 4^{th} cycle in CASE1_EXP2 suggests filter convergence, it drops from 80% to 74% in the first 3 cycles. This is because the observation-pass-ratio decreases when ensemble mean deviates from observations, or ensemble spread reduces. The ensemble spread is large at the beginning (before any assimilation proceeds), and therefore allows many observations to pass the background check. After the first assimilation step, however, all ensemble members are constrained by observations, and the resulting smaller ensemble spread leads to the reduction of observation-pass-ratio. For the following cycles, although the ensemble spread reduces (see Fig. 4.9c), the ensemble mean becomes closer to the observations. Consequently, fewer observations are rejected and the observation-pass-ratio increases.

After showing diagnostic indicators exhibiting the quality of the HREnKF cycling process, we now verify the impact of radial wind assimilation on analysis and short-term forecast by comparing them to the control run. Note that control runs for CASE1_EXP1 and CASE1_EXP2 are different (see subsection 4.3a).

The third results we show are scores of ‘bias’, ‘rms’, their ensemble mean and ensemble standard deviation computed at analysis time 0100 UTC on different radar elevation angles (Figs. 4.10a and 4.11a), which are similar to results presented by Aksoy et al. (2010). Although ‘radar beam elevation index’ is used as y-axis in the figures, it is still able to generally describe different altitudes in the atmosphere. While both 'bias' and 'rms' describe the accuracy of analysis and forecast, 'rms' is a more direct measure of errors. As shown in Eq. (4.12), 'rms' does not allow errors to cancel each other as the 'bias' does in Eq. (4.11). On the other hand, 'bias' is helpful to detect whether errors happens in small scale or is caused by the large-scale flow. When the radial velocity of analysis has significant errors, small bias is still possible when the inaccuracy is caused by large-scale flow. This is because large-scale errors (the entire wind field is overestimated/underestimated to the same direction at large scale) have opposite signs on opposite sides of the radar.

Figures 4.10a and 4.11a show the improvement of the analysis over the control run for both experiments, with observations used as reference. Note that all evaluations against radar data are done without data thinning. The total number of data used for verifications as a function of elevation angles appears on the right hand side of each panel. For CASE1_EXP1 at analysis time 0100 UTC (Fig. 4.10a), the red curves being closer to the zero lines than the blue curves indicates that the analysis has smaller bias and rms than the control run on almost all elevation angles. Similar results can also be observed in Fig. 4.11a for CASE1_EXP2. In addition, the entire error bars representing ensemble standard deviations in Figs. 4.10a and 4.11a are mostly closer to the zero line than the blue curve, which demonstrates that the improvement is not limited to the ensemble mean, but for most ensemble members.

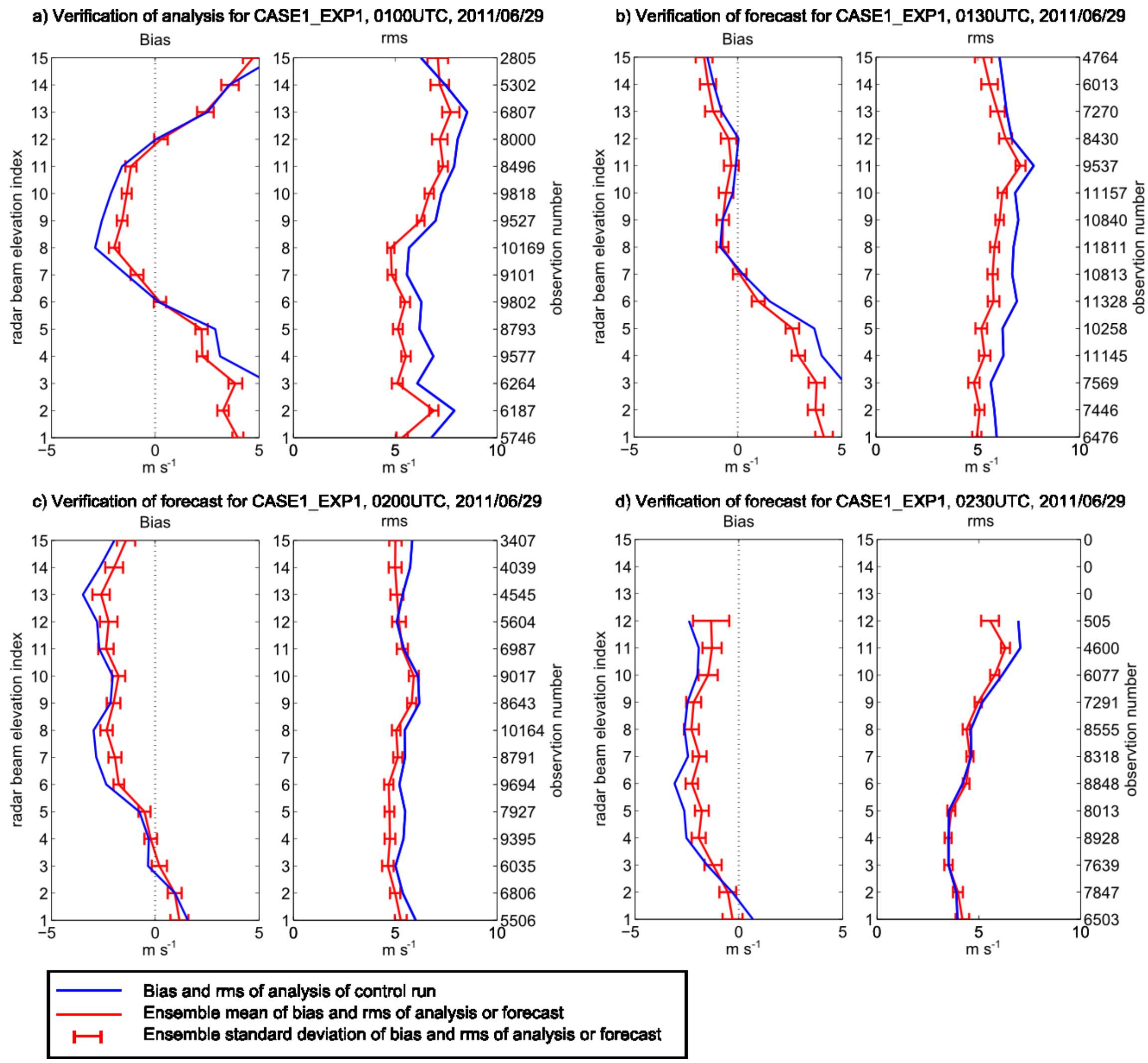

Fig. 4.10 Verification scores (bias and rms) of analysis and short-term ensemble forecast against the control run at different time periods for experiment CASE1_EXP1. Radar elevation indexes on y-axis from 1 to 15 correspond to radar beam elevation angle: 0.3, 0.5, 0.7, 0.9, 1.1, 1.4, 1.7, 2.0, 2.4, 2.9, 3.4, 4.1, 4.8, 5.6, 6.6 deg. Total number of radar data used (without data thinning) at each elevation angle appears on the right of each panel.

The fourth results for this case study include the scores of bias and rms in short-term forecasts. The curves in Figs. 4.10b, 4.10c, and 4.10d show that the bias and rms scores of short-term forecast gradually approach the scores of the control run over the forecast period in CASE1_EXP1. At time 0230 UTC, 90 min after initiation of the ensemble forecast, the rms curves of forecast and control run are almost identical especially in the lower elevations, but the bias of forecast is still generally smaller than control run. This means the impact of HREnKF still exists in forecast after 90-min model integration. Different from CASE1_EXP1, the accuracy of analysis in observation space in CASE1_EXP2 does not guarantee a precise forecast. The scores for CASE1_EXP2 illustrate that at time 0130 UTC, just 30 min after the start of short-term forecast, it is already difficult to tell whether the forecast or the control run is better, especially when the error bars are taken into consideration. In other words, the impact of assimilating radial velocities in CASE1_EXP2 does not last as long as in CASE1_EXP1.

Given the above results of short-term forecast, one can tell that the HREnKF has much more influence on the forecast in CASE1_EXP1 than in CASE1_EXP2. This can be explained by the role of REnKF which is to provide more precise mesoscale initial ensemble members for CASE1_EXP2. Because the entire system is a double step EnKF procedure, we expect to have a more precise analysis after REnKF assimilates conventional observations, which provide the initial ensemble members for the HREnKF. REnKF is expected to correct large-scale flows, and directly update more model variables other than only wind components. Consequently, the improved large-scale circulation, which strongly affects the prediction in this case study, removes many errors at the beginning of HREnKF in CASE1_EXP2. The evidence can be found in Fig. 4.6 as the control run at the initial time in EXP2 has much less errors than in EXP1. After HREnKF cycling process starts in CASE1_EXP2, errors are further corrected by radial velocity assimilation. However, most corrections happen at small-scales because large-scale errors are already reduced by the use of REnKF. Therefore when large-scale errors dominate the short-term forecast, the impact of HREnKF quickly diminishes in CASE1_EXP2 (Fig. 4.11). The effect of REnKF can be verified by comparing the blue curves of control runs in Figs. 4.10 and 4.11. For example, at 0130 UTC, the rms of control run in CASE1_EXP1 (Fig. 4.10b) is around 6 m s^{-1}, while the control run in CASE1_EXP2 (Fig. 4.11b) has smaller rms values around 5 m s^{-1}. Hence the relatively limited and short-lived impact of HREnKF on short-term forecast in CASE1_EXP2 is more likely due to the accuracy of its control run, rather than a defect of HREnKF.

The last results discuss the ensemble standard deviation of bias and rms in Figs. 4.10 and 4.11. By comparing the red error bars in Fig. 4.10 and 4.11 at the same time period (e.g. comparing Figs. 4.10b and 4.11b), we find that the ensemble standard deviations of bias and rms in CASE1_EXP2 are generally larger than those in CASE1_EXP1, which is consistent with the previous result of ensemble spread being larger in CASE1_EXP2. The ensemble standard deviation also changes with observation numbers. For example, at 0230 UTC in CASE1_EXP2 (Fig. 4.11d), the ensemble standard deviation of bias on the 12th elevation angle is much greater than those on lower elevation angles. This results from a poor sampling; i.e. having only 505 observations at that elevation.

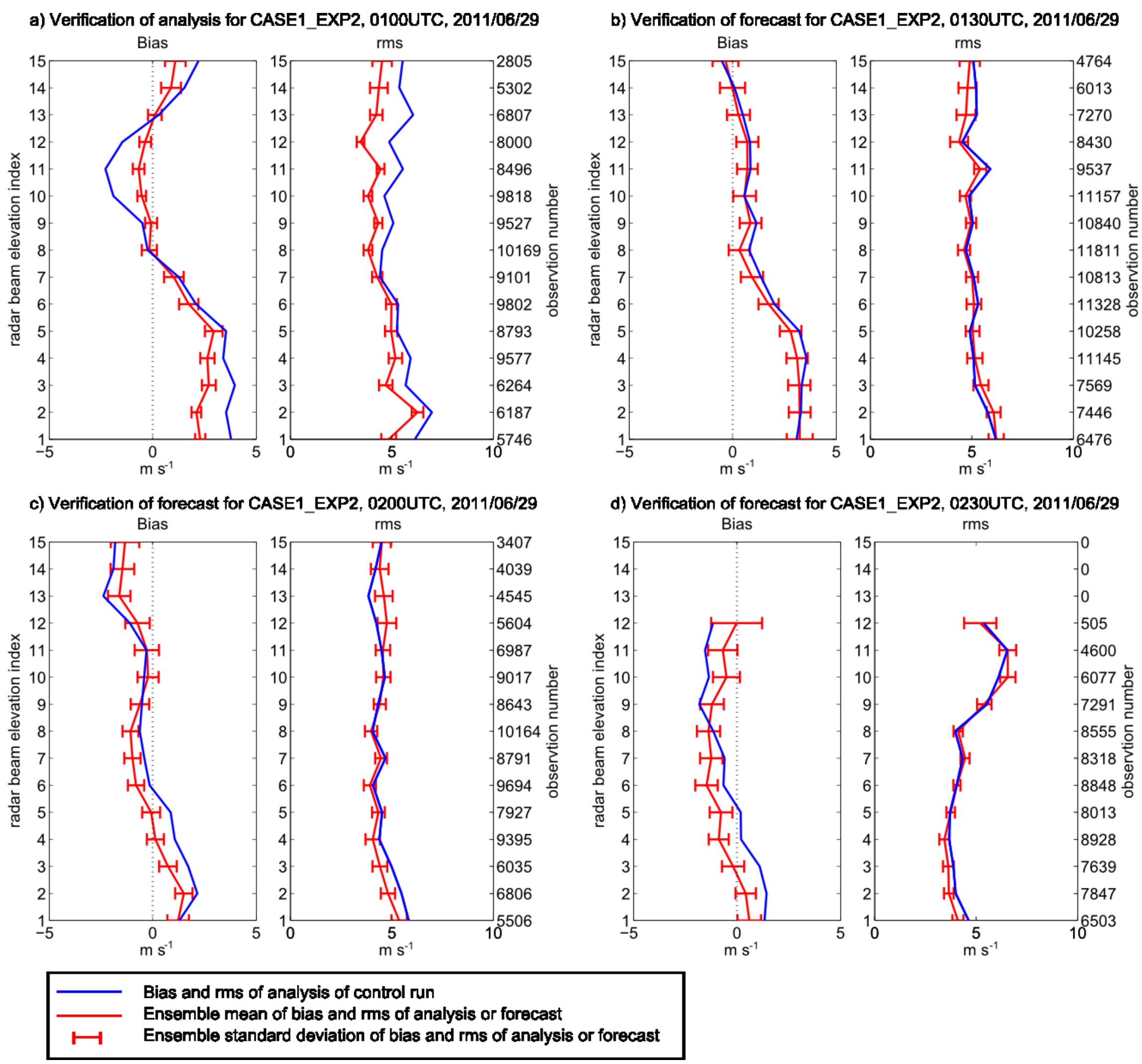

Fig. 4.11 As in Fig. 4.10 but for experiment CASE1_EXP2.

The difference between results of CASE1_EXP1 and CASE1_EXP2 suggests that applying REnKF before HREnKF has many benefits, such as providing the sufficient ensemble spread, and correcting larger scale circulation. Accordingly, the following two case studies will follow only the experimental procedure of CASE1_EXP2.

b. Results of the case on 12 June 2011

This case study is named CASE2 hereafter. Note that CASE2 allows REnKF to provide the initial ensemble members, and ensemble boundary conditions for the 1-km model used in HREnKF. The ensemble spread and rms errors of analysis and background during the cycling process are shown in Fig. 4.12a, where no severe ensemble spread insufficiency appears. The observation-pass-ratios plotted in Fig. 4.12b prove that larger proportion of observations pass the background check as more cycles are involved, indicating that background fields tend to gradually converge to observations.

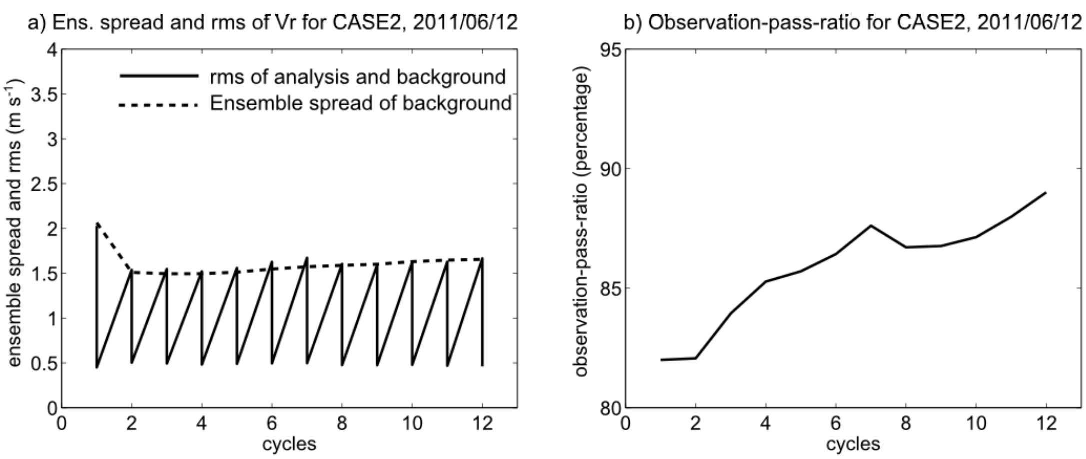

Fig. 4.12 Results of cycling process for CASE2 on 12 June 2011. Each cycle takes five minutes. a) ensemble spread in observation space (V_r) (dashed line), background rms of V_r (12 upper points on the solid line) and analysis rms of V_r (12 lower points on the solid line) during the cycling process. b) observation-pass-ratio.

Fig. 4.13 shows the one-step increments (analysis minus forecast) of V-component of the wind and humidity in the third cycling step at 1615 UTC. As directly involved in the observation operator (Eq. 4.6), the V-component is partly observed by the radar, and thus can be directly updated by assimilating radial velocities. The maximum change of the V-component can reach more than 2.1 m s^{-1} (Fig. 4.13a). On the other hand, the humidity field does not appear in the observation operator equation, and therefore requires cross-correlation between errors of humidity and observed variables (e.g. U, V components) to be updated (Snyder and Zhang 2003). The increment of humidity is up to 0.5 g Kg^{-1} at some locations in Fig. 4.13b (e.g. to the southwest of the radar), a value big enough to trigger convection under certain conditions (evidence of this in a parameterized convection context is given in Fillion and Bélair 2004).

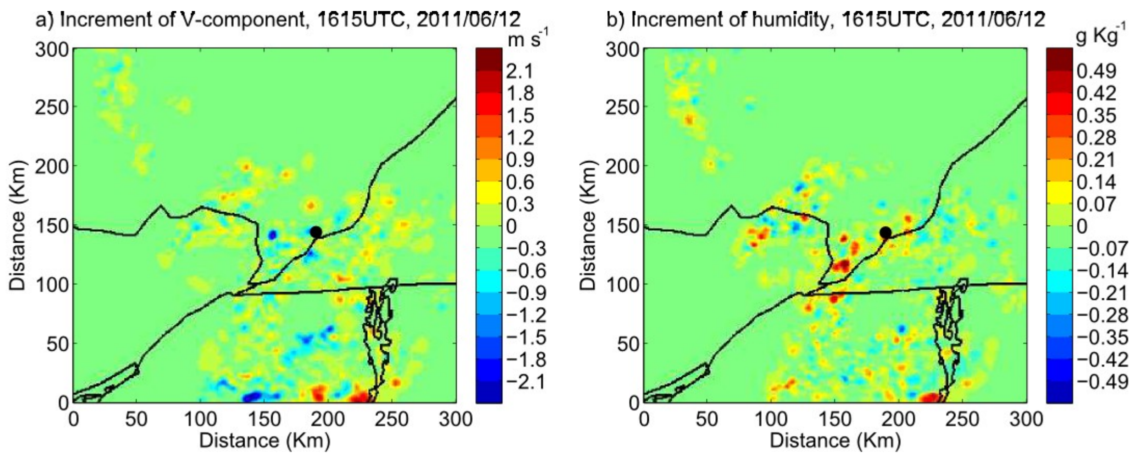

Fig. 4.13 The analysis increments (difference between ensemble mean background and ensemble mean analysis) of V-component of wind and specific humidity close to the surface (around 800hPa), for the third cycle at 1615 UTC, for CASE2 on 12 June 2011. The black dots near the centers of figures denote radar location.

In addition, although the unobserved variables can be updated by HREnKF, we still need to verify that the entire model state approaches the truth. Despite the truth being unknown, reflectivity observations provided by the same radar used in the assimilation system can reasonably be considered as a reference for examining the impact of radial velocity assimilation on precipitation. As an example, shown in Fig. 4.14 are snapshots of reflectivity fields of the 8th analysis member and the control run together with the reflectivity observations at 1700 UTC when all cycles are completed. We choose to show single ensemble members instead of ensemble mean because the ensemble mean could smooth the field and wipe out small-scale information. Figure 4.14d shows at each pixel, the percentage of ensemble members producing precipitation stronger than 30 dBZ with respect to the total 80 ensemble members. For example, 20% in Fig. 4.14d indicates 16 out of 80 members produce precipitation stronger than 30 dBZ. In general, given reflectivity observations as reference, Figs. 4.14c and 4.14d exhibit relatively more accurate storm locations near the center ('west-east distance' between 150 km and 200 km, and 'south-north distance' between 100 km and 150 km) and in the north of the domain ('south-north distance' greater than 150 km), compared to the control run (Fig. 4.14b). It infers that the HREnKF is able to correct the storm location error to some extent. However, some precipitation in the southeastern area is observed by the radar, but is missed by both the analysis members and the control run. Additionally, some spurious storms, around which radial velocity observations are unavailable, are difficult to be eliminated. Assimilating reflectivity data, especially the non-precipitation observations will be helpful for removing false alarms in a future development of our HREnKF system.

To have a deeper view, the Convective Available Potential Energy (CAPE) fields for the control run and the 8^{th} member of ensemble analysis are investigated (Fig. 4.15). The CAPE values are calculated based on the model levels within the lowest 50hPa. CAPE describes the convective instability present in model and we stress that its computation involves *unobserved* variables. Near the center of the domain and to the east of the radar ('west-east distance' around 220 km, and 'south-north distance' around 150 km), the CAPE values in #8 analysis are much greater than in the control run, which demonstrates that the assimilation of radial velocity greatly increases the instability. In the west of domain, the CAPE values for #8 analysis are smaller than the control run. Although no data are available in this region (see Fig. 4.14a), the CAPE are probably reduced by the perturbations or by assimilating the nearby observations which gradually modify the environment through the twelve assimilation cycles. In the southeast part of the domain, both analysis and control run give small CAPE values, even though plenty of observations are available over that region. One plausible reason explaining this fact is that the cross-correlation between wind components and other variables is too weak, and the background is too far from the reality.

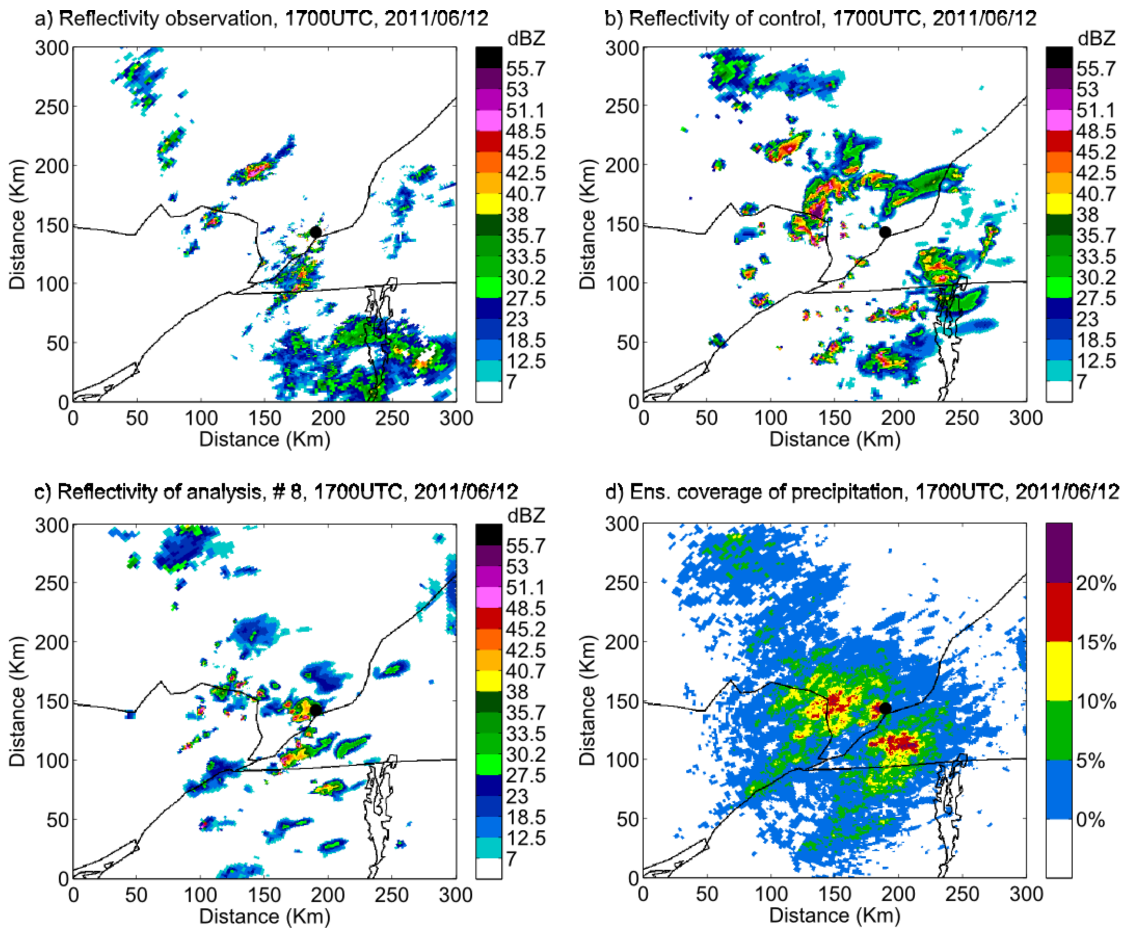

Fig. 4.14 Reflectivity fields of observations, control run and final analysis at 1700 UTC, 12 June 2011. a) reflectivity observations at the 4^{th} elevation angle (0.9 degree). b) reflectivity output of the control run, interpolated to the 4^{th} elevation angle. c) reflectivity output of the 8^{th} analysis member, interpolated to the 4^{th} elevation angle. d) the percentage of analysis members producing reflectivity higher than 30dBZ, out of the total analysis members, at the 4^{th} elevation angle. The black dots near the centers of figures denote radar location.

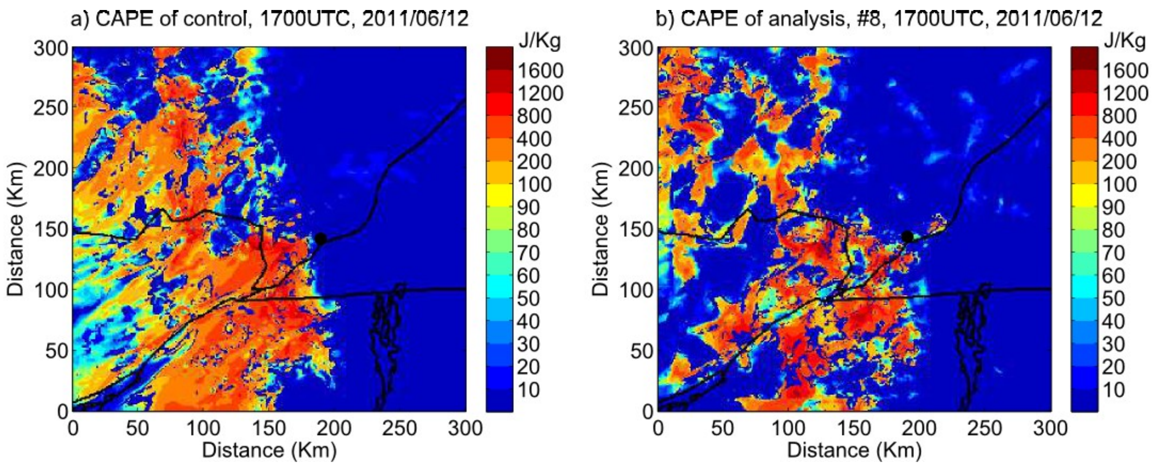

Fig. 4.15 CASE2 CAPE field near the surface (lowest 50hPa) at 1700 UTC for: (a) the control, (b) the 8th analysis member. The black dots near the centers of figures denote radar location.

Lastly, the effect of HREnKF on analysis and short-term forecast is shown by scores of radial wind bias and rms in Fig. 4.16. At 1700 UTC, the values of rms for analyses are generally much smaller than those for the control run (right panel of Fig. 4.16a), and such patterns last until 1830 UTC for 90 min (right panels of Figs. 4.16b, 4.16c, and 4.16d) during short-term forecasts. These forecast results are consistent with many other studies about EnKF systems working with simulated radar data (Tong and Xue 2005) and real radar data (Aksoy et al. 2009, 2010; Dowell 2011). Although the REnKF is applied on both CASE2 and CASE1_EXP2, the superiority of short-term forecasts over the control run is more evident in CASE2 than in CASE1_EXP2 (Fig. 4.11). As opposed to the squall line precipitation structure in CASE1_EXP2, convections in CASE2 are localized at small scale, and are less influenced by large-scale flow. Consequently, most of the correction made on small scale errors is done by HREnKF itself rather than from the REnKF. In brief, HREnKF plays a more important role in CASE2 than in CASE1_EXP2 due to the precipitation happening at small scales in CASE2.

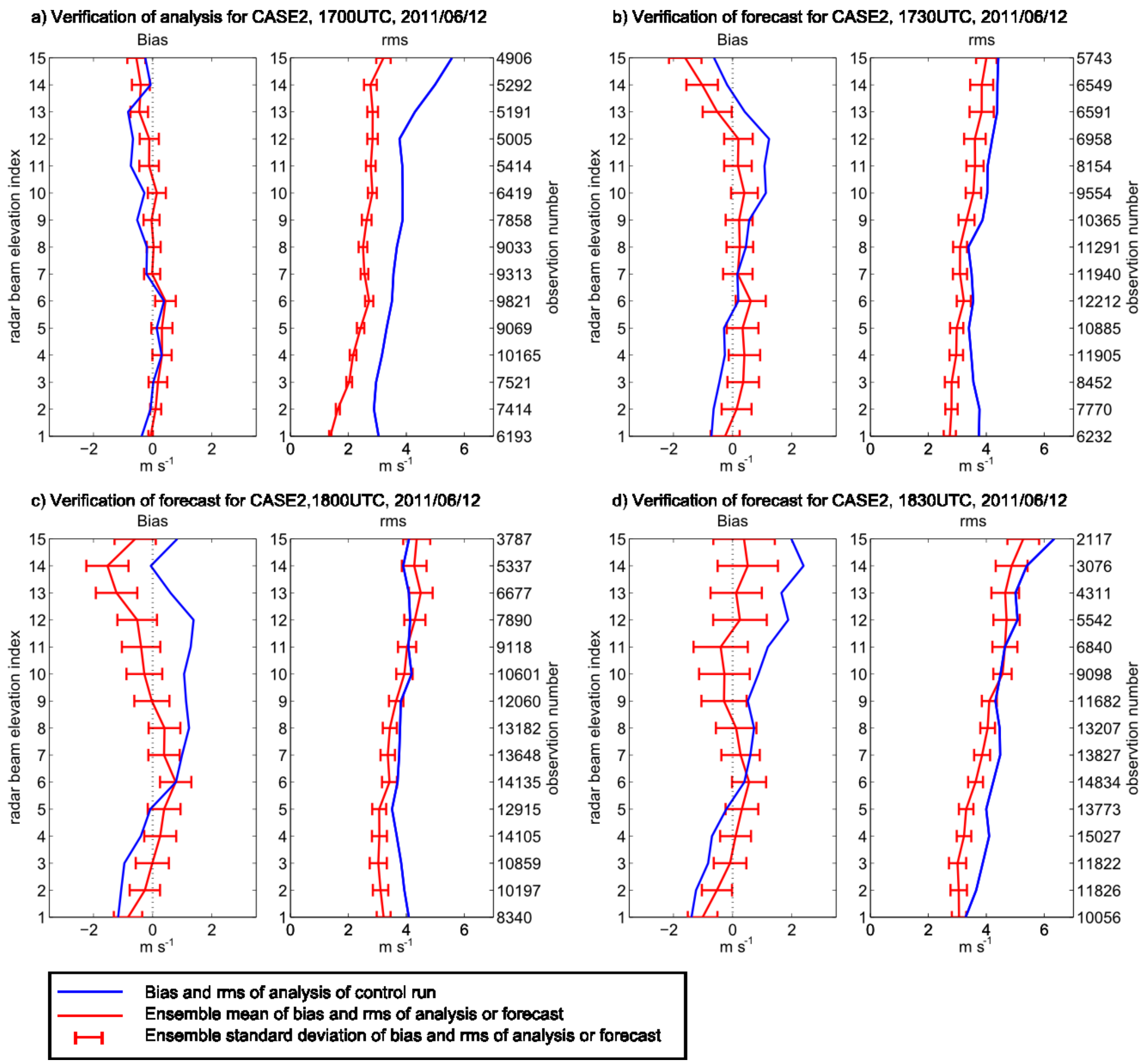

Fig. 4.16 As in Fig. 4.10 but for experiment CASE2 on 12 June 2011.

c. Results of the case on 23 June 2011

This case study is referred to as CASE3 in the following discussion. The analysis performance indicators for CASE3 shown in Fig. 4.17 exhibit large ensemble spread and increasing observation-pass-ratio, which are similar to the previous two cases, except for the growing ensemble spread during the cycling process (Fig. 4.17a). In fact, while the ensemble spread slightly increases, so does the observation-pass-ratio. It is difficult to determine whether the rise of observation-pass-ratio is caused by the convergence between background and observations as discussed in subsection 4.4a, or by the slightly growing ensemble spread that gradually allows larger portion of observations to pass the background check. We noted however that for CASE1_EXP2, the ensemble spread decreases when observation-pass-ratio increases (Figs. 4.9c and 4.9d), which suggests that the better agreement between background and observations is the only reason for the rising of observation-pass-ratio. Therefore, CASE1_EXP2 is more convincing than CASE3 in terms of convergence of model states to observations. On the other hand, although the ensemble spread rises slightly here, the analysis rms shows a tendency of decrease in CASE3 (Fig. 4.17a), implying that the ensemble mean analysis contains smaller errors with respect to observations as more cycles are conducted.

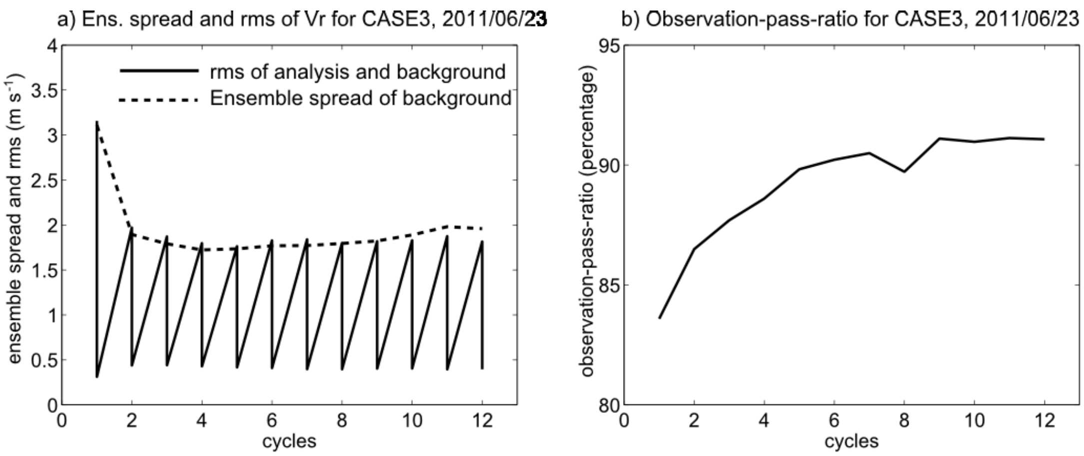

Fig. 4.17 As in Fig. 4.12 but for experiment CASE3 on 23 June 2011.

The verification scores of bias in Fig. 4.18a show that at time 2200 UTC, the improvement of analysis over the control run is insignificant. The control run is even better in terms of bias, probably because it happens to be very accurate at that time. After the forecast starts, however, the control run scores begins to deviate from the zero line at the lowest eight elevation angles, while the bias values of ensemble forecast remain smaller (Fig. 4.18b). This situation holds until 2330 UTC. This tells that even though the impact of HREnKF on analysis is not clear in observation space, the forecast is still under its influence because the entire model state is improved and able to produce more accurate prediction.

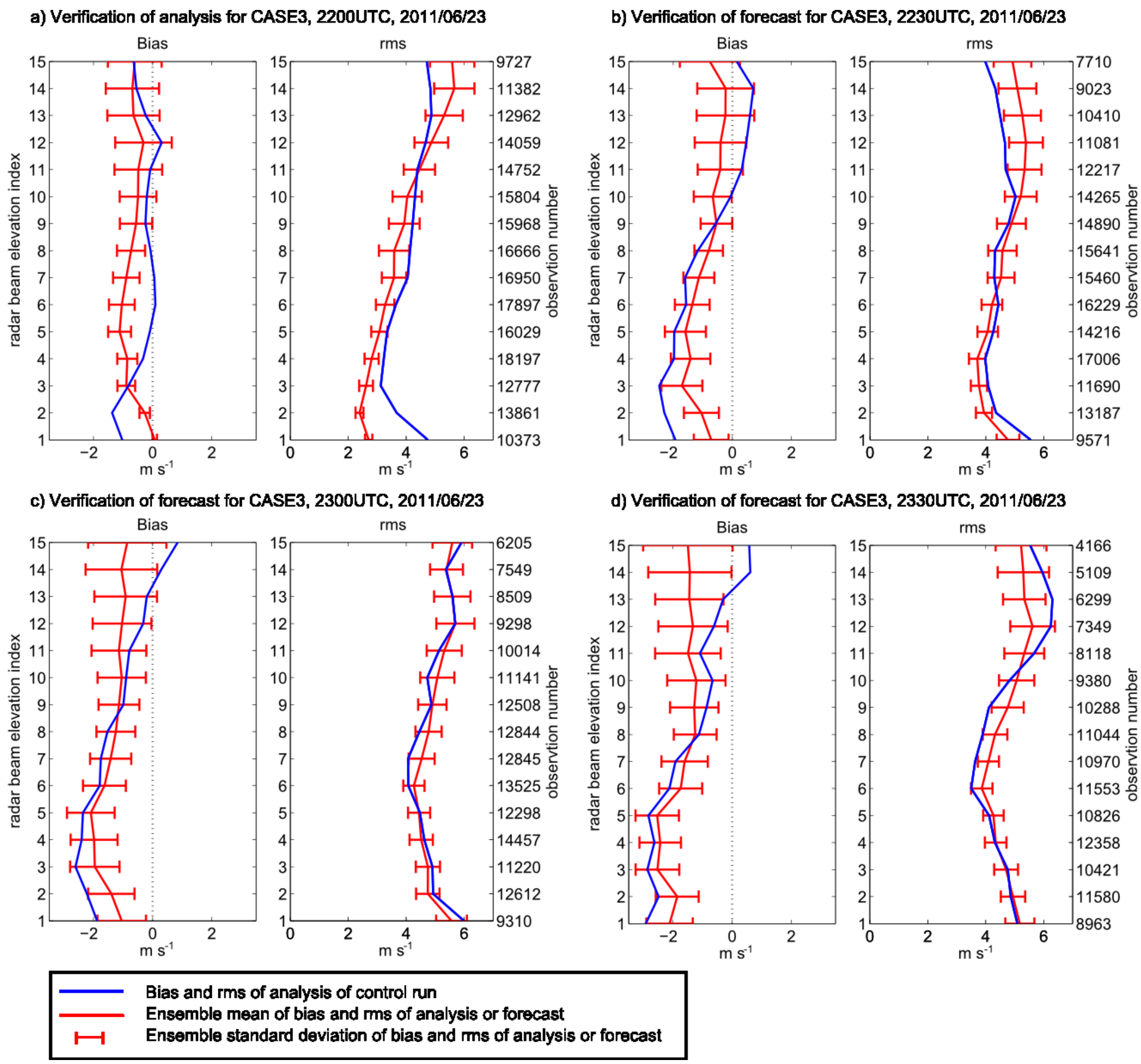

Fig. 4.18 As in Fig. 4.10 but for experiment CASE3 on June 23, 2011.

The verification scores of rms in Fig. 4.18 indicate that the analyses are better than control run below elevation angle #11 at 2200 UTC. Similarly, the superiority of forecasts can be seen below angle #7 at 2230 UTC, and is also evident below angle #5 at 2300 UTC. At 2330 UTC, the end of ensemble forecast, the impact of HREnKF on forecast vanishes. Therefore, for this stratiform precipitation case, the improvement on forecasts lasts longer at lower elevation angles than at higher elevation angles.

4.5 Summary and discussion

This study introduces a High Resolution Ensemble Kalman Filter (HREnKF) system designed in particular for convective-scale radar data assimilation. The key features of HREnKF include: a set of 80 ensemble members divided into four subgroups; three-dimensional error correlation localization; sequential assimilation; background check of observations. The observations assimilated by the HREnKF in current experiments are radial velocities from McGill Radar Observatory and covering the Montréal region. Radial velocity observations are incorporated by HREnKF every 5 min cycle for twelve cycles during the 1-h assimilation process, by the end of which, final analyses are produced and a 1.5-h 80-member ensemble forecast is launched.

Three summer cases in 2011 are studied including the first case with squall line precipitation structure on 29 June 2011; the second one with isolated strong small-scale storms on 12 June 2011; and the third case of widely distributed stratiform on 23 June 2011. Studies of all three cases involve the Canadian Regional EnKF (REnKF) for generating the initial ensemble members and ensemble lateral boundary conditions for HREnKF. In addition, another experiment is done for the first case study, where a deterministic forecast provides initial guess and fixed lateral boundary conditions for the experiment.

The indicators of ensemble spread, analysis rms and background rms exhibited sufficient ensemble spread during the cycling process in all three cases, as long as REnKF are implemented to provide ensemble initial and lateral boundary conditions. In contrast, if a deterministic forecast is used as initial guess for HREnKF and if lateral boundary conditions are the same for all ensemble members (as in the first experiment of the first case), this results in insufficient ensemble spread and underestimation of forecast uncertainty.

We also systematically measured the difference between background and observations by the *observation-pass-ratio* defined as the ratio of the number of observations passing the background check to the total observation number. As the cycling procedure proceeds, the portion of observations kept by the background check gradually increases for all three cases. Given that the ensemble spread reduces (the first case) or not significantly increases (the second and the third cases), one can conclude that the model state in HREnKF gradually converges to the observations during the cycling process.

Besides the observed wind components, unobserved variables are also updated by the HREnKF through the error cross-correlation between observed and unobserved variables. For example, the results of the second case study showed notable increment of the humidity field in one cycle although humidity is not observed by the radar. Moreover, images of reflectivity and CAPE for the second case show that the model convective instability in a manner is consistent with radar observations. In the areas devoid of observations, although the spurious storms are different to be directed removed, the surrounding data are able to modify the environment to some extent.

After the cycling process completes, the analysis and the short-term forecast are still under the influence of radial velocity assimilation. The first case showed that for the weather system controlled by large-scale flows, error corrections by the REnKF has more effect than HREnKF. The second case demonstrated that when localized convection happens, the HREnKF accounts for most of the corrections and is able to improve the location of the storms in the resulting analyses. In addition, the ensemble forecast is much better than the control run with respect to radial velocity observations, and lasts up to 90 min after forecast initiation. The third case showed that for this wide spread and stationary stratiform case, the improvement lasts longer at lower elevation angles than at higher elevation angles.

Some limitations exist in our current experiments. Firstly, although HREnKF improves short-term forecasts, the improvement unfortunately does not survive for more than 90 min. This can be explained by the growing errors of ensemble forecasts due to the use of an imperfect model and the invasion of inaccurate lateral boundary conditions. Secondly, observations of radial velocity only provide information of one wind component, and therefore have difficulty in efficiently improving 3-D wind field and unobserved variables. The update of unobserved fields relies on the cross-correlation between errors of observed and unobserved variables, which could occasionally be too weak to accomplish all necessary corrections. For example, results of the second case show that the assimilation of radial velocity in the southeast of the domain is unable to generate CAPE values large enough to trigger convections. Thirdly, the homogenous model error applied at every cycle and the fixed localization algorithm are not most favorable for the

HREnKF. In fact, model error is not homogenous but difficult to estimate. The localization algorithm should be made consistent with the spatial correlation distance of background errors, which is shorter in precipitation area and longer otherwise.

For a consistent incremental development of our HREnKF analysis system, we deliberately limited our study to the assimilation of radial velocity data. As a further step towards full exploitation of available radar observations, reflectivity data will be considered in addition to radial velocities in the near future. Actually, including reflectivity data will probably contribute much more to the analysis and forecast in terms of correction of storm location and intensity, since it directly relates to the microphysical variables. Hence the next step of HREnKF implementation is to assimilate in addition reflectivity observations and examine its impacts.

Chapter 5

Adaptive Radar Observation for Better Ensemble-Based Data Analysis

The previous chapter shows that although Ensemble Kalman Filter can improve the short-term forecast, the improvement cannot last for more than 2 hours. In order to enhance this improvement, this chapter will propose an adaptive radar observation method to improve the unobserved vertical velocity by assimilating only radial velocity in to a high resolution model. This idealized adaptive radar observation method works under the condition that the phased-array technique or fast scanning mechanical radar is available for adaptive data collection.

This chapter is based on the following article.

Chang, W. and I. Zawadzki, 2014: Adaptive Radar Observation for Better Ensemble-based Data Analysis. Monthly Weather Review. Submitted.

Chapter 5

Adaptive Radar Observation for

Better Ensemble-Based Data Analysis

Abstract

An analysis produced from mesoscale radar data assimilation usually has a short-lived improvement on numerical forecast (maximum 2~3 hours) because assimilating only the radar data of reflectivity and radial velocity leads to difficulty in correcting other important and unobserved model variables. The degree to which unobserved variables can be improved depends on background error statistics, including the cross-covariance between errors of observed and unobserved variables, which varies in space. The method of adaptive radar observation is introduced for modern radar employing phased-array technique to focus on the areas where the greatest potential improvement is possible for the important unobserved variables.

In this study, radial velocity and vertical motion are considered to be the observed and unobserved state variables respectively. The adaptive observation strategy is decided according to background error statistics calculated from ensemble forecasts. Observations simulated under different strategies are assimilated by Ensemble Kalman Filter.

Results from data assimilation show that the unobserved variable can be better improved when the background error variance of the observed variable and the background error cross-covariance between the observed and unobserved variables are larger. Spreading observations over the assimilation time window can also increase chances of correcting the unobserved variable. However, the improvement in the unobserved variable is minor, if the ensemble mean differs from the true atmosphere state.

5.1 Introduction

The improvement brought by radar data assimilation to mesoscale numerical forecast is always short-lived (less than 2~3 hours, Aksoy et al. 2009, 2010; Chang et al. 2014; Surcel et al. 2014). One plausible explanation for this is that some influential model state variables in the initial condition are still inaccurate even after data analysis. It is challenging to correct those variables by assimilating radar observations alone as only reflectivity and radial velocity observations are available in radar data. Nevertheless, many unobserved state variables are crucial for numerical prediction. For example, a successful precipitation forecast requires supporting vertical velocity in model initial condition. However, only a small component of vertical velocity is contained in the observed radar radial velocity. In order to reconstruct such a model field by data assimilation, significant and reliable flow-dependant cross-covariances between errors of observed and unobserved variables in the background are needed (Snyder and Zhang 2003). For this reason, ensemble-based data assimilation systems (e.g. Ensemble Kalman Filter and Ensemble-Variational method), using ensemble members to estimate background error statistics, are appropriate for radar data assimilation. However, those ensemble-based systems cannot improve the unobserved variables everywhere. For instance, in the areas where error cross-covariances are weak, there is low chance of updating unobserved variables. Since traditional mechanical radar scans the atmosphere without spatial preference, data from it do not guarantee to be placed at the locations where the unobserved variables can be greatly influenced. Consequently, under such circumstance, it is difficult to improve the numerical forecasts.

In contrast to traditional radar, modern radar employing phased-array technique is able to sample the atmosphere adaptively in space and time as required by the user, since the radar beam can be electronically steered by adjusting the phases of an array of antennas. Many studies and research projects were performed to demonstrate the benefits brought by phased-array radar data to weather forecast, such as higher temporal resolution (Lu and Xu. 2009, Yussouf and Stensrud 2010) and adaptive scanning (Heinselman et al. 2011). Adaptive radar scanning directs radar to target on the user-defined areas of interest, which increases the observation accuracy and temporal resolution without losing useful information in the important regions. From the perspective of radar data assimilation, this adaptive scanning can be used to focus on the areas ‘rich’ in background error cross-covariances in order to increase the chance of improving unobserved model variables.

The presented study introduces an idealized adaptive radar observation method, which takes advantage of hypothetical fast scanning radar to adaptively collect observations in space and time according to the background error statistics calculated from a set of ensemble model simulations. The purpose of this adaptive observation is to efficiently correct unobserved fields in the analysis step of data assimilation, ideally so as to improve the precipitation forecast accordingly. In the following experiments, simulated radial velocity is the only observation, and is assimilated by Ensemble Kalman Filter (EnKF) to correct the vertical velocity in the model. Background error cross-covariances, as well as other error statistics, provide the criterion for deciding adaptive observation strategies. Several observation strategies are proposed and compared in terms of their impact on the analysis uncertainty of unobserved vertical velocity.

The remainder of the article is organized as follows. In the next section, the experiment numerical setup is presented, including model configuration, observation simulation and data assimilation scheme. Section 5.3 provides the theoretical explanation of how an unobserved variable is corrected via observation by data assimilation during the analysis step. Section 5.4 introduces and compares different radar observation strategies. In Section 5.5, the simulated truth is used to evaluate different observation methods. In addition, this section discusses the problem of data assimilation caused by the difference between ensemble-mean and the truth. Finally, this article closes with a summary and some discussions in the last section.

5.2 Experiment setup

The experiment conduced in this study consists of ensemble numerical forecasts, adaptive observation strategy, data assimilation and verification. As shown in Fig. 5.1, the Global Environmental Multiscale Limited Area Model (GEM-LAM) is applied to yield 80 members of ensemble forecast. The first member is considered to be the true atmosphere state (henceforth to be referred as ‘truth’), while the other 79 ensemble members compose the background for data assimilation. Error statistics estimated from background ensemble members are used to decide the adaptive observation strategy, according to which the simulated radial velocity observations are generated from the truth. Finally, observations and the background are combined statistically by the EnKF analysis scheme. Although vertical velocity is not completely observed, it can be updated through the background error cross-covariance matrix by EnKF. After data assimilation, the impacts of different observation strategies on data assimilation are evaluated by analysis uncertainties estimation.

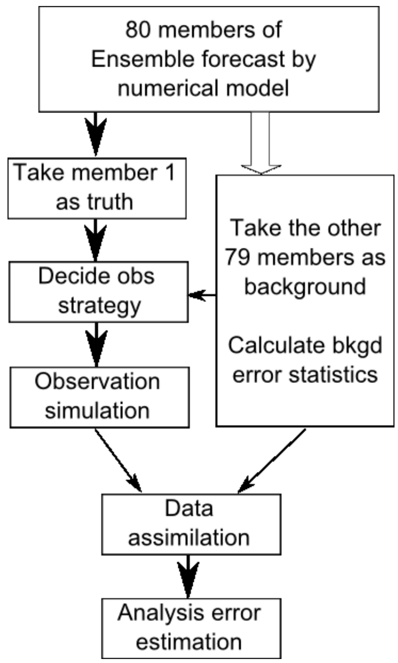

Fig. 5.1 Flowchart for the experiment of adaptive radar observation.

a. Model configuration and ensemble forecasts

Ensemble forecasts in this study are produced by a fully compressible GEM-LAM covering the Montréal region with 1-km horizontal grid spacing and 300 km by 300 km extension. As shown in Fig. 5.2, a global-driven three-level nested domain is configured to finally drive the 1-km model. The operational global EnKF system at the Canadian Meteorological Center provides initial and lateral boundary conditions for the ensemble limited-area simulations in domain A with horizontal grid spacing of 15-km. Conventional data assimilation is performed on LAM-15km by EnKF method every 6 h for two cycles. A second nested LAM (domain B) located around southern Québec is then driven by the parental LAM-15km and runs at 2.5-km horizontal grid spacing so as to produce 80 members of ensemble forecast. The LAM at 1-km horizontal grid spacing (domain C) is launched 6 hours later than the initiation of LAM-2.5km forecasts, with integration time step of 30 s. The 80 ensemble 1-km LAM simulations are then integrated for 30 minutes until the observation strategy is decided. Radar data assimilation is then performed on the 1-km LAM. The 80 ensemble members, originating from operational global EnKF system, ensure large ensemble spread, and therefore provide reasonable background error statistics for adaptive observation and data assimilation.

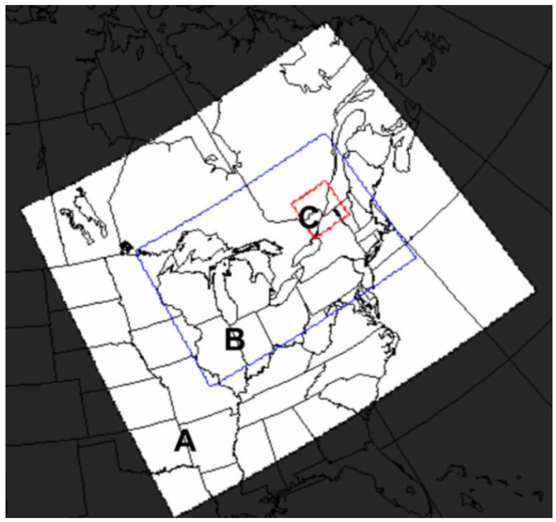

Fig. 5.2 The 1-km grid spacing GEM-LAM covering the Montréal region and its parental models. A: LAM 15-km grid spacing; B: LAM 2.5-km grid spacing; C: LAM 1-km grid spacing.

The limited-area simulations are fully non-hydrostatic with 58 hybrid vertical levels and a lid at 10 hPa. The "Interaction between Surface, Biosphere and Atmosphere" (ISBA; see Noilhan and Planton 1989) land surface scheme is applied. The Kain-Fritsch moist convective parameterization scheme (Kain and Fritsch 1990) is employed in LAM-15km; however no convective parameterization is used in either LAM-2.5km or LAM-1km. The double-moment version of the Milbrandt and Yau (2005) microphysics scheme is used for the grid-scale processes. In ensemble forecasts, physical schemes are the same for different members. Detailed descriptions of the dynamics and physics formulations can be found in Côté et al. (1998) and Mailhot et al. (1998), respectively.

The same model configuration described above was also used for assimilation of real radar data (Chang et al. 2014).

b. The truth and simulated observations

The first of the 80 ensemble forecasts is used as the truth. The truth fields include the model outputs of three wind components, temperature, humidity, rain mixing ratio and reflectivity. Although model does not directly produce radar radial velocity, it can be easily calculated from wind components by:

$$Vr = U\sin(\varphi)\cos(\theta) + V\cos(\varphi)\cos(\theta) + W\sin(\theta) \tag{5.1}$$

where U, V and W are three wind components; φ and θ are azimuth and elevation angles respectively, which are related to the radar location depicted in Fig. 5.3. In this study, radial velocity Vr is also considered to be the model state variable. The reflectivity, radial velocity and vertical velocity fields on the model level around 800hPa are shown in Fig. 5.3, from which one can tell that strong precipitation is usually associated with noisy vertical velocity and radial velocity.

Given the truth, Vr observations are here generated by simply adding Gaussian distributed random noise onto the true Vr field (Fig. 5.3a). The observation errors are independent in space and have a standard deviation of $\sigma_o = 2\, m\, s^{-1}$. The simulated radial velocity observations are shown in Fig. 5.3d. In contrast the truth, Vr observations are not available in the entire model domain as they can only be sampled by radar where precipitation exists. Thus simulated Vr observations have the same spatial coverage as the true reflectivity field (Fig. 5.3c).

In Fig. 5.3d, the simulated radar observations in this study are located on model grids, and differ from the real radar data distributed in radar geometry. Although this setup is not realistic, it is convenient for computing and analyzing the background error statistics on model grids. Adaptive radar observation methods proposed in section 5.4 will use the grid-wise error statistics to select a number of observations from Fig. 5.3d.

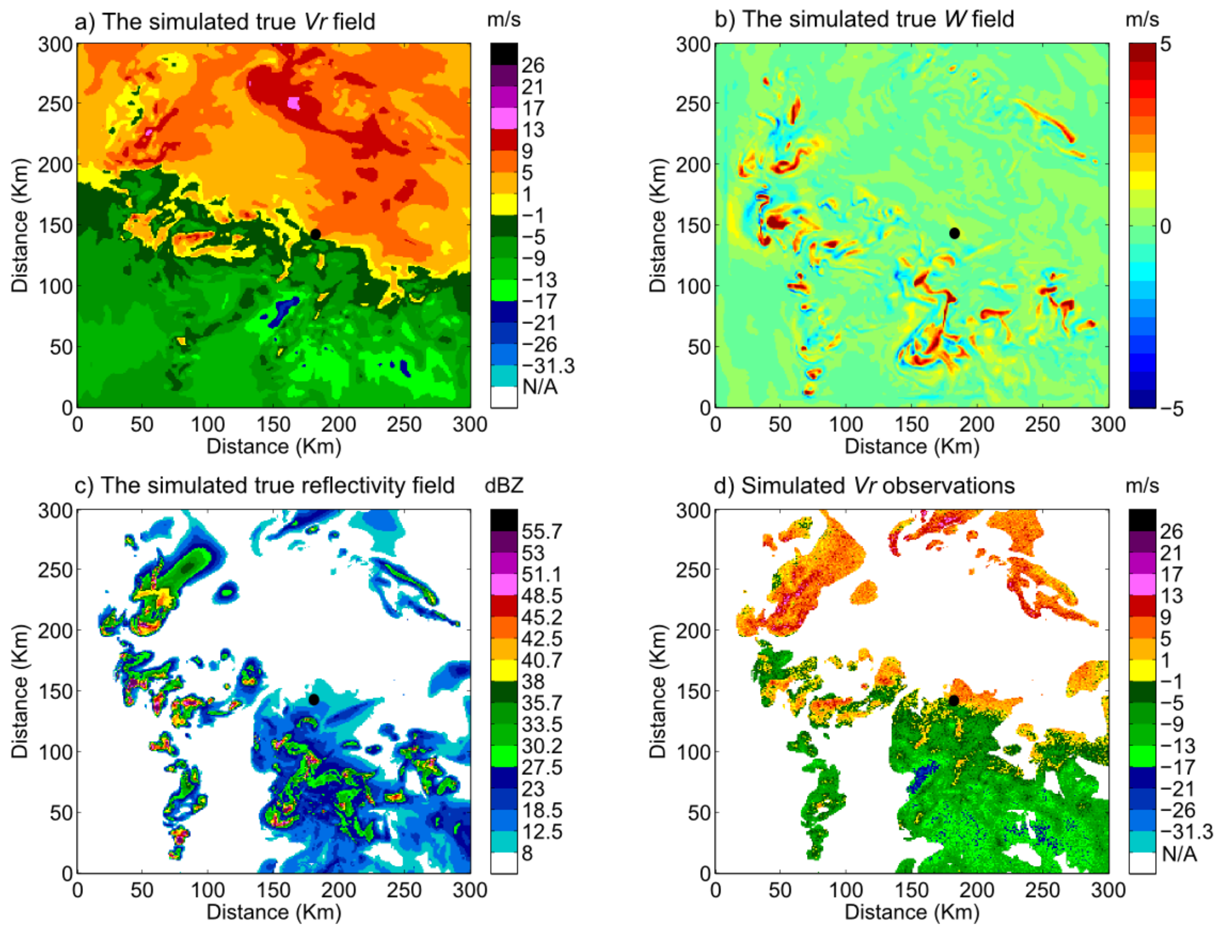

Fig. 5.3 The radial velocity (a), vertical velocity (b) and reflectivity (c) fields of the truth, and simulated radial velocity observations (d). The radar locations are denoted by black dots.

c. EnKF data assimilation scheme

An EnKF data analysis system is used to assimilate the simulated observations selected by the adaptive observation strategy. Similar to the equations presented in Evensen (1994), the basic EnKF algorithm is described as:

$$\mathbf{K} = \mathbf{P}^f \mathbf{H}^T (\mathbf{H}\mathbf{P}^f \mathbf{H}^T + \mathbf{R})^{-1} \tag{5.2}$$

$$\mathbf{X}_j^a = \mathbf{X}_j^f + \mathbf{K}(\mathbf{O}_j - \mathbf{H}\mathbf{X}_j^f) \tag{5.3}$$

where subscript j represents the ensemble member index; $\mathbf{K}$ is the Kalman gain; superscripts a and f represent analysis and background (i.e. forecast) respectively; $\mathbf{X}$ is the model state vector;

$\mathbf{O}_j$ represents perturbed observation vector (Whitaker and Hamill, 2002); $\mathbf{H}$ stands for the observation operator; $\mathbf{R}$ is the observation error covariance matrix; $\mathbf{P}^f$ is the background error covariance matrix. The error covariance matrices for both analysis and forecast can be estimated from the ensemble members by:

$$\mathbf{P} = \frac{1}{N-1}\sum_{j=1...N}(\mathbf{X}_j - \overline{\mathbf{X}})(\mathbf{X}_j - \overline{\mathbf{X}})^T \tag{5.4}$$

where $\mathbf{P}$ can be error covariance matrices for analysis ($\mathbf{P}^f$) or forecast ($\mathbf{P}^a$); $\mathbf{X}_j$ is the ensemble member of analysis or forecast; $\overline{\mathbf{X}}$ is the ensemble mean.

In addition to this basic analysis scheme, two-dimensional localization works on top of the calculation of background error covariance matrices in Eq. (5.4) in order to reduce noise in cross-covariances (Houtekamer and Mitchell 2001). The localization algorithm follows Eq. (4.10) in Gaspari and Cohn (1999), where 10-km is used as the scale parameter. Accordingly, the cut-off distance is twice as large as the above scale parameters.

In order to simplify the experiment, only radial velocity *Vr* and vertical velocity *W* on one model level around 800hPa are updated in analysis, the former of which can be directly observed by radar. Although the latter partially contributes to radial velocity, its contribution is small especially at low elevation angles (Eq. 5.1). Therefore in the following discussions, while radial velocity *Vr* is the 'observed' variable, vertical velocity *W* is called the 'unobserved' variable.

5.3 Theoretical influence of observation on unobserved variable

Snyder and Zhang (2003) stressed the importance of background error covariances for reconstructing the unobserved fields. In this section, the update of unobserved variable through background error covariances is examined in a theoretical and much simpler manner.

Suppose that the model state vector contains two elements $\mathbf{X} = [Vr \quad W]^T$. Since only the first variable is observable, the observation operator can be written as $\mathbf{H} = [1 \quad 0]$. The observation and background error covariance matrices are then expressed as $\mathbf{R} = \sigma_O^2$ and

$\mathbf{P}^f = \begin{bmatrix} \sigma_{Vr}^2 & Cov(Vr,W) \\ Cov(Vr,W) & \sigma_W^2 \end{bmatrix}$ respectively, where σ_O is observation error standard deviation; σ_{Vr} and σ_W are background error standard deviations of radial velocity and vertical wind in the background; $Cov(Vr,W)$ represents the background error cross-covariance between *Vr* and *W*. After substituting the above matrices into (5.2) and (5.3), the increments (defined as analysis - forecast) of *Vr* and *W* for each ensemble member are

$$\Delta Vr_j = \frac{\sigma_{Vr}^2}{\sigma_{Vr}^2 + \sigma_o^2} Innov_j(Vr) \tag{5.5}$$

$$\Delta W_j = \frac{Cov(Vr,W)}{\sigma_{Vr}^2 + \sigma_o^2} Innov_j(Vr) \tag{5.6}$$

where $Innov_j(Vr)$ is the innovation of *Vr*, which is defined as observation minus background of *Vr* for the *j*th ensemble member. Note that the unobserved *W* is updated by innovation of *Vr*. Theoretically, the update of *W* leads to the reduction of analysis error variance of *W*, as compared to its background error variance. Under the assumption of linear observation operator and approximation between ensemble mean and the truth, analysis error covariance matrix is computed by

$$\mathbf{P}^a = \mathbf{P}^f - \mathbf{P}^f \mathbf{H}^T (\mathbf{H}\mathbf{P}^f \mathbf{H}^T + \mathbf{R})^{-1} \mathbf{H}\mathbf{P}^f \tag{5.7}$$

where $\mathbf{P}^a$ indicates analysis error covariance matrix; other notations are the same as before. From Eq. (5.7), the difference between analysis and background error covariance matrix is written as

$$\mathbf{P}^f - \mathbf{P}^a = \frac{1}{\sigma_{Vr}^2 + \sigma_O^2} \begin{bmatrix} \sigma_{Vr}^4 & \sigma_{Vr}^2 Cov(Vr,W) \\ \sigma_{Vr}^2 Cov(Vr,W) & Cov^2(Vr,W) \end{bmatrix} \tag{5.8}$$

Consequently, the estimated reduction of error variance of *W* can be expressed as:

$$\Delta\sigma_W^2 = \frac{Cov^2(Vr,W)}{\sigma_{Vr}^2 + \sigma_O^2} = \frac{\sigma_W^2 \rho^2(Vr,W)}{1 + \sigma_O^2 / \sigma_{Vr}^2} \tag{5.9}$$

where $\rho(Vr, W)$ is the cross-correlation between two variables. Equation (5.9) suggests that in order to appreciably reduce the error variance of unobserved *W*, σ_{Vr} / σ_O and $\sigma_W^2 \rho^2(Vr, W)$ have to be sufficiently large. This is reasonable, as a large σ_{Vr} / σ_O value indicates that observation is more reliable than the background, and therefore ensures the significant influence of observations on the observed variable. The large value of $\sigma_W^2 \rho^2(Vr, W)$ can in turn efficiently transfer information from the observed variable *Vr* to unobserved variable *W* because their errors are much cross-correlated.

In Eq. (5.9), since observation error standard deviation σ_O is usually a constant (2 m s^{-1} in this study), the effect of assimilating *Vr* observation on the state variable *W* depends only on the flow-dependant background error statistics including σ_{Vr}, σ_W and $\rho(Vr, W)$, which can be estimated from ensemble members. Such a property allows observation strategy to be decided according to ensemble forecasts, and before observations are collected.

Note that (5.9) provides only a rough estimation because it neglects spatial correlation and cross-covariances among other variables. Moreover, (5.9) estimates the error variance reduction under the same assumptions as in EnKF, such as the ensemble mean being equal or close to the truth.

5.4 Adaptive observation strategies

This section proposes the methods of adaptive radar observation that increases the possibility of correct the unobserved vertical velocity through radar data assimilation. When only radial velocity *Vr* is observed and assimilated, (5.9) proves that the reduction of vertical velocity error standard deviation ($\Delta\sigma_W^2$) is determined by background error cross-covariance between *Vr* and *W*, as well as the background error variance of *Vr*. In the following subsections, background error statistics will be exhibited first, followed by four experiments about observation strategies and data assimilation. The uncertainty reduction of the unobserved *W* field is then computed for evaluating the effectiveness of adaptive radar observation.

As stated in the subsection 5.2b, simulated observations are placed on model grids for all the following experiments. This is not realistic because radar samples the atmosphere along the path of the beam; the user of phased-array radar can only specify the pointing direction of radar beam, instead of the desired model grid. Nevertheless, our experiment setup is helpful for analyzing the background error statistics.

a. background error statistics

Given 79 ensemble background members, statistical properties including ensemble mean, standard deviation and cross-correlation of errors can be calculated for each model grid, as shown in Fig. 5.4. One must note that the error statistics are computed with respect to the ensemble mean (5.4), which is consistent with most ensemble-based real data assimilation systems where the truth is unknown. The error statistics with respect to the truth will be discussed in the next section. Figures 5.4a, 5.4b and 5.4c exhibit great spatial variation. According to the discussions in section 5.3, if observation is placed where σ_{Vr} is large, *Vr* at that location is largely corrected. On the other hand, significant improvement of *W* is possible only at the grids where background error standard deviations σ_{Vr}, σ_W and error cross-correlation $\rho(Vr, W)$ are large. Note that $\rho(Vr, W)$ is close to zero at many grid points (Fig. 5.4c), which inhibits the correction of unobserved *W*. Adaptive observation in this study is supposed to avoid those areas and target the locations where *W* can be corrected more efficiently.

In addition, Fig. 5.4d provides the ensemble mean of rain mixing ratio, from which one can tell that the precipitation area is correlated with large σ_{Vr} and σ_W values in space. In addition, the location difference between the ensemble mean precipitation (Fig. 5.4d) and the truth (Fig. 5.3c) is usually considered as background phase error. Such an error is common for real radar data assimilation. However, phase error may affect the adaptive observation because some of the areas where *W* has a greater chance to be improved, which could be the same areas of strong precipitations in background, may not be observable.

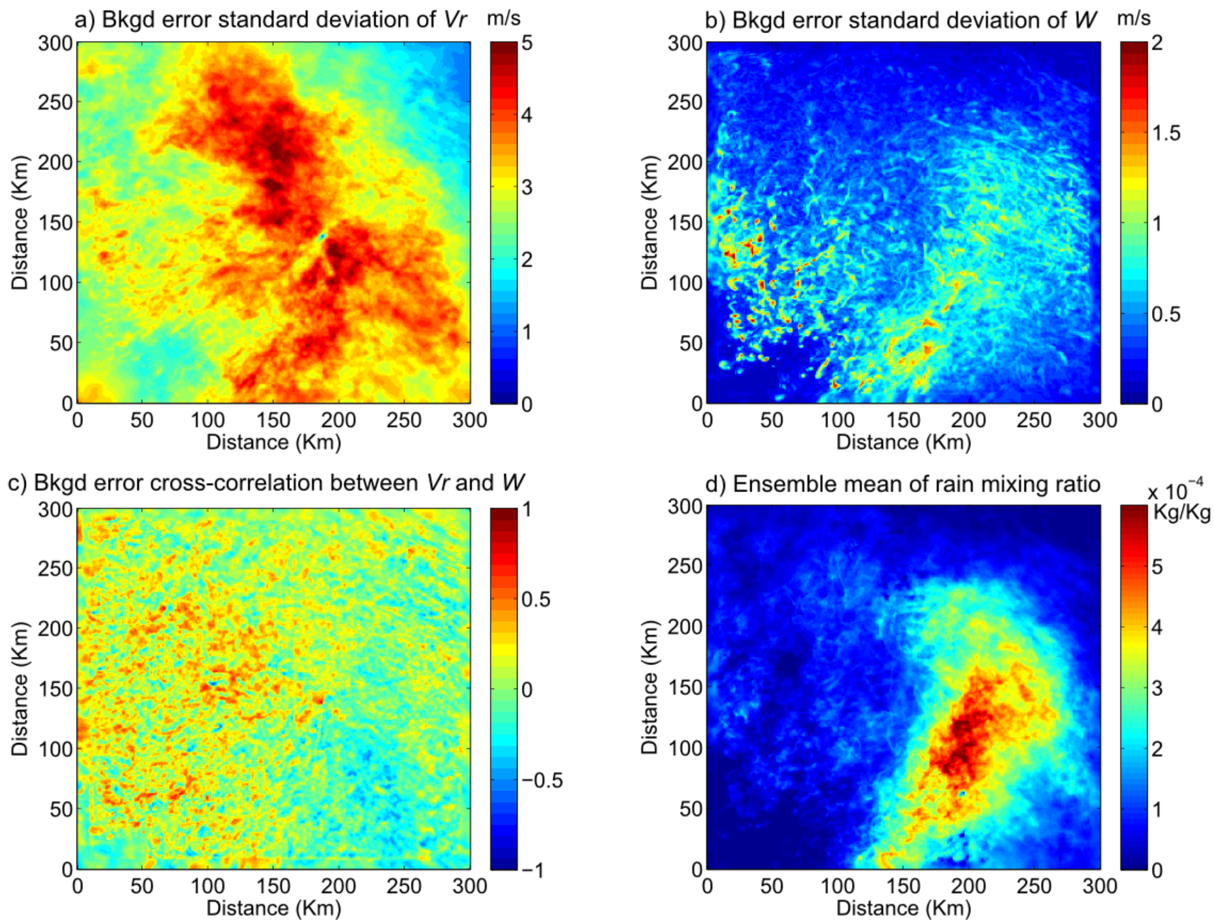

Fig. 5.4 Background error statistics. a) Standard deviation of *Vr* error. b) Standard deviation of *W* error. c) Cross-correlation between errors of *Vr* and *W*. d) Ensemble mean of rain mixing ratio.

b. Uniformly distributed observations

Let us first apply traditional uniformly distributed observations in order to provide a reference for the evaluation of adaptive observations in the next subsection. Two types of uniformly distributed observations are simulated in this section. The first spreads observations in the entire 2-D model domain, so as to mimic the observation strategy of traditional mechanical radar which scans the entire atmosphere regardless precipitation coverage. The second places the same number of observations only in precipitation regions, which simulates the 'focused scan' performed by phased-array radar (Heinselman et al. 2011). However, neither of these methods uses background error statistics to choose observation locations for improvement of the unobservable variable.

In the first experiment, 900 'potential' observations are uniformly distributed in the 300 km by 300 km 2-D domain (observations are located every 10 km), as shown in Fig. 5.5. They are called 'potential' observations because many of them, although placed in the domain, cannot be observed by radar if they are not covered by detectable precipitation. Under precipitation coverage, 325 *Vr* observations can be assimilated by the EnKF data analysis system described in subsection 5.2c.

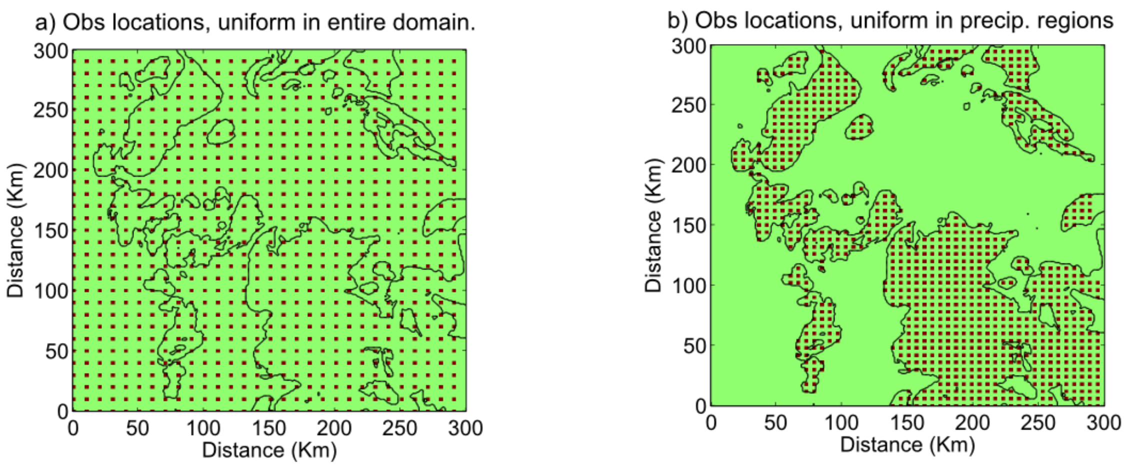

Fig. 5.5 Locations of uniformly distributed observations. a) 900 observations distributed in the entire domain. b) 900 observations distributed only in the precipitation region.

Given the ensemble analysis produced by data assimilation, analysis error standard deviations are calculated with respect to the ensemble mean. The reductions of error standard deviations in *percentage* (defined as 'background error standard deviation – analysis error standard deviation' divided by 'background error standard deviation') are shown in Figs. 5.6a and 5.6b for *Vr* and *W* respectively. Significant *Vr* error reduction is usually associated with a large σ_{Vr} value in background. In other words, the observed variable is corrected more when its uncertainty in background error is larger. The reduction of *W* error standard deviation is quite small (5%-10% in Fig. 5.6b), as compared to the *Vr* error reduction (40%-50% in Fig. 5.6a). Updating the unobserved variable is more challenging partly due to the weak error cross-correlation (Fig. 5.4c).

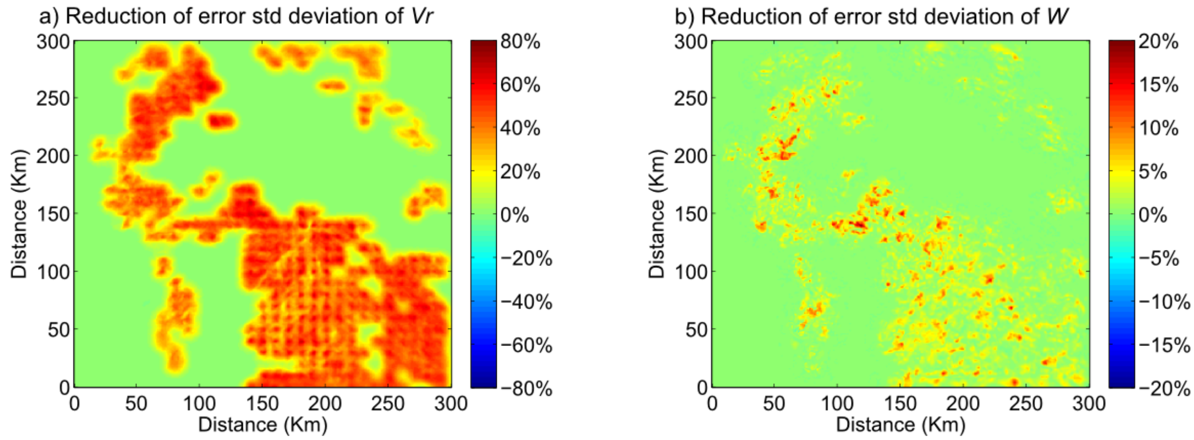

Fig. 5.6 Reduction of error standard deviation for *Vr* (a) and *W* (b) in percentage, when 900 observations are uniformly distributed in the entire two-dimensional model domain.

In the second experiment, 900 observations are uniformly placed every 6 km, but only in precipitation regions as shown in Fig. 5.5b. After data assimilation, the reduction of error standard deviation is shown in Fig. 5.7. The error reduction for *Vr* is around 60% almost everywhere within and around observation area (Fig. 5.7a). Moreover, the error reduction for *W* can reach 15%-20% in many areas. The differences between Figs. 5.7 and 5.6 indicate that the second experiment is superior in term of reducing *Vr* and *W* uncertainties.

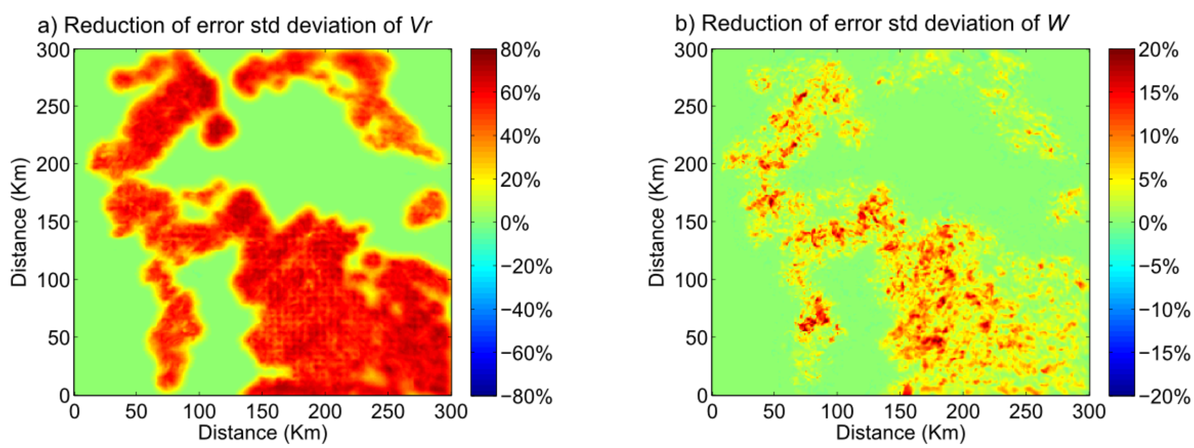

Fig. 5.7 Reduction of error standard deviation for *Vr* (a) and *W* (b) in percentage, when 900 observations are uniformly distributed in the precipitation region.

The difference between the results of the above two experiments is mainly caused by the different amount of assimilated observations. Since the first experiment assimilates much less information than the second experiment does, the analysis uncertainty in the first one is much higher for both *Vr* and *W*.

c. Adaptive radar observation based on background error statistics.

Previous experiment results demonstrate the limited influence of assimilating *Vr* for correcting the unobserved model state variable *W*. To amplify this influence, the experiment presented in this subsection applies an adaptive observation method which places more observations in the areas where uncertainties of *W* are more likely to be reduced while keeping the same total dwell time. Given the background error statistics presented in Fig. 5.4, the reduction of *W* error variance (background error variance – analysis error variance for *W*) can be estimated by Eq. (5.9) on every model grid in a rough but fast manner before collecting and assimilating *Vr* observations. The estimated $\Delta\sigma_W^2$ are shown in Fig. 5.8, where greater values indicate the greater potential for producing a more precise *W* analysis on the corresponding grid points. The figure shows that many locations with large values cannot be observed by radar because they are not covered by precipitation, such as in the west area of the domain. On the other hand, since the values in the northern part of the domain are close to zero, collecting observations there may have little contribution to the *W* correction, although those areas can be observed.

The spatial variability of $\Delta\sigma_W^2$ implies the importance of selecting proper observation locations for the improvement of *W*. Thus, the observation locations in this adaptive observation strategy are chosen according to the $\Delta\sigma_W^2$ value in Fig. 5.8 from high to low, until all 900 observations are gathered. The final observation locations decided by this process are displayed in Fig. 5.9a. Compared to the uniformly distributed observations in Fig. 5.5b, the new observation strategy removes many observations in the north and the southeast corner of the domain, and adds more observations near the center and to the west of the domain.

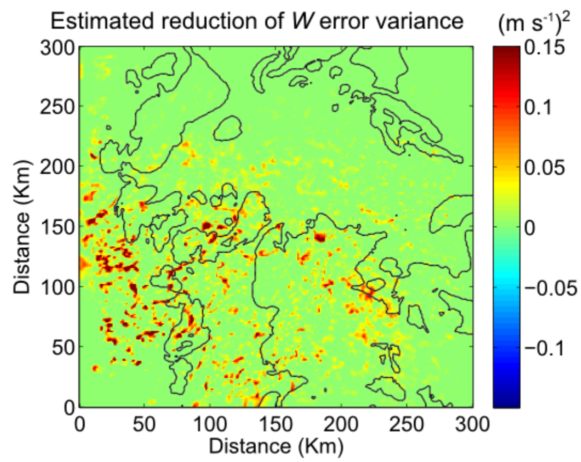

Fig. 5.8 Reduction of W error variance estimated by Eq. (5.9). Black contour indicates the true precipitation region.

After assimilating these selected observations by EnKF, the error standard deviations are more significantly reduced for both Vr and W (Figs. 5.9b and 5.9c), compared to the previous experiment (Figs. 5.7a and 5.7b). The reduction of W uncertainty is higher than 20% in many regions. Fig. 5.9d shows the difference between the analysis error standard deviations of W for the current experiment and the previous experiment where observations are uniformly distributed in precipitation areas (i.e. analysis error standard deviation for the previous experiment – analysis error standard deviation for the current experiment). Although many observations are removed from the north and the southeast corner of the domain, the values shown in Fig. 5.9d in these regions are not very negative. This suggests that the removal of observations in those regions has little impact on W analysis. In fact, W in those regions can hardly be updated no matter how many observations are placed there because the background error statistics cannot efficiently transfer observation information to the unobserved variable. On the other hand, placing more observations near the center, to the west and south of the domain helps to better improve the W field (e.g. the dark red colors in Fig. 5.9d).

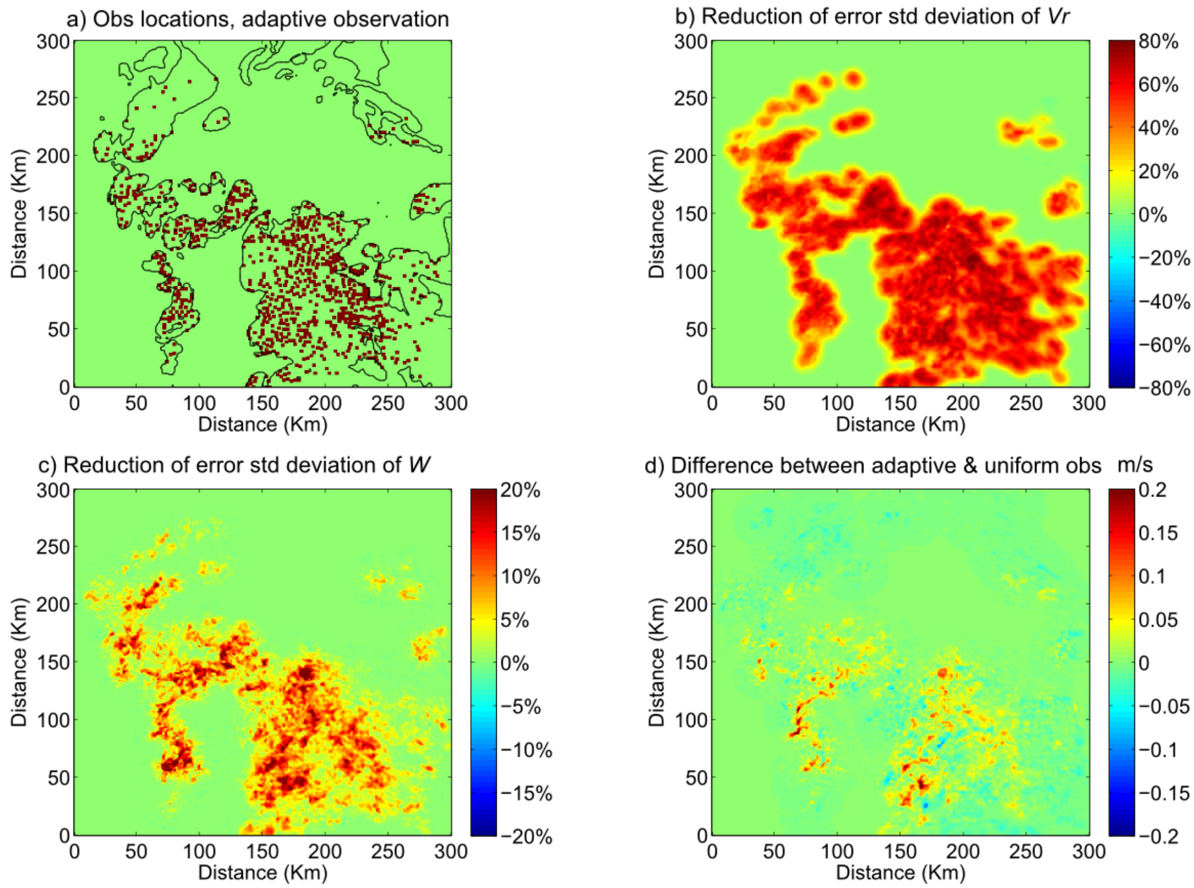

Fig. 5.9 a) Observation locations for the adaptive radar observation strategy. Black contour indicates the true precipitation region. Dark red points indicate the selected observation locations. b) Reduction of error standard deviation for *Vr* in percentage. c) Reduction of error standard deviation for *W* in percentage. d) Difference between analysis error standard deviations of *W* for the uniform observation strategy and the adaptive observation strategy.

d. Observations adaptively distributed in space and time

Radar employed phased-array technique can sample the atmosphere adaptively in both space and time. For example, radar can focus on some section in the first minute and then immediately steer the beam towards another direction in the next minute. Therefore, in addition to adaptively placing observations in space as described in the previous subsection, observations can also be spread adaptively over time.

In fact, assimilating *Vr* observations collected at different times is probably more beneficial for improving *W* if the time-lagged background error cross-correlation is more significant. Time-lagged background error cross-correlation is the correlation between errors of two variables produced at two different time steps. This experiment seeks to improve *W* at time T (analysis time), by assimilating *Vr* observations collected at T and 5 minutes before T (denoted as T-5).

The adaptive observation method considering both space and time is also practical in reality. For example, at time T-5, one can have ensemble forecasts for both T-5 and T. Both the time-lagged error statistics, and the same-time error statistics can be calculated and used for deciding temporal observation distribution for T-5 and T. According to the adaptive observation strategy decided at T-5, data can be collected at T-5 and T. After data assimilation, analysis is produced at T.

In addition, it is common for an ensemble-based system to assimilate observations produced at times differing from the analysis time. For example, the assimilation window in the operational global EnKF at the Canadian Meteorological Center is 6 hours (+/- 3 hours with respect to the analysis time), within which all data are assimilated to produce analysis at the central time (Houtekamer et al. 2005). The configuration of the assimilation window is also available in the Data Assimilation Research Testbed (Anderson et al. 2009) and the ensemble-based variational system (Mark Buehner et al. 2012).

Given *Vr* observations available at time T-5, their potential influence on improving *W* at T needs to be estimated. Similar to (5.9), the error variance reduction for *W* at T can be written as

$$\Delta\sigma_{W,T}^2 = \frac{Cov^2(Vr_{T-5}, W_T)}{\sigma_{Vr,T-5}^2 + \sigma_O^2} = \frac{\sigma_{W,T}^2 \rho^2(Vr_{T-5}, W_T)}{1 + \sigma_O^2 \big/ \sigma_{Vr,T-5}^2} \tag{5.10}$$

where W_T is the background vertical velocity at T; Vr_{T-5} denotes the background radial velocity at T-5. Equation (5.10) shows that the estimated error variance reduction depends on the background error variance of *Vr* at T-5, as well as the time-lagged background error cross-covariance between *Vr* at T-5 and *W* at T. Figures 5.10a and 5.10b show $\sigma_{Vr,T-5}$ and $\rho(Vr_{T-5}, W_T)$

respectively. Comparison between Figs. 5.10a and 5.4a implies that the general *Vr* error structures do not change much after 5 min's model integration. However, small differences can still be identified. The time-lagged cross-correlation $\rho(Vr_{T-5}, W_T)$, although is quite week in most areas (Fig. 5.10b), has spatial patterns slightly different from $\rho(Vr_T, W_T)$ in Fig. 5.4c. These minor differences may increase the chance of better improving *W* by putting some *Vr* observations at times T-5.

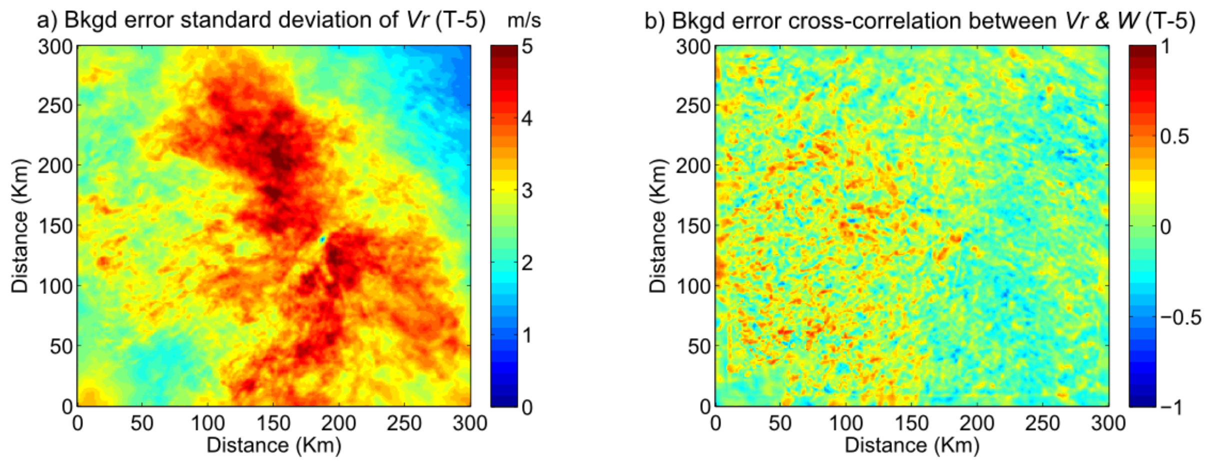

Fig. 5.10 a) Background error standard deviation of *Vr* at time T. b) Time-lagged error cross-correlation between *Vr* at T-5 and *W* at T.

Given these time-lagged error statistics, $\Delta\sigma^2_{W,T-5}$ is calculated from Eq. (5.10) and is plotted in Fig. 5.11a. The observation locations are selected according to $\Delta\sigma^2_{W,T-5}$ values (Fig. 5.11a) and $\Delta\sigma^2_W$ values at each grid point (Fig. 5.8) from high to low, until 900 observations are gathered. When the locations of observations are selected because of the greater values of $\Delta\sigma^2_{W,T-5}$, those observations should be collected at time T-5. Other observations should be collected at the analysis time T. This observation strategy is called here 'time-space adaptive observation' in the following discussion, while the observation strategy in the previous subsection is called 'space-only adaptive observation'.

The final observation locations selected by the time-space adaptive observation are shown in Fig. 5.11b. Note that one observation location is not selected repeatedly at T-5 and at T in the current strategy. Figure 5.11b indicates that collecting some *Vr* observations 5 minutes before the analysis time can improve *W* more efficiently. Additionally, since the precipitation at T-5 and T covers slightly different areas due to its movement, assimilating observations generated at both times may impact larger areas.

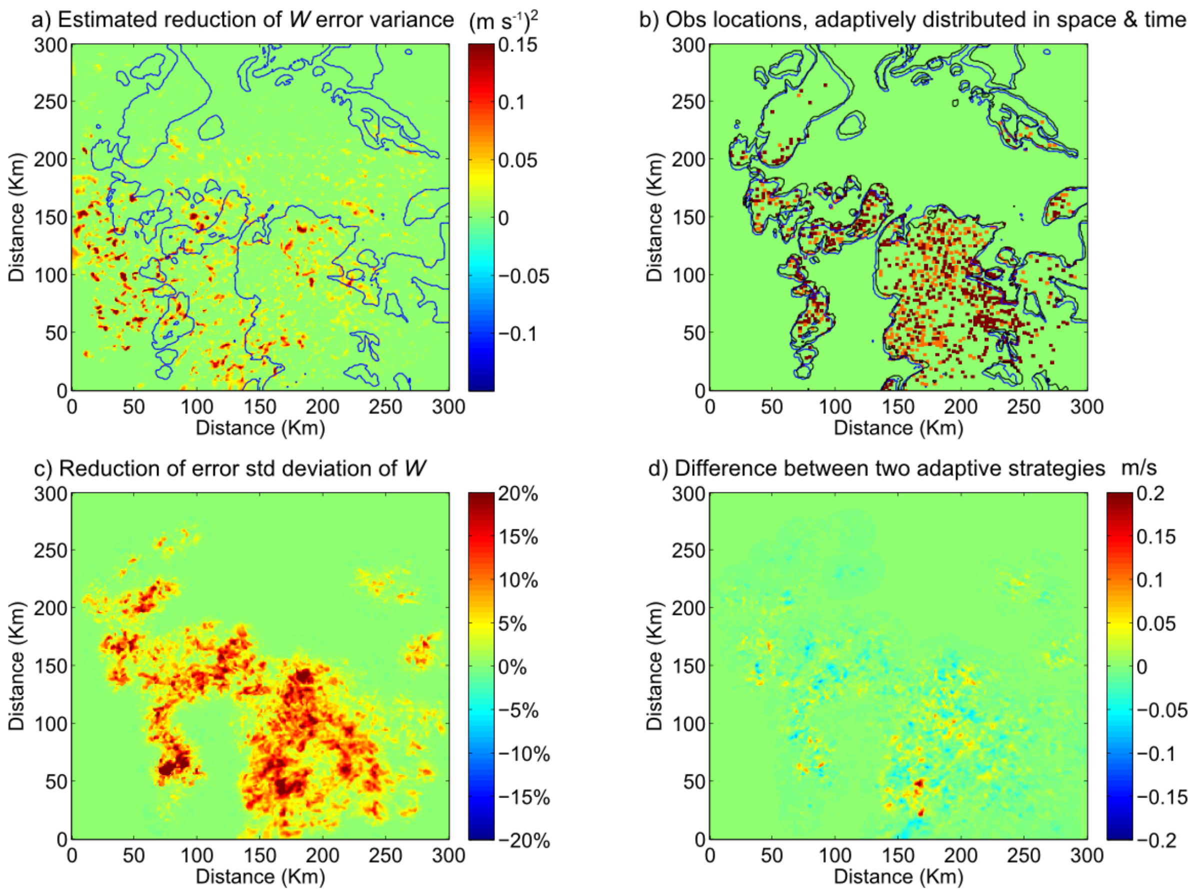

Fig. 5.11 a) Reduction of *W* error variance estimated by Eq. (5.10). b) Observation locations for the adaptive radar observation considering both time T-5 and time T. Black and blue contours indicate the true precipitation region at time T and T-5 respectively. Dark red points and orange points indicate the observation location at time T and T-5 respectively. c) Reduction of error standard deviation for *W* resulted from time-space adaptive observation in percentage. d) Difference between analysis error standard deviations of *W* for the space-only adaptive observation strategy and the time-space adaptive observation strategy.

After assimilating the observations adaptively collected in space and time, the error standard deviation of *W* is reduced, as shown in Fig. 5.11c. The difference between analysis error standard deviations of *W* for the experiments of time-space adaptive observation and space-only adaptive observation (i.e. analysis error standard deviation for the space-only adaptive observation – analysis error standard deviation for the time-space adaptive observation) is demonstrated in Fig. 5.11d. The proposed time-space adaptive observation strategy reduces more *W* uncertainties than the previous space-only adaptive observation strategy, especially around the location of (x=170, y=30~50) where many observations are collected at T-5 (Fig. 5.11b). More quantitative comparison of different observation strategies can be found in Fig. 5.14.

5.5 Verification by 'truth'

In the adaptive observation experiments presented above, error statistics calculated with respect to the ensemble mean are used to evaluate observation strategies. This evaluation method may underestimate the errors of the ensemble members because it does not include the difference between the ensemble mean and the truth. Consequently, the effect of adaptive observation could be misjudged. Therefore, the truth is used in this subsection to estimate uncertainties in the ensemble members before and after data assimilation, and re-evaluate the benefit brought by adaptive radar observation.

The differences between the background ensemble mean and the truth are shown in Figs. 5.12a and 5.12b for *Vr* and *W* respectively. Since the truth and the background members are from the same ensemble, most values in Fig. 5.12 are smaller than or comparable to the 'mean-based' error standard deviations (Figs. 5.4a and 5.4b), except for some areas to the south and the west of the domain. The fact that the spatial pattern in Fig. 5.12 is similar to the truth fields (Figs. 5.3a and 5.3b) implies that the ensemble mean is small, which is due to the average over largely spread members. Given the truth as reference, the error variance can be written as

$$\sigma_t^2(x) = \sigma_m^2(x) + (\bar{x} - x_t)^2 \tag{5.11}$$

where x is a state variable representing *Vr* or *W* in this case; $\sigma_t^2(x)$ is the error variance of x with respect to truth; $\sigma_m^2(x)$ is the error variance of x with respect to ensemble mean; $\bar{x} - x_t$ is the error of the ensemble mean with respect to the truth. Equation (5.11) suggests that the truth-based variance can better describe the uncertainties in ensemble members since the error of ensemble mean is considered. Figures 5.12c and 5.12d show that the truth-based background error standard deviations are much greater than the mean-based background error standard deviations in Fig. 5.4a and 5.4b.

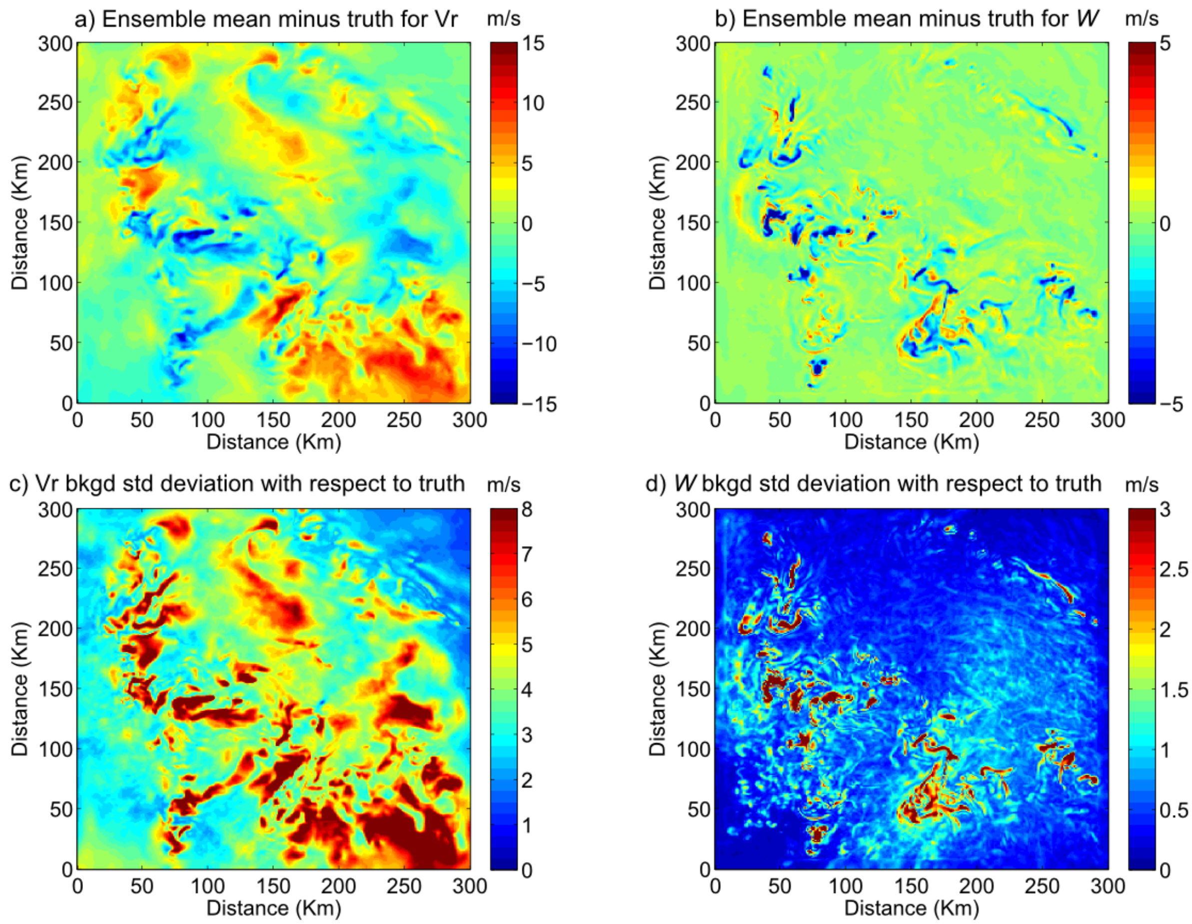

Fig. 5.12 Background ensemble mean minus the truth for *Vr* (a) and *W* (b). Background error standard deviation of *Vr* (c) and *W* (d), with respected to the truth.

Since error statistics with respect to the ensemble mean may underestimate the uncertainties, the evaluation results based on them in the previous section could be misleading. For example, the conclusion that adaptive observation is better than uniform observation in terms of error reduction of *W* (Figs. 5.9b, 5.9c and 5.9d) becomes less convincing when the ensemble mean differs from the truth.

Given the knowledge of the true atmosphere state in this study, the error reduction is recalculated based on the truth-based error variances (Eq. 5.11) as presented by Fig. 5.13. The positive and negative values in Fig. 5.13 respectively represent improvement and degradation of analysis in the experiment of adaptive observation (subsection 5.4c; Fig. 5.9b and 5.9c). The large positive values in Fig. 5.13a spatially correspond to the truth-based error standard deviations in Fig. 5.12c within the adaptive observation areas, due to the fact that data assimilation can reduce the uncertainty of the observed variable by correcting its ensemble mean. This correction can be proved by averaging (5.5) over all ensemble members, which is

$$\Delta\overline{Vr} = \frac{\sigma_{Vr}^2}{\sigma_{Vr}^2 + \sigma_o^2}(O - \overline{Vr}) \tag{5.12}$$

where $\Delta\overline{Vr}$ is the ensemble mean increment (i.e. analysis mean – background mean) for *Vr*; $(O - \overline{Vr})$ is the ensemble mean innovation (i.e. observation –background mean) for *Vr*; σ_{Vr}^2 is the mean-based background error variance. Equation (5.12) shows that when the background ensemble mean of *Vr* (i.e. $\overline{Vr}$) is smaller than observation O, $\Delta\overline{Vr}$ is increased in the analysis. In this way, the ensemble mean of the observed *Vr* is driven towards observations which represent the truth with small errors ($\sigma_o = 2\ m/s$ compared to σ_{Vr} in Fig. 5.12c).

On the other hand, reducing the difference between the ensemble mean and the truth is much more difficult for the unobserved *W* field. For example, there are more and stronger negative values in Fig. 5.13b, as compared to Fig. 5.13a. The degradation of *W* can be explained by the update of ensemble mean of *W*, as expressed by

$$\Delta\overline{W} = \frac{Cov(Vr,W)}{\sigma_{Vr}^2 + \sigma_o^2}(O - \overline{Vr}) \tag{5.13}$$

where $\Delta\overline{W}$ is the ensemble mean increment (i.e. analysis mean – background mean) for *W*; $Cov(Vr,W)$ is the mean-based background error cross-covariance between *Vr* and *W*. Equation (5.13) tells that the ensemble mean of *W* can be corrected by the innovation of *Vr*, that is $(O - \overline{Vr})$, under the condition that $Cov(Vr,W)$ precisely relates the errors of *Vr* and *W*. However, since $Cov(Vr,W)$ is calculated from ensemble mean that differs from the truth, it is not able to correctly describe the relationship between errors (with respect to truth). As a result, the observations of *Vr* may drive *W* further away from the truth and increase its uncertainty, as shown by the negative values in Fig. 5.13b. Similarly, negative values can also be found in Fig.

5.13a in the areas close to but not covered by observations, due to the poorly estimated spatial error covariance.

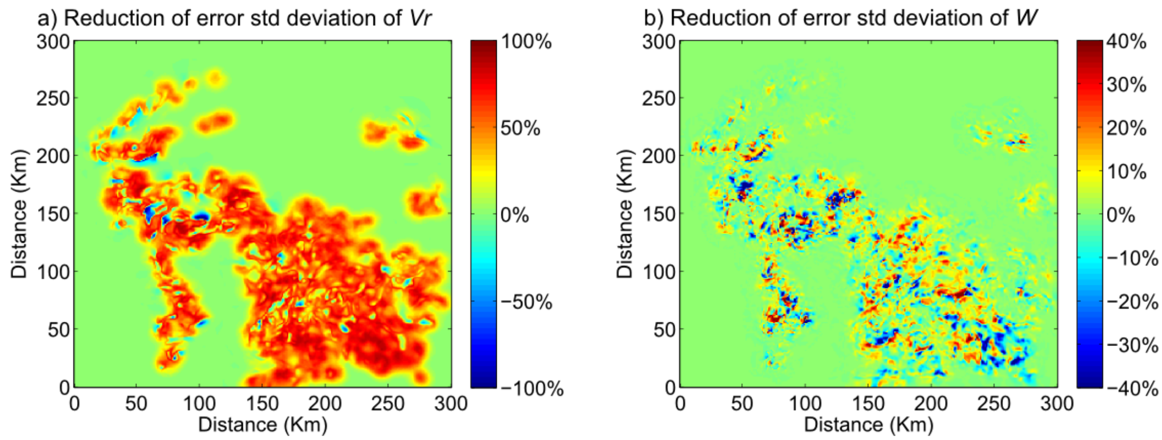

Fig. 5.13 Reduction of truth-based error standard deviation for *Vr* (a) and *W* (b) in percentage.

We stress that the negative effect on data analysis is not caused by the application of adaptive observation. Traditional uniform observation and adaptive radar observation have the same possibility of degrading the analysis results, if the truth is unknown and differs from the ensemble mean. Therefore adaptive observation could still be superior to traditional uniformly distributed observation, even though the truth is used for evaluation.

In order to assess different observation strategies properly, both the ensemble mean and the truth are used as reference for computing error variances of background and analysis. The percentage of error variance reduction is computed by [‘total background error variance’ minus ‘total analysis error variance’] divided by ‘total background error variance’ for both observed *Vr* and unobserved *W*, where ‘total variance’ means the sum of variances for a certain variable over the entire domain. The results of the four observation strategies discussed in section 5.4 are presented in Fig. 5.14. Note that the truth-based error statistics are used only for evaluation. In the data assimilation scheme and the observation strategy decision process, the mean-based error statistics are used so that the experiments can stay close to the real data assimilation system where the truth is unknown.

In the upper panel, *Vr* uncertainty is reduced by 30% to 50%, as compared to the uncertainty reduction of the unobserved *W* being less than 8% in the lower panel, which suggests that the observed variable is improved much more than the unobserved variable. When observations are redistributed from the entire domain to the areas covered by precipitation (comparing the left two observation strategies in Fig. 5.14), improvements in both *Vr* and *W* are significantly increased, particularly because more observations are assimilated, as discussed in subsection 5.4b. When the observation strategy becomes more sophisticated (comparing the right three observation strategies in Fig. 5.14), the improvement in *Vr* is slightly reduced, but the error reduction in *W* is significantly increased. This is because the adaptive observation in this study is dedicated to reduce only *W* uncertainty. The benefit brought by adaptive observation is evident whether the ensemble mean (blue bars in Fig. 5.14) or the truth (red bars in Fig. 5.14) is used for evaluation.

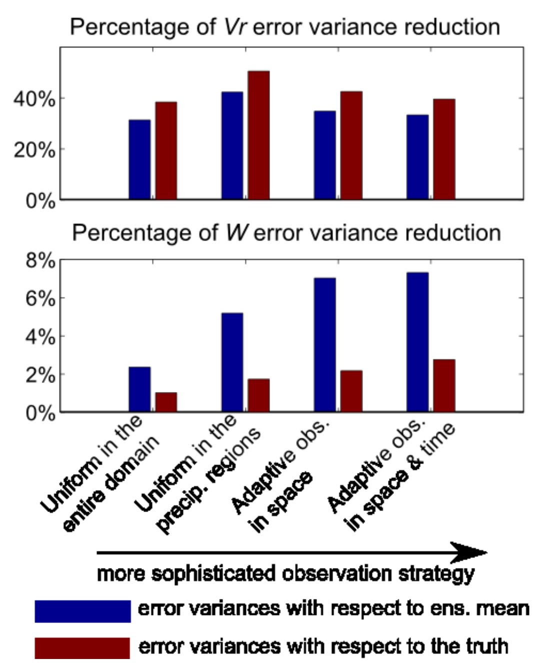

Fig. 5.14 Percentage of error reduction ([‘total background error variance’ minus ‘total analysis error variance’] divided by ‘total background error variance’) for *Vr* (upper panel) and *W* (lower panel). Four observation strategies are considered, as in section 5.4.

In the upper panel of Fig. 5.14, red bars are always higher than the neighbouring blue bars because the red bars include the correction of ensemble mean, since *Vr* is observed. In contrast, the red bars in the lower panel of Fig. 5.14 are much shorter than the corresponding blue bars. This is because while the truth-based total background error variance contains the error of ensemble mean of W, such an error is difficult to be corrected by data assimilation when the ensemble mean differs from the truth, and W is unobserved. In other words, if the ensemble mean differs from the truth, the improvement in unobserved variable is small because its ensemble mean cannot be corrected through error cross-covariances estimated with respect to the ensemble mean.

5.6 Summary and discussion

In order to improve the effectiveness of radar data assimilation in numerical forecast or in a heuristic nowcasting approach, some important unobserved variables, such as vertical velocity W, must be better assessed. For this reason, methods of adaptive radar observation are proposed in this article, for the purpose of improving the unobserved W more efficiently in the analysis step of data assimilation.

The transfer of observation information to the unobserved state variable is studied theoretically. It is demonstrated that the uncertainty of unobserved variable can be reduced significantly when the background error variance of observed variable and the background error cross-covariance between observed and unobserved variables are large. The former ensures that the observations are able to correct the observed state variable; and the latter brings the correction to the unobserved variable.

In order to decide on observation strategy and perform data assimilation, flow-dependent error statistics are needed. The Global Environmental Multiscale Limited Area Model (GEM-LAM) is used to yield 80 members of ensemble forecast. Simulated truth and radial velocity observations are generated from the first member, while the other 79 ensemble members are considered to be the background for data assimilation. The error statistics computed from the background ensemble members are used to decide observation strategy.

Four radar observation strategies are discussed and compared. The first is similar to the traditional mechanical radar observation strategy that uniformly scans the entire atmosphere.

The second strategy mimics the ‘focused scan’ possible in phased-array and some mechanical fast scanning radars, which uniformly places observations only in the precipitation region. The third strategy is an adaptive observation strategy that, according to background error statistics, determines the locations where the unobserved variable is more likely to be corrected. The fourth strategy is similar to the third one, but distributes observations in both space and time. After EnKF is applied, background and analysis error statistics are analyzed to evaluate the adaptive observation strategies. Quantitative analysis based on the total error variance shows that a greater portion of uncertainties is removed from the unobserved variable when a more sophisticated observation strategy is used.

The difference between the ensemble mean and the truth causes inaccurate uncertainty estimation. While observations are able to correct the ensemble mean for the observed variable, it is difficult to correct it for the unobserved variable, no matter which observation strategy is applied.

There are some limitations in this exploratory study. Firstly, the simulated observations are placed on model grids instead of radar coordinates. A more realistic adaptive radar observation strategy should consider how to decide radar azimuth and elevation angles. Secondly, simulated observations are used in this study, which limits the errors in background. However, in a real radar data assimilation system, much larger background errors may reduce the effect of adaptive observation. Thirdly, the improvement in unobserved variable is much smaller than the observed variable, although adaptive observation is applied (Fig. 5.14). Lastly, this article does not discuss the correction of the unobserved variable during model integration in the cycling process of data assimilation, which is possible when the observed variables are corrected in the analysis step.

Chapter 6

Conclusions

The research presented in this thesis aims at implementing and analyzing the Ensemble Kalman Filter (EnKF) system for radar data assimilation at convective-scale, and improving the EnKF for a better weather prediction by means of adaptive radar data observation. In order to achieve this goal, the flow-dependent background error statistics and other uncertainties involved in EnKF, including model error, initial ensemble spread, representations of model and observation errors, are studied. An 80-member high resolution (1-km) EnKF is then implemented to assimilate radial velocity observations provided by the McGill J. S. Marshall Radar Observatory into the Canadian Meteorological Center (CMC)'s Global Environmental Multiscale Limited Area Model (GEM-LAM). Finally, an adaptive radar observation method is proposed in order to more efficiently correct the unobserved variable at the analysis step of EnKF, and furthermore better improve the subsequent weather prediction.

Before implementing the complex data analysis system, several simple experiments of the EnKF and the linear Kalman Filter are performed to examine the influence of uncertainties in EnKF and the effectiveness of observations on data analysis. The results from the experiments of initial ensemble spread suggest that underestimating the error of the first guess is more problematic than overestimating it, because EnKF could falsely reject observations and consequently increase the analysis uncertainty. The experiments also show that the ensemble mean gradually converge to the truth when there is no model error. If model error exists, the difference between the ensemble mean analysis and the truth does not converge to zero, even though the model error is well estimated. If the model error or the observation error is poorly estimated, the analysis error is even larger, as compared to other experiments where the error statistics are well represented. However, the above conclusions are limited. Since the first guess is not far from the truth, the ensemble members are able to represent the background errors quite well with a small ensemble spread, which is different from a real data assimilation system. Moreover, there is no model bias, or error cross-covariance between different control variables, because of the use of one-dimensional viscid Burgers' equation as forecast model.

Additionally, a number of simple experiments are conducted to examine the effectiveness of observations on the analysis step of EnKF. It is shown that when the background error decorrelation distance is large, high spatial resolution of data is not required, because the background error correlation can spread observation information from the observed location to many nearly model grids. Similarly, when observation error decorrelation distance is large, EnKF does not need 'dense' observations because it will increase information redundancy. Furthermore, if the observation error covariances have to be ignored because of the limited knowledge of error structure or the restriction of the EnKF system, data 'thinning' should be performed. Additionally, under a hypothetical condition that the phased-array technique is available for radar data collection, the trade-off between observation accuracy and observation number is examined. It is indicated that a threshold of observation number exists, beyond which increasing observation quantity and enhancing observation quality can improve data analysis to the same degree. If this threshold cannot be reached, observation number is more important than observation accuracy. When the observation error statistics are misrepresented, increasing observation number or reducing observation error may have an negative effect on the EnKF.

After these simple excises, this research examines the flow-dependent background error variances and 3-dementional spatial correlations computed from 80 ensemble members produced by a 1-km grid spacing GEM-LAM. After the initial homogeneous and isotropic perturbations are added onto the first guess, the 'situation dependence' of background error structures appears after a lead-time of 15 minutes, the time evolution of which is different for different control variables. Moreover, error variances tend to grow faster inside and near the precipitation regions, compared to those in non-precipitating areas where the atmosphere is stable. The study also indicates that once microphysical processes are active, the error structures evolve rapidly, even before the occurrence of precipitations.

Based on the same numerical weather prediction model and the studies above, the 80-member high resolution (1-km) EnKF is implemented to assimilate real radial velocity observations provided by the McGill J. S. Marshall Radar Observatory. This system is derived from the operational global EnKF at Canadian Meteorological Center (CMC), with the features of four parallel EnKF subgroups, three-dimensional error correlation localization, sequential batching process and background check for observations. The parallel EnKF subgroups are used in order to prevent the insufficiency of ensemble spread. The initial ensemble members and model boundary conditions are provided by a regional EnKF system working at a larger scale. Observations with a 4-km thinning are incorporated into the 1-km grid spacing model every 5 min for 12 cycles within a 1-h cycling process, after which a 1.5-h 80-member ensemble forecast is launched. Such a system is applied on three summer cases with different precipitation structures. The indicators of ensemble spread, analysis rms and background rms exhibited sufficient ensemble spread during the cycling process in all three cases, as long as the parental regional EnKF system is applied. At the same time, the difference between background and observations gradually reduces, which indicates that the model state becomes accurate after data assimilation, at least in the observation space. In the model space, unobserved variables, such as humidity and CAPE values, can also be updated through the error cross-correlations, although such update is not enough to correct the entire precipitation field.

After the EnKF performance, the short-term forecasts are still under the influence of radial velocity assimilation for up to 90-min lead-time. For the weather system controlled by large-scale flows, the corrections made by parental regional EnKF are more important than this convective-scale EnKF. But when localized convections happen, the HREnKF accounts for most of the corrections and is able to improve the location of the storms in the analyses. Moreover, for the wide spread and stationary stratiform, the improvement lasts longer at lower elevations than higher elevations. Unfortunately, the improvement brought by the EnKF system does not survive for more than 90 min for all the three cases.

In order to allow the EnKF system to better improve the forecast, we want the unobserved vertical velocity to be more corrected at the analysis step by assimilating only radial velocity observations, which will be helpful for maintaining or triggering precipitations in NWP. Several adaptive radar observation methods are proposed, which takes advantage of hypothetical phased-array radar to adaptively collect observations. It is demonstrated that if observations can be placed where and when the background error variance of observed variable and the background error cross-covariance between observed and unobserved variables are large, the uncertainty of unobserved variable can be significantly reduced. Based on this idea, four radar observation strategies are applied on the previous EnKF system to assimilate simulated radial velocity observations. The first is similar to the traditional mechanical radar observation strategy which uniformly scans the entire atmosphere. The second strategy mimics the ‘focused scan’ used by phased-array radar, which uniformly places observations only in the precipitation region. The third strategy is an adaptive observation strategy that, according to background error statistics, determines the locations where the unobserved variable is more likely to be corrected. The fourth strategy is similar to the third one, but distributes observations in both space and time. Quantitative analysis based on the total analysis error variance of the unobserved variable shows that a greater portion of uncertainties can be removed from the unobserved variable when a more sophisticated adaptive observation strategy is used. However, when the analysis results are compared to the truth, the improvement of the unobserved variable is not significant, because of the difference between the ensemble mean and the truth. While observations are able to correct the ensemble mean for the observed variable, it is difficult to correct for the unobserved variable, no matter which observation strategy is applied.

The estimation of background error statistics from ensemble members is reliable only when the background ensemble mean is close to the reality. At the beginning of EnKF, the ensemble mean (or the first guess) and the resulting error statistics are usually inaccurate. As the cycling process proceeds, the ensemble mean of *observed* variable becomes closer to the reality. However, the ensemble mean of *unobserved* variable cannot be corrected because of the poor error correlation estimation resulted from inaccurate first guess. Since updating unobserved variables in radar data assimilation system requires reliable error correlation, it is worth examining the impact of first guess accuracy on the analysis quality.

In order to prepare an accurate first guess for radar data assimilation in a high-resolution model at convective scale, conventional observations (e.g. radiosonde) should be assimilated gradually from synoptic scale to mesoscale to ensure that all state variables are close to the reality. Such a first guess is able to produce reliable error statistics, and yield analysis results with less uncertainty for both observed and unobserved variables. An example of such a system is given in Chapter 4 where a regional EnKF was performed to assimilate conventional observations before radar data assimilation. However, the first guess provided by this system was apparently not precise enough for generating reliable error statistics.

Besides the first guess, the data assimilation quality is also strongly affected by the localization method. Chapter 3 shows that the spatial correlation of background error (Fig. 3.8) is not homogenous and isotropic; and the maximum spatial cross-correlation (Fig. 3.20) does not correspond to the center of the localization function. Therefore, the localization methods described in Chapter 4 and 5 probably damaged the spatial and cross- correlations. This problem can be solved by increasing ensemble size or applying adaptive localization method, which requires further exploration.

In addition, the assimilation of reflectivity observations can benefit the data analysis by updating more model variables such as rain mixing ratio and humidity, suppressing the false alarms, and correcting the phase errors. A better estimation of the observation and model error statistics would also be helpful.

References

Aksoy, A., D. C. Dowell, and C. Snyder, 2009: A Multicase Comparative Assessment of the Ensemble Kalman Filter for Assimilation of Radar Observations. Part I: Storm-Scale Analyses. *Mon. Wea. Rev.*, **137,** 1805-1824.

Aksoy, A., D. C. Dowell, and C. Snyder, 2010: A Multicase Comparative Assessment of the Ensemble Kalman Filter for Assimilation of Radar Observations. Part II: Short-Range Ensemble Forecasts. *Mon. Wea. Rev.*, **138,** 1273-1292.

Anderson, J. L., and S. L. Anderson, 1999: A Monte Carlo Implementation of the Nonlinear Filtering Problem to Produce Ensemble Assimilations and Forecasts. *Mon. Wea. Rev.*, **127,** 2741-2758.

Anderson, J. L., 2001: An Ensemble Adjustment Kalman Filter for Data Assimilation. *Mon. Wea. Rev.*, **129,** 2884-2903.

Anderson, J., T. Hoar, K. Raeder, H. Liu, N. Collins, R. Torn, and A. Avellano, 2009: The Data Assimilation Research Testbed: A Community Facility. *Bull. Amer. Meteor. Soc.*, **90,** 1283-1296.

Anderson, J. L., 2003: A Local Least Squares Framework for Ensemble Filtering. *Monthly Weather Review*, **131**, 634-642.

Anderson, J. L., 2007a: An Adaptive Covariance Inflation Error Correction Algorithm for Ensemble Filters. *Tellus A*, **59** (2)

Anderson, J. L., 2007b: Exploring the Need for Localization in Ensemble Data Assimilation Using a Hierarchical Ensemble Filter. *Physica D: Nonlinear Phenomena*, **230**, 99-111.

Anderson, J. L., and N. Collins, 2007: Scalable Implementations of Ensemble Filter Algorithms for Data Assimilation. *J. Atmos. Oceanic Technol.*, **24,** 1452-1463.

Anderson, J., and L. Lei, 2013: Empirical Localization of Observation Impact in Ensemble Kalman Filters. *Monthly Weather Review*, **141**, 4140-4153.

Bannister, R. N., S. Migliorini, and M. A. G. Dixon, 2011: Ensemble prediction for nowcasting with a convection-permitting model - II: forecast error statistics. *Tellus Series a-Dynamic Meteorology and Oceanography*, **63**, 497-512.

Bishop, C. H., B. J. Etherton, and S. J. Majumdar, 2001: Adaptive Sampling with the Ensemble Transform Kalman Filter. Part I: Theoretical Aspects. *Mon. Wea. Rev.*, **129,** 420-436.

Bishop, C.H. and D. Hodyss, 2011: Adaptive ensemble covariance localization in ensemble 4D-VAR state estimation, *Mon. Wea . Rev.* **139**, 1241-1255

Bonavita, M., L. Torrisi, and F. Marcucci, 2010: Ensemble data assimilation with the CNMCA regional forecasting system. *Quarterly Journal of the Royal Meteorological Society*, **136**, 132-145.

Buehner, M., P. L. Houtekamer, C. Charette, H. L. Mitchell, and B. He, 2009: Intercomparison of Variational Data Assimilation and the Ensemble Kalman Filter for Global Deterministic Nwp. Part Ii: One-Month Experiments with Real Observations. *Monthly Weather Review*, **138**, 1567-1586.

Buehner, M., P. L. Houtekamer, C. Charette, H. L. Mitchell, and B. He, 2009: Intercomparison of Variational Data Assimilation and the Ensemble Kalman Filter for Global Deterministic Nwp. Part I: Description and Single-Observation Experiments. *Monthly Weather Review*, **138**, 1550-1566.

Buizza, R. and A. Montani 1999: Targeting Observations Using Singular Vectors. *Journal of the Atmospheric Sciences* **56**(17): 2965-2985.

Caron, J. F. and L. Fillion, 2010: An Examination of the Incremental Balance in a Global Ensemble-Based 3D-Var Data Assimilation System. *Mon. Wea. Rev.*, **138**, 3946-3966.

Caron, J. F., 2012: Mismatching Perturbations at the Lateral Boundaries in Limited-Area Ensemble Forecasting: A Case Study. *Mon. Wea. Rev.*, **141,** 356-374.

Caya, A., J. Sun, and C. Snyder, 2005: A Comparison between the 4dvar and the Ensemble Kalman Filter Techniques for Radar Data Assimilation. *Monthly Weather Review*, **133**, 3081-3094.

Chen, Y. and C. Snyder, 2006: Assimilation of hurricane position with an ensemble Kalman Filter. *Geophysical Research Abstracts*, **8**, 09910

Côté, J., S. Gravel, A. Méthot, A. Patoine, M. Roch, and A. Staniforth, 1998: The operational CMC-MRB Global Environmental Multiscale (GEM) model. Part I: Design considerations and formulation. *Mon. Wea. Rev.*, **126**, 1373-1395.

Cho, Y.-H., G. W. Lee, K.-E. Kim, and I. Zawadzki, 2006: Identification and Removal of Ground Echoes and Anomalous Propagation Using the Characteristics of Radar Echoes. *J. Atmos. Oceanic Technol.*, **23**, 1206-1222.

Chung, K.-S., I. Zawadzki, M. K. Yau, and L. Fillion, 2009: Short-Term Forecasting of a Midlatitude Convective Storm by the Assimilation of Single-Doppler Radar Observations. *Mon. Wea. Rev.*, **137,** 4115-4135.

Chung, K.-S., W. Chang, L. Fillion, and M. Tanguay, 2013: Examination of Situation-Dependent Background Error Covariances at the Convective Scale in the Context of the Ensemble Kalman Filter. *Mon. Wea. Rev.*, **141**, 3369-3387.

Côté, J., S. Gravel, A. Méthot, A. Patoine, M. Roch, and A. Staniforth, 1998: The Operational CMC-MRB Global Environmental Multiscale (GEM) Model. Part I: Design Considerations and Formulation. *Mon. Wea. Rev.*, **126,** 1373-1395.

Daley R. 1985. The analysis of synoptic scale divergence by a statistical interpolation procedure. *Mon. Wea. Rev.*, **113**, 1066–1079.

Dayley, R. 1991: *Atmospheric Data Analysis*. Cambridge University Press.

Davis, C., W. Wang, J. Dudhia, and R. Torn, 2010: Does Increased Horizontal Resolution Improve Hurricane Wind Forecasts? *Weather and Forecasting*, **25**, 1826-1841.

Doviak, R. J., and D. S. Zrnic, 1984: *Doppler Radar and Weather Observations.* Academic Press, 458 pp.

Dowell, D. C., F. Zhang, L. J. Wicker, C. Snyder, and N. A. Crook, 2004: Wind and Temperature Retrievals in the 17 May 1981 Arcadia, Oklahoma, Supercell: Ensemble Kalman Filter Experiments. *Mon. Wea. Rev.*, **132,** 1982-2005.

Dowell, D. C., and L. J. Wicker, 2009: Additive Noise for Storm-Scale Ensemble Data Assimilation. *J. Atmos. Oceanic Technol.*, **26**, 911-927.

Dowell, D., G. Romine, and C. Snyder, 2010 : Ensemble storm-scale data assimilation and prediction for severe convective storms. *25th Severe Local Storms Conference* Denver, Colorado, Amer. Meteor. Soc., paper 9.5.

Dowell, D. C., L. J. Wicker, and C. Snyder, 2011: Ensemble Kalman Filter Assimilation of Radar Observations of the 8 May 2003 Oklahoma City Supercell: Influences of Reflectivity Observations on Storm-Scale Analyses. *Mon. Wea. Rev.*, **139,** 272-294.

Evensen, G., 1994: Sequential Data Assimilation with a Nonlinear Quasi-Geostrophic Model Using Monte Carlo Methods to Forecast Error Statistics. *J. Geophys. Res.*, **99,** 10143-10162.

Evensen, G., 2003: The Ensemble Kalman Filter: Theoretical Formulation and Practical Implementation. *Ocean Dynam.*, **53,** 343-367.

Evensen, G 2006: *Data Assimilation: The Ensemble Kalman Filter.* Springer.

Fabry, F., and A. Kilambi, 2011: The Devil Is in the Details: Preparing Radar Information for Its Proper Assimilation. 19A.6, *35th Conference on Radar Meteorology*, Pittsburgh, PA. (Available at https://ams.confex.com/ams/35Radar/webprogram/Paper191698.html)

Fillion, L., and S. Bélair, 2004: Tangent Linear Aspects of the Kain-Fritsch Moist Convective Parameterization Scheme. *Mon. Wea. Rev.*, **132,** 2477-2494.

Fillion, L., and Coauthors, 2010: The Canadian Regional Data Assimilation and Forecasting system. *Weather Forecasting*, **25**, 1645–1669.

Gaspari, G., and S. E. Cohn, 1999: Construction of Correlation Functions in Two and Three Dimensions. *Q. J. R. Meteorol. Soc.*, **125**, 723-757.

Greybush, S. J., E. Kalnay, T. Miyoshi, K. Ide, and B. R. Hunt, 2010: Balance and Ensemble Kalman Filter Localization Techniques. *Monthly Weather Review*, **139**, 511-522.

Gustafsson, N., S. Hörnquist, M. Lindskog, L. Berre, B. Navascués, S. Thorsteinsson, X. Huang, K. Mogensen, J. Rantakokko, 1999: Three-dimensional variational data assimilation for a high resolution limited area model (HIRLAM). *HIRLAM Technical Report*, No. 40. January 1999.

Heinselman, P. L., and S. M. Torres, 2011: High-Temporal-Resolution Capabilities of the National Weather Radar Testbed Phased-Array Radar. *J. Appl. Meteor. Climatol.*, **50**, 579–593.

Houtekamer, P. L., and H. L. Mitchell, 1998: Data Assimilation Using an Ensemble Kalman Filter Technique. *Mon. Wea. Rev.*, **126,** 796-811.

Houtekamer, P. L., and H. L. Mitchell, 2001: A Sequential Ensemble Kalman Filter for Atmospheric Data Assimilation. *Mon. Wea. Rev.*, **129,** 123-137.

Houtekamer, P. L., H. L. Mitchell, G. Pellerin, M. Buehner, M. Charron, L. Spacek, and B. Hansen, 2005: Atmospheric Data Assimilation with an Ensemble Kalman Filter: Results with Real Observations. *Mon. Wea. Rev.*, **133,** 604-620.

Kain, J. S., and J. M. Fritsch, 1990: A One-Dimensional Entraining/Detraining Plume Model and Its Application in Convective Parameterization. *J. Atmos. Sci.*, **47,** 2784-2802.

Kalnay, E. 2003: *Atmospheric Modeling, Data Assimilation and Predictability*. Cambridge University Press.

Keeler, R. J., and S. M. Ellis, 2000: Observational Error Covariance Matrices for Radar Data Assimilation. *Phys. Chem. Earth Pt B-Hydrol. Oceans Atmos.*, **25,** 1277-1280.

Kendall, Sir, M., A. Stuart and J.K. Ord, 1986 : *Kendall's advanced theory of statistics – 5 th ed, Vol 1: distribution theory*. Charles Griffin and Company Limited, London, 604 pp.

Lu, H., and Q. Xu, 2009: Trade-Offs between Measurement Accuracy and Resolutions in Configuring Phased-Array Radar Velocity Scans for Ensemble-Based Storm-Scale Data Assimilation. *Journal of Applied Meteorology and Climatology*, **48**, 1230-1244.

Mailhot, J., S. Bélair, R. Benoit, B. Bilodeau, Y. Delage, L. Fillon, L. Garand, C. Girard, and A. Tremblay, 1998: Scientific Description of Rpn Physics Library - Version 3.6. Recherche en prévision numérique, 188 pp. (Available from RPN, 2121 Trans-Canada Highway, Dorval, PQ H9P 1J3, Canada; also online at http://www.cmc.ec.gc.ca/rpn/physics/physic98.pdf.)

Majumdar, S. J., C. H. Bishop, et al. 2002: Adaptive Sampling with the Ensemble Transform Kalman Filter. Part II: Field Program Implementation. *Monthly Weather Review* **130**(5): 1356-1369.

Milbrandt, J. A., and M. K. Yau, 2005: A Multimoment Bulk Microphysics Parameterization. Part I: Analysis of the Role of the Spectral Shape Parameter. *J. Atmos. Sci.*, **62,** 3051-3064.

Mitchell, H. L., P. L. Houtekamer, and G. Pellerin, 2002: Ensemble Size, Balance, and Model-Error Representation in an Ensemble Kalman Filter. *Mon. Wea. Rev.*, **130,** 2791-2808.

Mitchell, H. L., and P. L. Houtekamer, 2009: Ensemble Kalman Filter Configurations and Their Performance with the Logistic Map. *Mon. Wea. Rev.*, **137,** 4325-4343.

Montmerle, T. and L. Berre, 2010: Diagnosis and formulation of heterogeneous background-error covariances at the mesoscale. *Quarterly Journal of the Royal Meteorological Society*, **136**, 1408-1420.

Noilhan, J., and S. Planton, 1989: A Simple Parameterization of Land Surface Processes for Meteorological Models. *Mon. Wea. Rev.*, **117,** 536-549.

Nutter, P., D. Stensrud, and M. Xue, 2004a: Effects of Coarsely Resolved and Temporally Interpolated Lateral Boundary Conditions on the Dispersion of Limited-Area Ensemble Forecasts. *Mon. Wea. Rev.*, **132,** 2358-2377.

Nutter, P., M. Xue, and D. Stensrud, 2004b: Application of Lateral Boundary Condition Perturbations to Help Restore Dispersion in Limited-Area Ensemble Forecasts. *Mon. Wea. Rev.*, **132,** 2378-2390.

Palmer, T. N., R. Gelaro, et al. 1998: Singular Vectors, Metrics, and Adaptive Observations. *Journal of the Atmospheric Sciences* **55**(4): 633-653.

Raeder, K., J. L. Anderson, N. Collins, T. J. Hoar, J. E. Kay, P. H. Lauritzen, and R. Pincus, 2012: Dart/Cam: An Ensemble Data Assimilation System for Cesm Atmospheric Models. *Journal of Climate*, **25**, 6304-6317.

Saito, K., H. Seko, M. Kunii, and T. Miyoshi, 2012: Effect of Lateral Boundary Perturbations on the Breeding Method and the Local Ensemble Transform Kalman Filter for Mesoscale Ensemble Prediction. *Tellus A*, **64,** 11594.

Skamarock, W. C., 2004: Evaluating Mesoscale NWP Models Using Kinetic Energy Spectra. *Mon. Wea. Rev.*, **132**, 3019-3032.

Snyder, C., and F. Zhang, 2003: Assimilation of Simulated Doppler Radar Observations with an Ensemble Kalman Filter. *Mon. Wea. Rev.*, **131,** 1663-1677.

Snyder, C., T. Bengtsson, P. Bickel, and J. Anderson, 2008: Obstacles to High-Dimensional Particle Filtering. *Monthly Weather Review*, **136**, 4629-4640.

Sun, J., and N. A. Crook, 1997: Dynamical and Microphysical Retrieval from Doppler Radar Observations Using a Cloud Model and Its Adjoint. Part I: Model Development and Simulated Data Experiments. *J. Atmos. Sci.*, **54,** 1642-1661.

Surcel, M., I. Zawadzki, and M. K. Yau, 2014: On the Filtering Properties of Ensemble Averaging for Storm-Scale Precipitation Forecasts. *Monthly Weather Review*, **142**, 1093-1105.

Stensrud, D. J. and J. D. Gao, 2010: Importance of Horizontally Inhomogeneous Environmental Initial Conditions to Ensemble Storm-Scale Radar Data Assimilation and Very Short-Range Forecasts. *Monthly Weather Review*, **138**, 1250-1272.

Sundqvist, H., 1978: Parameterization Scheme for Non-Convective Condensation Including Prediction of Cloud Water-Content. *Quarterly Journal of the Royal Meteorological Society*, **104**, 677-690.

Szunyogh, I., E. J. Kostelich, G. Gyarmati, E. Kalnay, B. R. Hunt, E. Ott, E. Satterfield, and J. A.

Yorke, 2008: A local ensemble transform Kalman filter data assimilation system for the NCEP global model. *Tellus Series a-Dynamic Meteorology and Oceanography*, **60**, 113-130.

Tippett, M. K., J. L. Anderson, C. H. Bishop, T. M. Hamill, and J. S. Whitaker, 2003: Ensemble Square Root Filters. *Mon. Wea. Rev.*, **131,** 1485-1490.

Tong, M., and M. Xue, 2005: Ensemble Kalman Filter Assimilation of Doppler Radar Data with a Compressible Nonhydrostatic Model: OSS Experiments. *Mon. Wea. Rev.*, **133,** 1789-1807.

Tong, M., and M. Xue, 2008a: Simultaneous Estimation of Microphysical Parameters and Atmospheric State with Simulated Radar Data and Ensemble Square Root Kalman Filter. Part I: Sensitivity Analysis and Parameter Identifiability. *Mon. Wea. Rev.*, **136**, 1630-1648.

Tong, M., and M. Xue, 2008b: Simultaneous Estimation of Microphysical Parameters and Atmospheric State with Simulated Radar Data and Ensemble Square Root Kalman Filter. Part II: Parameter Estimation Experiments. *Mon. Wea. Rev.*, **136**, 1649-1668.

Torn, R. D., 2010: Ensemble-Based Sensitivity Analysis Applied to African Easterly Waves. *Weather and Forecasting*, **25**, 61-78.

Wang, H., J. Sun, X. Zhang, X.-Y. Huang, and T. Auligné, 2013: Radar Data Assimilation with WRF 4d-Var. Part I: System Development and Preliminary Testing. *Mon. Wea. Rev.*, **141,** 2224-2244.

Whitaker, J. S., and T. M. Hamill, 2002: Ensemble Data Assimilation without Perturbed Observations. *Mon. Wea. Rev.*, **130,** 1913-1924.

Xu, Q., K. Nai, and L. Wei, 2007: An Innovation Method for Estimating Radar Radial-Velocity Observation Error and Background Wind Error Covariances. *Q. J. R. Meteorol. Soc.*, **133**, 407-415.

Xue, M., M. Tong, and K. K. Droegemeier, 2006: An Osse Framework Based on the Ensemble Square Root Kalman Filter for Evaluating the Impact of Data from Radar Networks on Thunderstorm Analysis and Forecasting. *Journal of Atmospheric and Oceanic Technology*, **23**, 46-66.

Yussouf, N., and D. J. Stensrud, 2010: Impact of Phased-Array Radar Observations over a Short Assimilation Period: Observing System Simulation Experiments Using an Ensemble Kalman Filter. *Monthly Weather Review*, **138**, 517-538.

Zhang, F., C. Snyder, and J. Sun, 2004: Impacts of initial estimate and observation availability on convective-scale data assimilation with an ensemble Kalman filter. *Monthly Weather Review*, **132**, 1238-1253.